Spectroscopic Analysis of Primeval Galaxy Candidates

Joseph Caruana

Christ Church

University of Oxford

A thesis submitted for the degree of

Doctor of Philosophy

Michaelmas 2012

To my family, especially my parents and my sister Maria, who have been a constant presence throughout all my life, and without whom I would not be where I am today.

Acknowledgements

As I look back over the past few years, I realize how many people have left their mark on my life. As I embark on this mission to thank each and every one of them for their kindness, I realize how tough it is going to be to ensure that I do not leave anybody out. I hereby offer my deeply felt note of thanks to all of these special people, who are listed below in no particular order.

My office mates in room 512, who were ever so lovely and who managed the formidable task of maintaining their sanity despite my presence in the same office, day in, day out. Adam, Silvio, Taysun, Tessa, and Phil, you were indeed great company over the last three years.

My supervisor, Andy, who was ever so patient in advising me throughout the whole process, and whose guidance and friendship I will cherish for many years to come. Thanks for being such a great boss! Stephen, who was always ready to help when questions arose, and to offer his honest opinion whenever it was asked for. Also, Vanessa and Ashling, who, with their exceptional organization and patience, ensured that deadlines were never forgotten.

Thanks to the Christ Church community, where I was made to feel so welcome. Anca, Camille, Phil, Torben, Simone, Melanie, Karolina, Max, Davide, Kiterie, Arne: your friendship will never be forgotten. With you folks around I could be sure there was always someone I could count on over the past three years. Cheers also to the physics community in Christ Church, especially my college tutors, Derek & Guy - and Axel.

Here's to Richard, who is ever so keen to follow my progress, and whose wide-ranging chats are always an inspiration.

A big cheer for all the people from The Astronomical Society of Malta, past and present, where I found my first astronomy community. Many thanks also to Kris and Charles for supporting me on the way that led here.

Here also are my thoughts for the ones whom I was extremely lucky to meet before their untimely departure - Joe and Steve, thanks for your kind words and wisdom - you will always be missed.

And finally, my most special thanks to the ones who share my every joy and sorrow - my family back at home, especially my parents and sister, to whom this work is dedicated.

Abstract

This thesis presents spectroscopic observations of $z \geq 7$ galaxy candidates in the Hubble Ultra Deep Field, which were selected with HST WFC3 imaging, using the Lyman-Break technique. Four z-band ($z \approx 7$) dropout galaxies were targeted with Gemini/GNIRS, one z-band dropout galaxy and three Y-band ($z \approx 8-9$) dropout galaxies with VLT/XSHOOTER, and 22 z-band dropouts with VLT/FORS2, where 15 of the latter are strong candidates. No evidence of Lyman-α emission is found, and the upper limits on the Lyman-α flux and the broad-band magnitudes are used to constrain the rest-frame equivalent widths for this line emission. Amongst the targeted objects, observations were made of HUDF.YD3, a relatively bright Y-band dropout galaxy likely to be at $z \approx 8-9$ on the basis of its colours in the HST ACS and WFC3 images. Lehnert et al. (2010) observed this galaxy using the VLT/SINFONI integral field spectrograph and claim that it exhibits Lyman-α emission at $z = 8.55$. In observations of this object described in this thesis, which were made with VLT/XSHOOTER and Subaru/MOIRCS, this line was not reproduced despite the expected signal in the combined MOIRCS & XSHOOTER data being 5σ. Hence it appears unlikely that the reported Lyman-α line emission at $z > 8$ is real.

Accounting for incomplete spectral coverage, in total (across all spectrographs) 9.63 z-band dropouts and 1.15 Y-band dropouts are surveyed to a Lyman-α rest-frame Equivalent Width better than 75Å. A model where the fraction of high rest-frame equivalent width emitters follows the trend seen at $z = 3-6.5$ is inconsistent with these non-detections at $z = 7-9$ at a confidence level of $\sim 91\%$, which may indicate that a significant neutral HI fraction (χ_{HI}) in the intergalactic medium suppresses the Lyman-α line at $z > 7$. In particular, the lack of detection of Lyman-α emission in this spectroscopy is compared with results at lower redshift by Stark et al. (2010), who derive a mapping between Lyman-α fractions and χ_{HI}

based on radiative transfer simulations by McQuinn et al. (2007). These results suggest a lower limit of $\chi_{HI} \sim 0.5$.

All data reduction and analysis presented in this thesis was led by the author. Observations made with Gemini/GNIRS, described in Chapter 3, were designed by Andrew Bunker and made available for this thesis. Simulations described in Wilkins et al. (2011) and Lorenzoni et al. (2011), cited in Chapters 3 and 4, were carried out by Stephen Wilkins.

Some of the content of this thesis has already appeared in the following publications:

- J. Caruana, A.J. Bunker, S.M. Wilkins, E.R. Stanway & S. Lorenzoni, Spectroscopy of $z > 7$ sources using GEMINI/GNIRS and VLT/XSHOOTER, MNRAS, 427, 3055, December 2012.
- A.J. Bunker, J. Caruana, S.M. Wilkins, E. R. Stanway S. Lorenzoni, M. Lacy, M. J. Jarvis, & S. Hickey, VLT/XSHOOTER and Subaru/MOIRCS spectroscopy of HUDF.YD3: no evidence for Lyman-α emission at $z = 8.55$, MNRAS, 430, 3314, April 2013.

Contents

List of Figures

Chapter 1

Introduction

1.1 In the Beginning

One of the foremost questions of modern-day cosmology and astrophysics deals with how the observed structure in the cosmos, in all its complexity, arose from simpler beginnings. The question of how the world came to be occupied the minds of human beings for thousands of years. Over the past century, astronomers have made great strides towards gaining a better understanding of both the Universe's origins and its subsequent evolution. The basis on which the whole edifice of our understanding stands is referred to as the Hot Big Bang model of the Universe. The Hot Big Bang model holds that the Universe began 13.7 billion years ago, arising from a singularity of infinitely high density and temperature. Observations in the early 20th century by Vesto Slipher (Slipher, 1915, 1917) revealed that observed "nebulae" (which turned out to be galaxies) exhibited redshifts in their spectral lines, and in 1929 Edwin Hubble established the empirical Redshift-distance law of galaxies (Hubble, 1929), nowadays infamously known as Hubble's Law. Hubble's Law states that the further away from us a galaxy is, the larger its redshift. If one interprets the redshift as a direct measurement of the recession speed of the galaxy, then the observation supports

a particular set of solutions to Einstein's equations of general relativity, namely a homogeneous and isotropic, expanding universe, as illustrated in the work of Georges Lemaître as early as 1927 (Lemaître, 1927). The observation of receding galaxies is the first major piece of evidence for the Big Bang theory.

The Hot Big Bang model goes on to stipulate that the beginning of the universe was followed by a period of accelerated expansion, known as Inflation. The duration of this inflatory period was very small of the order of 10^{-38} seconds, but this time was sufficient to increase the size of the universe by about 10^{26} orders of magnitude[1]. At the end of inflation, the universe was very homogenous on the largest of scales, however quantum fluctuations led to local perturbations. Until about a redshift of 3400, the universe was radiation-dominated (Spergel et al., 2003), and radiation continued to be thermally coupled with matter by means of Compton scattering[2] until a redshift of about 1100, at which point the universe ceased to be optically thick to radiation. As the universe continued to expand, its temperature T, cooled down according to $T \propto (1 + z)$ where z is the redshift.

Once the temperature dropped down to 10^9K, the strong force took over and light nuclei were able to form, with ^{4}He nuclei synthesising later. By this point, the universe had cooled down sufficiently such that heavier elements could not be formed via nuclear fusion. The prediction of the relative abundances of nuclei and particles during this process of Big Bang nucleosynthesis, which lasted for about 10^3s, agree perfectly with observations (75% H, 24.8% ^{4}He). This provides the second major piece of evidence for the Hot Big Bang model, and is testament to the power of the theory.

As the universe continued to expand, the temperature kept dropping, and at a

[1]This is often referred to as an expansion of 60 e-folds, where $e^{60} \sim 10^{26}$.

[2]Compton scattering describes the process whereby upon interacting with matter, a photon is elastically scattered, resulting in the photon losing some of its energy which is transferred to a scattering electron. The electron, in turn, recoils and gets ejected from the atom, leaving the atom ionised.

redshift of about $z \sim 3200$, the universe had cooled to about 10^4K; at this point it evolved from being radiation-dominated to being matter-dominated. However, it was still too hot for atoms to form, and the universe consisted of an ionized plasma of matter and radiation, which interacted with each other via Compton scattering.

When one calculates the probability of interactions between electrons and photons as it varies with the changing ionization of the gas, it emerges that at around $z = 1000$ this scattering came to an end, and protons and electrons combined to form atoms of hydrogen, with radiation decoupling from matter at the same time. This marks a major transition in the history of the universe, and it left its signature in the form of a spherical, ever expanding surface of redshifted light from when the Universe was still not transparent, and observed today as the Cosmic Microwave Background (CMB) which was serendipitously discovered in 1965 by Arno Penzias and Robert Wilson (Penzias and Wilson, 1965) and which was remarkably predicted by George Gamow back in the late 1940s. This radiation was shown to be isotropic and to have a temperature of 2.7 Kelvin, precisely in the expected range of the Hot Big Bang model (Dicke, Peebles, Roll, and Wilkinson, 1965). Observations made in the early 1990s with the Far Infrared Absolute Spectrophotometer (FIRAS) on board the Cosmic Background Explorer (COBE) found that the CMB deviates from a perfect black-body spectrum by only 50 parts per million (Fixsen et al., 1994), thus making it the most perfect black body spectrum known to exist. The observation of the CMB spectrum is the third key piece of evidence for the Big Bang model. As tiny as these deviations are, they are the remnants of quantum fluctuations in the early universe, tiny perturbations (of the order of 10^{-5}) of the energy and gravitational potential that are crucial to our own existence; had the universe been perfectly homogeneous, no structure would have formed and we would not be here to tell the story. Our current paradigm has indeed reached a point where the actual number of independent observational constraints is larger than the number of parameters that need to be

constrained. This has led to the subject being referred to as precision cosmology.

1.2 The Dark Ages and The First Objects

Following the formation of the first atoms of hydrogen and helium (recombination), the CMB glow slowly faded out, and in the lack of any light-emitting sources, the universe entered a period known as the "dark ages". During this era, which lasted hundreds of millions of years, the perturbations in density continued growing due to gravitational instability. This evolution is commonly explained by means of a simple model, such as in Mo et al. (2010) and Loeb (2010), which is described below. Let us consider a gravitating mass $M_g = \rho_{\rm g} V$, where $\rho_{\rm g}$ is the density and V is the volume of this mass within a sphere of radius $a(t)$, where t denotes time, such that $V = 4/3\pi a^3$. The resulting acceleration is:

$$\frac{d^2a}{dt^2} = -\frac{GM_{\rm g}}{a^2} \tag{1.1}$$

Without going into unnecessary detail, one can simply note here that from the theory of general relativity, the variable $\rho_{\rm g} = (\rho + 3p/c^2)$ takes the place occupied in Newtonian physics by the gravitating mass density ρ, where p is the pressure, which in general relativity has a gravitational effect as it is found in the stress-energy tensor (hence its inclusion in the expression for $\rho_{\rm g}$). We can find the variation of the pressure, p with the scale factor of the universe $a(t)$ by noting that thermodynamically, the change in internal energy $d(\rho c^2 V)$ is equal to the work done by the pressure, pdV, such that $d(\rho c^2 V) = -pdV$. From this we obtain the expression $\dot{\rho} + 3\dot{a}(\rho + p/c^2)/a = 0$ where $\dot{\rho}$ and $\dot{a}$ are $d\rho/dt$ and da/dt respectively. Now, multiplying equation 1.1 by $\dot{a}$ and using this expression, we arrive at:

$$\frac{\dot{a}^2}{2} - \frac{GM}{a} = E \tag{1.2}$$

where $M = \rho V$ and E denotes the total energy. If $E \geq 0$, the sphere that we are considering would be gravitationally unbound and hence would continue to grow ever larger. But if $E < 0$, then the sphere would indeed be bound by gravity and at some point collapse. Defining the Hubble parameter, $H = \dot{a}/a$, we can present equation 1.2 as:

$$1 - \frac{E}{\dot{a}^2/2} = \Omega \tag{1.3}$$

where $\Omega = \rho/\rho_c$.

Hence, from this discussion we observe that regions which are overdense can be considered as if they were part of a closed ($\Omega > 1$) universe, leading to the formation of structures held by gravity. As we have seen, the two competing contestants involved in this scenario of ever increasing density difference are gravity and pressure. As the gas density at the core of a cloud becomes higher, a pressure wave is emitted outwards at the speed of sound. The gas pressure exerts an outward force, whilst gravity acts in the opposite direction, trying to collapse the cloud. If the wave does not reach the edge of the cloud during the time it would take the cloud to collapse in the absence of any outward forces (i.e. the free-fall time of the cloud), then the cloud will indeed end up collapsing. In such a case, the speed of the outward-propagating wave would be too low with respect to the speed of the infalling gas, and therefore, the pressure wave would be transported inwards. If, however, the speed of the wave is larger than the speed of the infalling gas, i.e. if the gas cloud is small enough such that the free-fall time, which itself depends on the cloud's mass, is fairly small, then collapse is resisted.

For the total energy, we must have $2E_K + E_G = 0$ for virial equilibrium, where E_K denotes the thermal kinetic energy resulting in outward pressure and $E_G = -\frac{3}{5}\frac{GM^2}{R}$ is the gravitational binding energy of the cloud, i.e. the amount of energy required to pull all the material apart to infinity. If the cloud is to collapse, then $E_K < -\frac{1}{2}E_G$,

whereas if it is to continue expanding, $E_K > -\frac{1}{2}E_G$. If, for the purpose of this simple analysis, we assume an ideal gas, then $E_K = \frac{3}{2}Nk_BT$, and the requirement for collapse becomes $\frac{3}{2}Nk_BT < -\frac{1}{2}E_G$. This leads to what is known as Jeans' criterion:

$$3Nk_BT < \frac{3}{5}\frac{GM}{R} \tag{1.4}$$

This criterion yields the smallest possible mass which the cloud must have in order for it to collapse:

$$M_J = \left(\frac{5Nk_BTR}{G}\right)^{1/2} \tag{1.5}$$

If we denote the mean molecular weight of the gas by μ and the mass of a proton by m_p, then the number of particles constituting the Jeans mass is:

$$N = M_J/m_p\mu \tag{1.6}$$

Considering the mass density, ρ, of the cloud, we have:

$$M_J = \frac{4\pi\rho R^3}{3} \tag{1.7}$$

Merging equations 1.4, 1.6 and 1.7, we derive:

$$M_J = \left(\frac{3}{4\pi\rho}\right)^{1/2}\left(\frac{5k_BT}{G\mu m_p}\right)^{3/2} \tag{1.8}$$

which can be rewritten in the following form:

$$M_J \approx 45T_k^{3/2}(n_{cm^{-3}})^{-1/2}M_\odot \tag{1.9}$$

If the temperature, T_k, is not very different from that at recombination ($\sim$ 3000K) and taking $n \sim 6 \times 10^3$, we find that the lower mass limit for the initial gas cloud

to collapse (roughly about 100 Myr following the Big Bang) is $\sim 10^5 M_\odot$, a value that was shown by Haiman et al. (1996) not to depend on redshift. The first galaxies photoionized and heated the gas in the universe to above 10^4K, so the lower mass limit for galaxies became larger than about $10^8 M_\odot$ (Haiman and Loeb, 1999). Eventually, during the era of reionization, small halos which had a virial temperature $< 10^4 K$ had their gas expelled by the UV radiation which by now was permeating the cosmos, where the virial temperature is given by:

$$T_{vir} = \frac{\mu V_c^2}{2k_B} = 36100 \frac{\mu}{0.6 m_p} \left(\frac{r_{vir}}{h^{-1} kpc} \right)^2 K \frac{\Omega_0}{\Omega(z)} \frac{\Delta_c}{200} \left(\frac{1+z}{10} \right)^3 \tag{1.10}$$

where μ is the mean molecular weight determined by ionization equilibrium, V_c is the circular velocity of the halo, k_B is Boltzmann's constant, m_p is the proton mass, and Δ_c is the collapse overdensity (Barkana and Loeb, 1999).

In cosmology we have come to an accepted model of structure formation which proposes a hierarchical (bottom-up) process for the formation of objects. Following the predictions of such a model, we expect that the very first objects must have formed inside clumps of gas with mass slightly higher than the $\sim 10^5 M_\odot$ threshold. During the collapse of a dark matter halo, the gas falls in at a speed $V = (GM/r_{vir})^{1/2}$ (where r_{vir} is the virial radius). As described in Barkana & Loeb (2001), Mo et al. (2010), Loeb (2010), collisions of several gas streams result in the gas being shocked to the virial temperature, at which temperature the thermal pressure of the gas resists gravitational collapse; in order for the first stars to form, the gas must fragment - and the only way this can be achieved is by cooling it, increasing its density such that the order of the Jeans mass comes down to that of the stars.

In present day galaxies, gas cooling happens by means of heavy elements. However, in the early universe these elements had not yet been synthesized, so the only cooling mechanism available at the time was radiative cooling via transitions in atomic and molecular hydrogen (Barkana and Loeb, 2001, 1999). If collisions between atoms

were energetic enough, then they would become excited as a result, and radiation would be released when they de-excited later. However, at temperatures less than 10^4K, these collisions are simply not energetic enough, so these first clouds of gas had to be cooled by some other means, as their virial temperature was indeed $< 10^4$K. Saslaw and Zipoy (1967) were the first to note that the required cooling could instead come about by means of molecular Hydrogen, H_2, which would have formed via a two-step reaction (McDowell, 1961):

$$\mathrm{H} + e^- \rightarrow \mathrm{H}^- + \mathrm{photon} \tag{1.11}$$

$$\mathrm{H}^- + \mathrm{H} \rightarrow \mathrm{H}_2 + e^- \tag{1.12}$$

or, not so efficiently:

$$\mathrm{H} + \mathrm{H}^+ \rightarrow \mathrm{H}_2^+ + \mathrm{photon} \tag{1.13}$$

$$\mathrm{H}_2^+ + \mathrm{H} \rightarrow \mathrm{H}_2 + \mathrm{H}^+ \tag{1.14}$$

with the free electrons, e^-, serving the role of reaction catalysts. In the first gas clouds, there were enough free electrons around to catalyse this H_2 forming reaction, and so the gas cooled down (Barkana & Loeb, 2001). It should be noted that Anninos and Norman (1996) showed that the primordial fraction of H_2 is about 2×10^{-6} (Hirata and Padmanabhan, 2006 find $\sim 6\times10^{-7}$), which is not sufficient to cool the gas enough for star formation to be able to take place. Tegmark et al. (1997) studied how the H_2 abundance for various halo masses (trying different initial conditions) evolved, and concluded that for every virialization redshift, z_{vir}, there exists a critical mass $M_{\mathrm{c}}(z)$, such that only halos whose mass is larger than this critical value will collapse (see their Fig. 6) and result in the formation of luminous objects, i.e. the critical fraction of H_2 required for collapse was only attained by the more massive halos.

Things changed once the very first stars formed. The UV radiation emitted by

these objects resulted in a UV background that dissociated H_2 molecules, suppressing their role in cooling the gas (Haiman, Rees, and Loeb, 1997; Ciardi, Ferrara, Governato, and Jenkins, 2000; Haiman, Abel, and Rees, 2000a). This ensured that star formation inside halos with low virial temperatures was suppressed, leading to subsequent halos having a higher virial temperature above 10^4K, which is a high enough temperature to allow cooling via atomic transitions; gas cooling could now be achieved by atomic hydrogen (Barkana and Loeb, 2001), with no more need for molecular hydrogen - and later still, the cooling process became more efficient via heavy elements.

Let us now take a step back to see the large picture of the unfolding events. Slowly, on the very largest scales, regions collapsed along the first axis to form two-dimensional sheets which, upon collapsing along the second axis, resulted in one-dimensional filaments (e.g. Bhavsar et al., 2003; Colberg et al., 2005); a foam-like, filamentary structure commonly referred to as the cosmic web emerged (Bond et al., 1996). These filaments would then collapse along the third axis, resulting into virialized halos (e.g. Shen et al., 2006). The nodes of intersection of these tendrils of structure were the regions where the first stars formed in the most cool and dense gas knots. Subsequently, galaxies formed. This pattern of structure is reflected today in the way galaxies are hierarchically organised in clusters, which in turn are part of superclusters[3] separated by vast voids. Sky surveys, such as the 2dF survey (Colless et al., 2001), have allowed us to observe this large-scale pattern (see Figure 1.1).

[3]These superclusters are also known as great walls, such as the CfA2 Great Wall (Geller and Huchra, 1989) and the Sloan Great Wall (Gott et al., 2005), the largest known such wall.

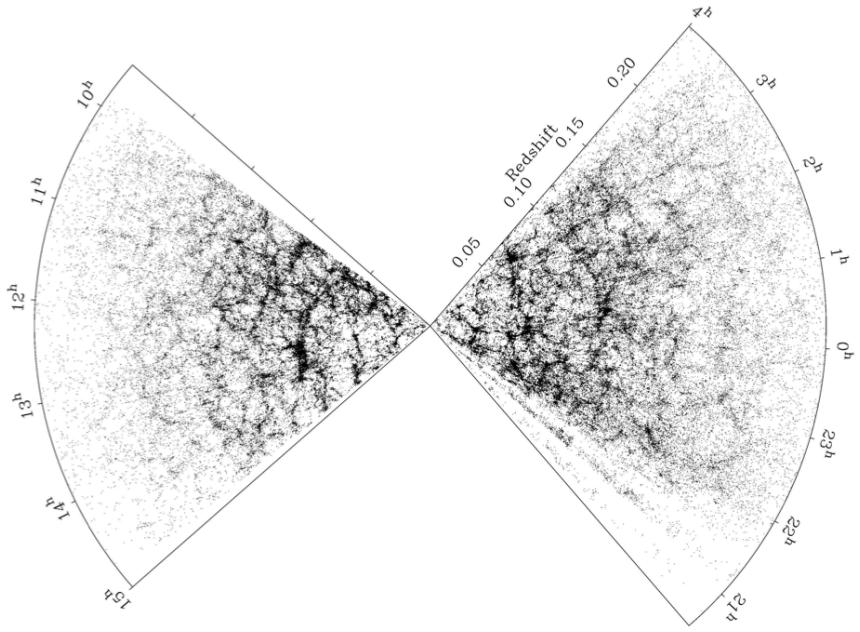

Figure 1.1: This figure from the 2dF survey (Colless et al., 2001) shows the projected distribution of the galaxies in the North Galactic Pole (top) and South Galactic Pole (bottom) strips, as a function of redshift and RA.

1.3 First Light in the Universe and Reionization

The First Stars

As we mentioned briefly above, the first stars (Population III stars, hereafter) in the universe started to emit UV radiation. Simulations employing one-dimensional radiation hydrodynamics explored the evolution of HII regions surrounding Population III stars, investigating the photon escape fraction (Kitayama et al., 2004; Whalen et al., 2004) for a range of stellar masses. The advent of simulations using three-dimensional radiation hydrodynamics (Abel et al., 2007; Yoshida et al., 2007) brought novel results, even revealing formations in the shape of HII regions akin to those that are observed in real star-forming regions. Various studies (e.g. Alvarez et al., 2006, Yoshida et al., 2007) show that ionized regions around the first stars were a lot larger than today's HII regions, meaning that their contribution to reionization can be very

important. In fact, Wise and Abel (2008) showed that Population III stars may ionize as much as one-fourth of the IGM locally. But these stars have very short lifetimes (Schaerer, 2002 finds 2.2Myr for a $200M_{\odot}$ star) so the ionized regions take just a few tens of Myrs to recombine (Alvarez et al., 2006, Wise & Abel, 2008). However, when ionized regions merge, the column density of neutral Hydrogen declines and the stars can then manage to ionize more of their environment. Being metal-free, energy production by these first stars is limited to a proton-proton chain reaction, and so these stars have a higher temperature as well as harder spectra than Population II and Population I stars which came later (Tumlinson et al., 2003), which means that they should exhibit prominent Lyman-alpha and Helium-II lines. The HI ionizing rate of these objects is significantly larger. Tumlinson et al. (2003) found that the ionizing rate for Pop III stars with masses below $100M_{\odot}$ takes double the amount of time taken by Pop II stars to drop to a tenth of its maximum. Bromm, Kudritzki, and Loeb (2001) showed that the amount of ionizing photons spewed out by the first stars with masses above $300M_{\odot}$ is ten times larger than for stars with a normal, Salpeter-like Initial Mass Function (IMF). At this point, however, it needs to be said that a major drawback in these studies is the lack of knowledge of the fragmentation mechanisms that lead to the formation of these first objects, which in turn results in an uncertainty about their IMF (Clark et al., 2011). One other important factor to consider is the clumpiness of the IGM; according to simulations by Pawlik et al. (2009) and Wise and Abel (2008), decreasing the clumping factor helps a lot with keeping the IGM ionized. However, larger simulations are required to investigate global reionization. Later, HII regions resulting from the first stars are overtaken by HII regions arising from galaxies, which are considered next.

The First Galaxies

Determining the contribution of galaxies to reionization is very much dependent on our description of the baryonic processes in these galaxies, such as, for instance, how gas fragments and forms stars in dark matter halos, and indeed these processes are far from understood. This carries implications when one attempts to model the impact these objects had on the reionization process, which entails modelling the escape fraction of the ionizing photons from their host galaxies, which suffers from a degeneracy with the star formation rate (see Wyithe et al., 2010). Therefore, we see that we have two open parameters: (1) the escape fraction of ionizing photons and (2) the star formation rate. Simulations and semi-analytic models (e.g. Choudhury and Ferrara, 2006; Ciardi et al., 2000, Benson et al., 2006) have been employed in an attempt to understand the impact of these first galaxies upon the reionization of the Universe. Such models would benefit greatly from observations of the high-redshift universe (as we shall see further in Section 1.4 and thereafter) which could be used to tune these models and constrain free parameters.

Quasars

Quasars (Quasi Stellar Objects) are energetic active galactic nuclei whose power derives from gas accretion onto black holes in their centres. Compared to stellar sources, they have an ionizing photon escape fraction that is about an order of magnitude higher (Barkana and Loeb, 2001), and a harder spectrum resulting from energy radiation via black hole accretion, so quasars can indeed be more efficient at reionization. Volonteri and Gnedin (2009) conclude that whilst by $z \sim 6$, the contribution to reionization by quasars does not exceed 50% at best, more likely being below $\sim 20\%$, at $z \approx 8$ all their models suggest that quasars are responsible for between 50% and 90% of reionization. Most of this quasar reionization budget comes from massive black holes with mass $< 10^6 \mathrm{M}_\odot$; as Volonteri and Gnedin note in their work, these are fairly

small and low-luminosity massive black holes that do not contribute to the bright end of the quasar luminosity function, and so are challenging to explain away by simple extrapolation of the quasar luminosity function. For this reason, constraining the evolution of the accreting massive black hole population at $z \lesssim 10$ will have to await the James Webb Space Telescope.

1.3.1 Cosmological Constraints on Reionization from the Cosmic Microwave Background

The Cosmic Microwave Background provides us with a constraint on the first light in the Universe. By the time the Universe has finally emerged from the dark ages, the electrons that have been freed from atoms can resume scattering the CMB photons via Thomson scattering. This results in a damping of the acoustic peaks. Since the Universe is not opaque anymore, the mean free path of the photons grows to about the size of the horizon - so this damping is inclusive of all scales, which means that the CMB fluctuations undergo a general damping as a direct imprint of the reionization process (Serjeant, 2010; Haiman and Knox, 1999).

In addition to this suppression of acoustic peaks, reionization has an effect upon the polarization of the CMB. Primordial CMB polarization comes about only through scattering of the CMB photons, and therefore polarization can be expected to be a sensitive probe of the reionization state of the universe. In ΛCDM, the total electron scattering optical depth, τ, is given by (Hu, 1995):

$$\tau = \frac{0.041\Omega_b h}{\Omega_m}\left(\sqrt{1-\Omega_m+\Omega_m(1+z)^3}-1\right) \tag{1.15}$$

This large-scale[4] polarization signal has been detected in WMAP observations

[4]There exists also a small-scale reionization signal (kinetic Sunyaev-Zeldovich effect) arising from (a) patchy reionization and (b) the Ostriker-Vishniac effect, but this lies beyond the scope of this discussion.

and the 7-year analysis by Larson et al. (2011) gives a value of $\tau = 0.088 \pm 0.015$ which gives a reionization redshift (assuming instantaneous reionization from the neutral state to the fully ionized state) centred about $z = 10.5 \pm 1.2$. Apart from this cosmological constraint on Reionization from analysis of WMAP data, there exist also astrophysical constraints on reionization, which are discussed in later sections.

1.4 Observing the High-Redshift Universe

Now that we have seen some of the theoretical underpinnings of our current understanding of the early universe, we shall turn our attention towards observational efforts to probe these early times of the universe's history. Understanding the properties of the early universe entails studying distant populations of galaxies, deriving information in the form of, for example, the UV and Lyman-α luminosity functions, and the star formation rates. $z = 1$ provides a rough distinction between low and high redshift, since as noted in Dickinson (2003), the range lying below this value has been studied well by magnitude-limited surveys, whereas most development beyond $z > 1$ has been achieved via specially designed methods. Ellis (2008) stresses the importance of carrying out observations of the early universe, rightly noting that the accepted standard model is not able to match fundamental properties of the local universe without invoking various forms of feedback mechanisms, which are commonly in use in the literature; as remarked, focusing our observational efforts to better understand the early universe would help to assess the extent to which these models are correct. Observations of galaxies beyond $z \sim 7$ are crucial to address unresolved mysteries about how they form. According to predictions of Cold Dark Matter models, galaxies are built up hierarchically via mergers of dark matter halos (for example, see Stewart et al., 2009; Springel et al., 2005). A semi-analytic approach is adopted to describe the detailed processes of baryonic physics (which are not well understood)

and form galaxies in these halos. Observational studies are required to adjust the free parameters of these models, which can be tweaked to fit various scenarios. Therefore, by studying the properties of these very high redshift galaxies, observed at a time when the universe was still very young, we can investigate the premises which underpin models of galaxy formation.

1.5 The Search for High-Redshift Galaxies

The search for galaxies at high redshift beyond $z = 1$ has utilized various methods, extensively reviewed in Stern and Spinrad (1999) and Dickinson (2003). The following draws a summary of key points about some commonly used techniques. One method has been to carry out (the afore-mentioned) magnitude-limited redshift surveys, for example the DEEP2 Redshift Survey (Davis et al., 2003) and Caltech Faint Galaxy Redshift Survey (Cohen et al., 2000). The drawback with this method is that most objects bright enough to be probed with current ground-based observatories lie at lower redshifts by comparison. A second method in use is gravitational lensing, which is a prediction of general relativity. This method entails using a foreground galaxy or cluster of galaxies to magnify the light from more distant objects (see Richard et al., 2004). Using this method, one can acquire observations with a larger signal to noise ratio. Additionally, it enables one to find sources which are simply not bright enough to be detected unless they are magnified by these gravitational lenses. A third method used in high-redshift searches exploits the fact that the universe was indeed a very active place in the past. AGN were prevalent in the high-redshift universe, and radio galaxies are located in dense environments, so the location of these exotic sources is often used, e.g. in Kurk et al. (2000, 2004); Venemans et al. (2007), as a starting point to extend the search for high-redshift galaxy clusters. Furthermore, radio galaxies are located in some of the most massive systems (De Breuck, 2006),

the properties of which provide us with a useful insight into galaxy evolution. Another useful class of objects in the study of the high redshift universe is that of luminous quasars, such as ULASJ112001.48+064124.3, discovered by Mortlock et al. (2011) and discussed in more detail later. The immense brightness of these objects makes them visible across huge distances (although it needs to be said that it can be very difficult indeed to find examples at very high redshifts). However, in the end it is important to understand both 'normal' and active galaxies. Since all these objects are exotic sources not normal galaxies, it is accepted that on their own they would not provide us with a complete picture of the early universe.

The problem one faces when trying to select only high-redshift sources is that these are always swamped by a larger number of lower-redshift ones; indeed, magnitude-limited spectroscopic surveys have demonstrated that the number of high-redshift objects in such surveys is relatively small. Spectroscopic observations provide a reliable way to pin down the redshift. However, attempting spectroscopic confirmation of each individual object that is visible in a deep image is simply too time-consuming to be a feasible option. Therefore, the need arises for an efficient method to reject low redshift contaminants whilst retaining only high-redshift candidates. (Spectroscopy can then be employed for follow-up confirmation of the selected candidates.) There are two main methods in use. One method consists of emission line searches. Young star-forming galaxies in the early universe ionize their dense neutral hydrogen surroundings, and when electrons transition back from the n=2 orbital to the n=1 orbital, Lyman-alpha is emitted. (The Lyman-alpha line is discussed further in Sections 1.7.1 and 1.8.1). These narrow band searches consist of very deep exposures through a filter which allows transmission only through a narrow wavelength range; in the case of interest to us, this filter is designed to detect Lyman-alpha at a certain redshift, efficiently allowing us to select objects located at that redshift. The drawback is that the surveyed comoving volume is limited, which is not quite ideal since high-redshift

galaxies cluster over large scales (e.g. Shimasaku et al., 2003). This is where the next efficient technique comes in. It is referred to as the Lyman-Break technique and is discussed further below.

1.6 Star-forming Galaxies

In 1987, Simon Lilly and Lennox Cowie (Lilly and Cowie, 1987) demonstrated how the flat continuum spectrum of a star-forming galaxy can be used to derive the rate at which heavy elements are produced (Longair, 2006). Although there is no definition set in stone for the term 'star-forming galaxy', a galaxy can be described as being such when the star formation rate (SFR) of the system is sufficiently rapid that it would deplete the galaxy's gas reserves quicker than its dynamical timescale and: Current SFR/Average Past SFR $\gg 1$. A particular feature of star-forming galaxies which is of interest to our current discussion is the flat, blue continuum spectrum mentioned above. In his historical account, Longair (2006) gives a detailed overview of the groundbreaking observations by Lilly and Cowie (1987) that led to the understanding of how this flat blue continuum spectrum of a star-forming galaxy is related to the formation of heavy elements. It is apt to recapitulate below his description of their findings. If a burst of star formation is sustained for a long period, then this results in a flat intensity spectrum in f_ν at wavelengths on the long side of the Lyman limit, beyond which photons have sufficient energy to ionize hydrogen. Later we shall see that $z > 6$ galaxies can be modelled with $f_\lambda \propto \lambda^\beta$, where $\beta \sim -2$. New stars constantly take the place of the O & B stars in these galaxies, which do not live for long - and the intensity is directly proportional to the galaxy's rate of heavy element production, since in nuclear fusion the conversion of H into He is the starting point in the production of metals. The galaxies found by Cowie & Lilly exhibited similar brightness in U, B & V filters; this was taken to imply that a substantial amount of

heavy elements was formed at a redshift of about 1.

1.7 The Lyman-Break Technique

1.7.1 Flux Absorption by Intervening Neutral Hydrogen

It was described above how if there is no dust extinction, a starburst galaxy displays a blue spectrum in the rest-frame UV. However, neutral hydrogen lying between the galaxy and the observer suppresses the flux at wavelengths short-ward of the Lyman limit. The photospheres of O & B stars within the galaxy, its interstellar medium, and the intergalactic medium all contribute to this absorption. Given two filters covering adjacent wavelength ranges, this drop in flux occurs in the bluer filter. The observed wavelength of the Lyman-break changes with redshift, so the precise filter in which the galaxy disappears is redshift-dependent. This is the Lyman-Break technique, which was first applied succesfully by Steidel and Hamilton (1992).

1.7.2 Resonance scattering of Lyman-alpha photons

Let us consider the simple scenario of an electron bound to an atom. An arriving photon which has the same frequency as some particular energy transition of the electron will induce the electron to resonate, as it experiences a force arising from the photon's oscillating electromagnetic field. In absorbing the incoming photon, the electron gets excited and shifts to a higher level, only to de-excite later, in the process emitting a photon in some other direction but of the same energy. The Lyman-alpha line, which originates when an electron in the Hydrogen atom shifts from the $n = 2$ level to occupy the $n = 1$ level, is one such strongly resonant line. This electron stays in the $n = 2$ level for an amount of time that is very short compared to the inter-collisional time in the Interstellar Medium. For this reason, ultraviolet light around the wavelength of Lyman-alpha undergoes a lot of scattering. Therefore, for

very high redshift galaxies, further to the absorption of UV radiation blue-ward of the Lyman limit by neutral hydrogen, we expect to see a set of absorption lines in the spectrum of these objects due to the absorption of Lyman-alpha resonance photons by neutral hydrogen along the line-of-sight.

Neutral hydrogen clouds at separate locations along the line-of-sight perceive the photons at distinct wavelengths due to their having been redshifted, each leaving its signature as an absorption feature at a separate location in the observed spectrum blue-ward of the Lyman-alpha emission line (see Figure 1.2). The resulting set of absorption lines is called the Lyman-alpha forest, and these forest lines cause another break in the spectrum short-ward of Lyman-alpha at the galaxy's emission redshift, an effect that is more pronounced at higher redshifts as the forest becomes even thicker. In common nomenclature, the galaxy is said to "drop out" in the bluer filter, and galaxies discovered using the Lyman-Break technique are termed i-, z-, Y- (etc.) drop-out galaxies (corresponding to redshift 6, 7, 8-9 respectively) depending on the filter in which they disappear from view.

In 1992, Charles Steidel and collaborators used this method to discover star-forming galaxies at $z > 3$ with the aim of discovering those objects which cause the Lyman-limit absorption systems in quasar spectra. The same method was eventually used for the purpose of selecting $z \sim 3$ Lyman-break galaxies, as reported in Steidel et al. (1998).

Strong features in the spectrum of radiation emitted by these objects can be detected in certain filters but not others. The method whereby one obtains the photometric redshift depends precisely on this feature to obtain a rough estimate of the redshift of a galaxy. The flux measured in a number of carefully selected filters gives a rough estimate of the object's Spectral Energy Distribution (SED). There are several spectral features present in the SEDs of galaxies, so this means that for a certain population of galaxies at some particular redshift, the precise position on a colour-colour

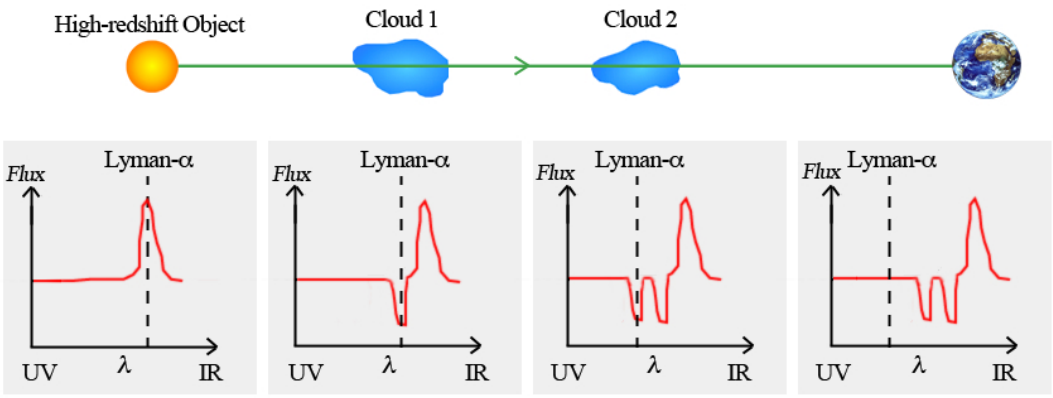

Figure 1.2: This figure shows how neutral hydrogen clouds at separate locations along the line-of-sight perceive the photons at distinct wavelengths due to their having been redshifted. This means that each cloud ends up leaving its signature as an absorption feature at a separate location in the observed spectrum blue-ward of the Lyman-alpha emission line.

plot is restricted to a small location which depends on the redshift, so the measured colours yield a rough value of the redshift (Mo et al. 2010). Of course, not all galaxies have the same intrinsic spectral energy distribution, so this method's selection efficiency depends also on the underlying galaxy SED as well as the magnitude. Indeed, objects such as cool Galactic L dwarfs exhibiting pronounced molecular bands can introduce a significant problem since they cannot be reliably discriminated from high-z galaxies. A similar problem arises due to the Extremely Red Object population of evolved galaxies, which lie roughly at redshifts between 1 and 2. It should be noted that while this method makes redshift tagging quite fast, it suffers from catastrophic failure (a term used to refer to the problem of low redshift objects being mistaken as high redshift sources, when using high-redshift selection techniques) and as noted in Mo et al. (2010), has a reasonably high error ($\Delta z/1+z$) of between 3% and 10%, a value sensitive to the filter set used.

1.8 Probing the Redshift Range of The Reionization Epoch

Since the advent of the Lyman-Break technique, our knowledge of the high redshift universe has increased tremendously. The Lyman break method has been applied successfully to ever higher redshift candidates and has now been employed to identify objects at redshift 6 and beyond (Stanway et al., 2003; Bunker et al., 2004).

Until fairly recent times, working at very high redshifts ($z > 7$) was incredibly challenging since such studies were limited to small fields observed with the Hubble Space Telescope (e.g. Bouwens et al., 2008) or to very shallow wide-area surveys carried out from the ground (e.g. Stanway et al., 2008; Hickey et al., 2010). The advent of the Hubble Space Telescope's Wide Field Camera 3 (WFC3), installed in May 2009, gave the Lyman-Break technique at $z > 7$ a great boost, since WFC3 was equipped with a Near-Infrared detector which not only had a significantly larger field of view than its predecessor, NICMOS, but also better sensitivity. This new camera together with its broad-band filters centered at 1.0, 1.25, and 1.6μm (i.e. Y-, J-, and H-bands respectively) was used to target fields which already had deep imaging carried out with the Advanced Camera for Surveys (ACS), with the aim of identifying optical dropouts, i.e. objects which are visible in the WFC3 (near-IR) images but disappear from view in the ACS (optical) images. Such dropouts are candidate $z > 7$ galaxies. Numerous studies turned up a number of such objects (e.g. Oesch et al., 2010a; Bunker et al., 2010; McLure et al., 2010; Yan et al., 2010; Finkelstein et al., 2010; Wilkins et al., 2011). Similarly, the search for objects which have no flux at 1.0μm and in bluer filters (i.e. Y-drops) is expected to yield $z > 8$ galaxies (e.g. Bouwens et al., 2010; Bunker et al., 2010; McLure et al., 2010; Lorenzoni et al., 2011)

Exploring the $z > 6$ universe is extremely important, especially since it has decidedly emerged that the epoch beyond $z = 6$ marks an important transition in the

history of the Universe. There is growing evidence that the universe at $z > 6$ contains a large fraction of neutral hydrogen. This has come about through observations of quasars lying at $z > 6.2$ (Becker et al., 2001; Fan et al., 2002, 2006) (see Figure 1.3) whose flux at wavelengths short-ward of Lyman-alpha is nearly completely absorbed, suggesting that the universe is optically thick to this line. This was illustrated in Gunn and Peterson (1965), and independently in Scheuer (1965). Schmidt (1965) had found a quasar lying at a redshift of about 2, and Gunn & Peterson noted that the potential occurrence of neutral hydrogen in the IGM could be investigated by using optical filters to observe the continuum spectrum short-ward of the redshifted Lyman-α line. The Gunn-Peterson test, as it has come to be known, exploits the high scattering cross-section of the Lyman-α line at 1216Å. What this means is that when the quasar's UV continuum is redshifted to this wavelength, the radiation ends up being scattered a lot. As a result, if the neutral fraction of hydrogen is high enough, short-ward of the redshifted Lyman-α line one would observe a trough in the spectrum due to the ensuing absorption.

Additionally, as mentioned previously, WMAP studies of the CMB lead us to believe that the universe was completely neutral at a redshift beyond 10 (Spergel et al., 2007; Dunkley et al., 2009). This means that in order to determine what caused the reionization of the universe, we need a better understanding of the $6 < z < 10$ universe.

According to Dijkstra et al. (2004), the number density of high-z AGN is too low to account for this reionization (which result contradicts the previously mentioned findings of Volonteri and Gnedin, 2009), and the proposed alternative process for reionization is UV light which presumably would have escaped from star forming galaxies during this era. Apart from introducing elements heavier than Beryllium into the cosmos, these first stars would additionally have been responsible for a large amount of energetic photons the like of which had only been around before recombina-

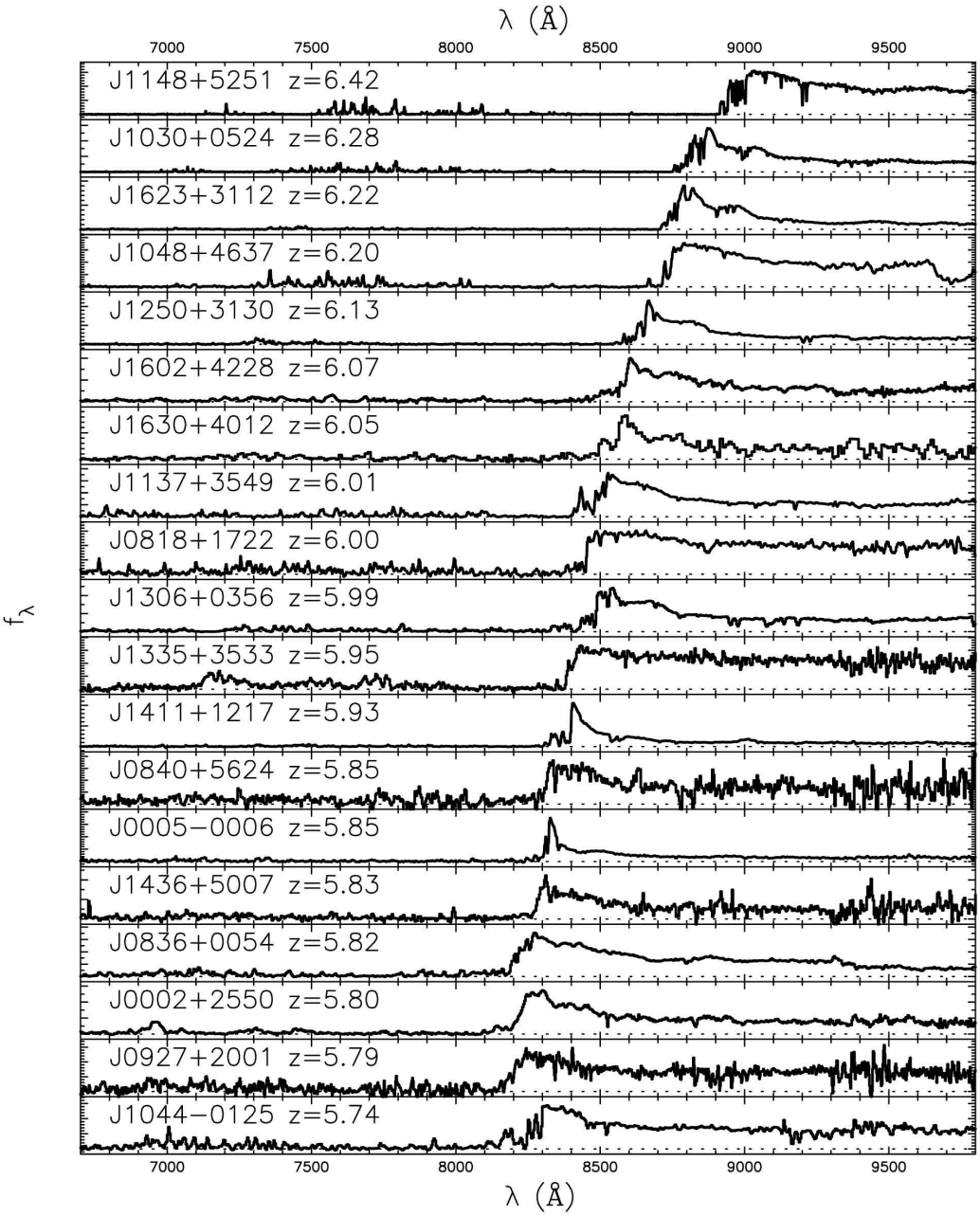

Figure 1.3: This figure from Fan et al. (2006) shows spectra of 19 SDSS quasars lying at $5.74 < z < 6.42$ and clearly illustrates the redshifted Lyman-alpha emission line migrating to ever redder wavelengths (bottom to top), with absorption blue-ward of the line increasing markedly; note how blue-ward of Lyman-alpha, the spectrum exhibits a fairly "rough" character at lower redshifts, becoming plainly smooth and featureless at higher redshifts due to complete absorption.

tion, at a time when hydrogen was still ionized and the photons were being scattered. Reionization is thought to have occurred over an extended period, starting a few hundred million years following the Big Bang and taking about 500 Myr to finish. It is important to gain better knowledge of the global star formation rate at high redshifts and the escape fractions for these ionizing photons.

1.8.1 Using the Lyman-alpha line to probe the Epoch of Reionization

The most prominent spectral line of the very first generation of objects is strongly predicted to be Lyman-alpha, which is the strongest transition of Hydrogen. Galaxies, AGN and Lyman-alpha blobs are the principal classes of objects that exhibit Lyman-alpha emission, with galaxies constituting the largest number density at high redshift. In galaxies, the principal responsible agent for Lyman-alpha emission is deemed to be star formation. Photons spewed out by the star-forming process have energies > 13.6eV[5], thus ionizing the neutral hydrogen component of the Interstellar Medium. Since the Interstellar Medium is very dense, protons and electrons recombine very quickly, and this in turn results in Lyman-alpha emission in galaxies. Also, as a result of gas infall in a host dark matter halo, gravitational binding energy is released as cooling radiation, and this radiation can be carried away as significant, detectable Lyman-alpha emission (Dijkstra, 2009; Haiman et al., 2000b; Fardal et al., 2001). Thus, galaxies could be observable as sources of extended Lyman-alpha emission even before star formation takes place (Dijkstra, 2009). This mechanism has been associated in particular with luminous Lyman-alpha blobs.

In the case of AGN, which make up a tiny fraction of Lyman alpha emitting

[5]13.6eV being the Rydberg constant, found by the Bohr model of the atom to be $-13.6eV = -m_e q_e^4/8h^2\epsilon_0^2$, where m_e is the mass of the electron, q_e its charge, h is the Planck constant, and ϵ_0 is the permittivity of free space; this number represents the amount of energy of the $n = 1$ level of the hydrogen atom.

objects in samples to date (e.g. Ouchi et al., 2008), Lyman-alpha emission would result from gas accretion onto the central black hole. Viscous forces heat the disc of accreting gas, and a fraction of the energy that is produced in this process then goes into ionizing hydrogen. However, since galaxies are by far the most abundant sources of Lyman-alpha emission in the early universe, it is these objects that the discussion shall focus upon. These early galaxies would have commenced reionization in the Universe and reionization in turn should have left its mark on the number counts and clustering of Lyman-alpha emitting galaxies (e.g. Furlanetto et al., 2006), as is discussed in the paragraph below with reference to Figure 1.4.

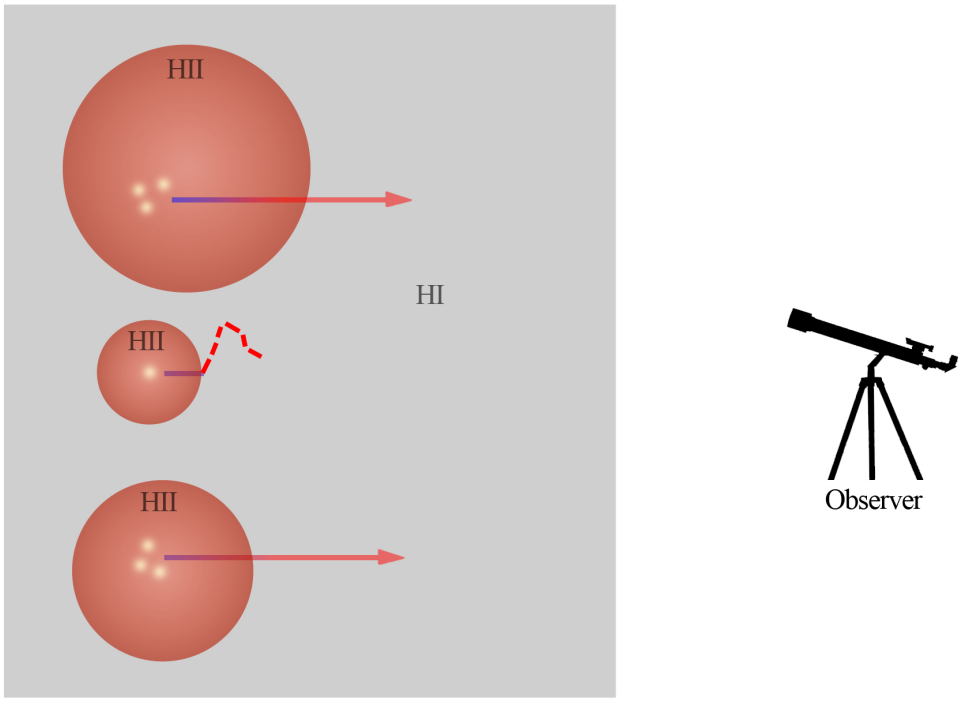

Figure 1.4: This schematic diagram (see Dijkstra et al., 2011) illustrates how Lyman-alpha photons emanating from galaxies in HII regions can propagate unhindered or get scattered depending on the size of the HII regions surrounding them. In the cases illustrated at the top and bottom, the photons are redshifted to a point where they are no longer resonant, managing an unhindered journey to the observer. In the case depicted in the middle, the HII region is too small and the photons are scattered.

By the time they reach the edge of the HII region, some of the Lyman-alpha

photons emitted by galaxies inside large HII regions can become sufficiently redshifted (represented by the colour-changing arrow in Fig. 1.4) such that they are not resonant anymore. This enables them to travel unhindered across the cosmos up to the present day, and an observer at the present time would be able to detect this Lyman-alpha emission. However, in the case of a galaxy located in too small an HII region, the Lyman-alpha photons emanating from the galaxy might not have redshifted enough by the time they leave the HII region. This results in them being scattered in the neutral IGM (represented in the figure by a broken line) and the ensuing low-surface-brightness fuzzy glow is not bright enough to be detected with current telescopes (Dijkstra and Wyithe, 2010; Loeb and Rybicki, 1999). So from all this we expect the Lyman-alpha line to be a sensitive diagnostic of the fraction of neutral hydrogen, and hence a very useful tool in understanding the reionization process.

The detection of this line is fairly recognizable, both due to the strength of the Lyman-alpha transition, and the sudden cutoff shortward of it (see also Chapter 2, Section 2.3.2) because of the high Gunn Peterson optical depth, τ_{GP}, given by:

$$\tau_{GP} = \frac{\pi e^2}{m_e c H(z)} f_\alpha \lambda_\alpha n_{HI} \tag{1.16}$$

where e is the charge of an electron, f_α is the oscillator strength, λ_α is the rest-frame wavelength of Lyman-alpha, m_e is the mass of an electron, c is the speed of light, $H(z)$ is the Hubble parameter at redshift z and n_{HI} is the density of neutral hydrogen in the IGM. At high redshifts, adopting $H(z) \propto h\Omega_m^{1/2}(1+z)^{3/2}$, converting hydrogen density to the present-day baryon density parameter Ω_b, and denoting the mean global density of hydrogen at a given z by n_H, we can rewrite the above equation as in Fan et al. (2006):

$$\tau_{GP} = 1.8 \times 10^5 h^{-1} \Omega_m^{-1/2} \left(\frac{\Omega_b h^2}{0.02}\right) \left(\frac{1+z}{7}\right)^{3/2} \left(\frac{n_{HI}}{n_H}\right) \tag{1.17}$$

where $h = H_o/100\text{kms}^{-1}\text{Mpc}^{-1}$.

Fan et al. (2006) then convert the results depicted in Fig. 1.3 into an optical depth as illustrated in Fig. 1.5. They track the evolution of τ_{GP} across a wide redshift range by making use of their quasar observations for higher redshifts ($z = 4.8 - 6.3$) and data from Songaila (2004) for lower redshifts.

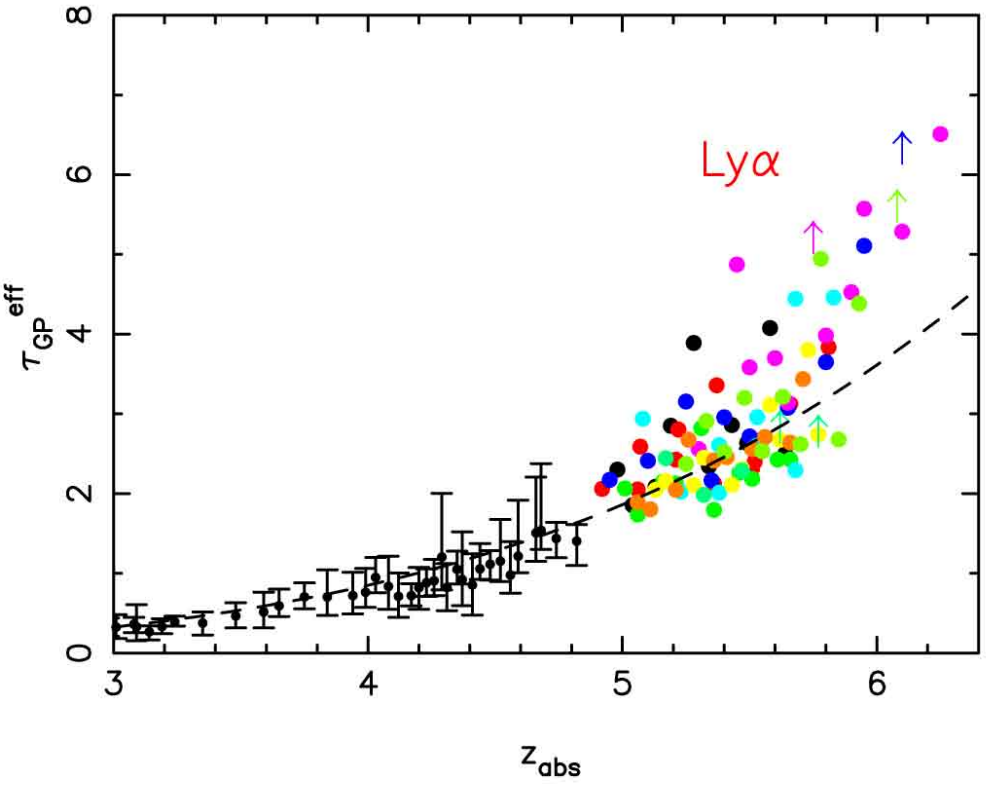

Figure 1.5: This figure From Fan et al. (2006) traces the evolution of the Lyman-α Gunn-Peterson optical depth with redshift. The small symbols denote observations from Songaila (2004) whereas the large symbols represent results from Fan et al. (2006) for measurements of 19 SDSS quasars shown in Figure 1.3. The arrows depict the 2-σ lower limit on the optical depth for Quasars with complete Gunn-Peterson troughs in which no flux was detected.

The key number used to characterize the neutral fraction of Hydrogen is χ_{HI}, which is defined as:

$$\chi_{HI} = \frac{n_{HI}}{n_H} \tag{1.18}$$

Determining the value of χ_{HI} at high redshift is crucial, as it provides us with a handle on the amount of neutral hydrogen present in the universe; thus the evolution of χ_{HI} tracks the reionization history of the universe. Obtaining spectroscopy on very high redshift galaxies in order to constrain this number is one of the main efforts of this thesis. Other groups have also put effort into constraining χ_{HI} and this work is reviewed in the next section.

1.8.2 Constraining χ_{HI}

In this section, we shall first consider spectroscopic surveys at lower redshifts ($z < 7$) and then will turn our attention to recent efforts made by other groups to obtain spectroscopic detection of Lyman-α emission at $z \sim 7$, looking at how these studies at higher redshift compare with those made at lower redshifts, and in particular how the ensuing results are being interpreted as possibly indicating an increase in the neutral fraction of Hydrogen. Later in this thesis (e.g. Chapter 3, Section 3.7.2), these $z \sim 7$ studies are compared with our own observations.

Exploring the $5 < z < 7$ redshift range

In the search for galaxies in this redshift range, emission lines are much easier to detect than the stellar continuum, which is incredibly faint for these dropout galaxies. Indeed, in our spectroscopic observations (which probe the higher end of this redshift range and beyond) the continuum is not detected. Earlier, we saw that star formation results in a prominent Ly-α line, so apart from enabling one to pin down the redshift, this line is an important tracer of the star formation rate. Also, measuring a clustering signal in Ly-α emitters could be another way to investigate reionization. Narrow-band

imaging and spectroscopy have both been used to detect Lyman-α in this redshift range. Both have their strengths; narrow-band imaging can cover larger co-moving volumes, while spectroscopy can go deeper.

Very important work has been carried out via numerous Narrow-Band Lyman-α surveys; the summary here focuses on those carried out with the Subaru Prime-Focus Camera (SuPrime-Cam), which is a mosaic of ten 2048×4096 CCD arrays installed at the prime focus of the 8.3m Subaru Telescope, covering a field of view of $34' \times 27'$. The selection of such objects is normally carried out via the presence of excess flux in the narrow-band filter with respect to a broad-band image, and often by also imposing a colour-colour constraint. (Spectroscopy remains important to avoid low-z interlopers.) Among other studies, work with Suprime-Cam has targeted Lyman-α emitters at various redshifts in this range, e.g. Hu et al. (2004); Ouchi et al. (2005); Ajiki et al. (2006); Murayama et al. (2007); Shimasaku et al. (2006) at $z \sim 5.7$, Kodaira et al. (2003); Taniguchi et al. (2005); Kashikawa et al. (2006) at $z \sim 6.5 - 6.6$, and Iye et al. (2006); Ota et al. (2008); Hibon et al. (2012) at $z \sim 7$. An extensive study that should be mentioned here is that of Ouchi et al. (2010), which presented statistics of 207 Lyman-α emitters at $z \sim 6.6$. Combining the results of several published surveys, Malhotra and Rhoads (2004) argued that the lack of observed evolution in the Lyman-α luminosity function between $z \sim 5.7$ and $z \sim 6.5$ could be interpreted as suggesting that reionization had to be complete by $z \sim 6.5$; this was the first attempt to constrain the neutral fraction.

$z \sim 7$ and beyond

As discussed in Section 1.8, the installation of WFC3 on the Hubble Space Telescope resulted in the discovery of numerous $z > 7$ candidate galaxies; these objects have been the subject of spectroscopic follow-up studies by various groups.

Fontana et al. (2010) used VLT/FORS2 to observe 7 Lyman-break galaxy candidates selected in the GOODS-S field from Hawk-I/VLT and WFC3/*HST* imaging, and other than the one tentative Lyman-α emission line in G2_1408 (HUDF.zD1 in the catalogue of Bunker et al. 2010) which is also targeted by the observations described in this thesis and discussed in later Chapters, they detect no other Lyman-α emission in the rest of the sample.

As part of the same survey, Vanzella et al. (2011) report the detection of Lyman-α emission in 2 objects (at z=7.008 and z=7.109) in the BDF4 field (Lehnert and Bremer, 2003). They note that in this field, 2 out of the 3 observed candidates were confirmed as Lyman-α emitters, in contrast to Fontana et al. (2010) who find only one tentative Lyman-α emitter out of 7 targets. As they observe, whilst it is not possible to draw any statistical inferences basing on just two objects, taken on their own these two confirmed Lyman-α emitters would seem to fit the trend of galaxies with large Ly-α Equivalent Widths observed at $4 < z < 6$, something which would be at odds with the results of Fontana et al. (2010) and would possibly suggest variation across fields, which in turn could suggest that the reionization process at these times was an inhomogeneous one; inhomogeneity in reionization could be explained by a clustering effect, which would arise if objects were tracing overdense, biased regions (Furlanetto et al., 2006). However, the results of the final sample discussed in Pentericci et al. (2011) seem to confirm an overall decline in Lyman-α emitters at $z > 7$. Pentericci et al. (2011) observed 20 z-drop galaxies with VLT/FORS2 and detected 5 Lyman-α lines in their sample. Adopting simulation techniques discussed in Fontana et al. (2010) they report that, on the basis of observations made at lower redshift, the probability of detecting only 5 galaxies in their sample is below 2%, indicating a declining fraction of strong Lyman-α emitters at higher redshifts.

Schenker et al. (2012) presented Keck LRIS observations of 19 sources with photometric redshifts lying in the range $6.3 < z < 8.8$. They reported two convincing

Lyman-α detections (ERS 8496 at $z = 6.441$ and A1703_zD6 at $z = 7.045$), and a marginal detection at $z = 6.905$ for HUDF09_1596. For their discussion, they added the 7 objects discussed by Fontana et al. (2010) such that they could carry out an analysis over a larger sample of objects. They conclude that 24 of their targets (out of 26) have spectral coverage over more than half the likely wavelength range for Lyman-α (given the photometric redshifts using the EAZY code). From simulations they show that out of the combined 26 targets observed by them and Fontana et al. (2010), they should have detected 7-8 emission lines rather than just 2, again arguing for a steep decline in the Lyman-α fraction at $z > 6.3$.

Ono et al. (2012) carried out observations of 11 z-drops in the Subaru Deep Field (SDF) and the Great Observatories Origins Deep Survey North (GOODS-N) using Keck/DEIMOS, detecting Lyman-α emission for 3 objects in their sample, one of which had already been detected at a lower level of significance by Iye et al. (2006).

The only claimed detection of Lyman-α emission in a galaxy beyond $z \sim 7$ is that reported in Lehnert et al. (2010); the reported Lyman-α emission would place the object at $z = 8.55$. However, this claim could not be confirmed in our own observations of the same object. The full discussion of the observations, results and analysis of this object be found in Chapter 3, Section 3.9. Failing confirmation of this reported galaxy, at the time of writing, the highest redshift galaxy which has been spectroscopically-confirmed remains GN-108036 reported by Ono et al. (2012) to be at $z = 7.213$.

In this high redshift regime, one must not forget Gamma Ray Bursts (GRBs), which are short-lived bursts of gamma-rays which are followed by an afterglow detected over the whole electromagnetic spectrum. They are so bright that they can easily outshine their host galaxy and so can be detected up to very high redshifts, such as GRB 090423 at z=8.2 (Salvaterra et al., 2009; Tanvir et al., 2009). Spectroscopy of this afterglow often reveals metal absorption lines which allow for a better un-

derstanding of the metal and dust content of their environment. GRBs have stellar origins and are hosted in objects whose metallicity is moderate to low (Tanvir, 2010), so they should happen at an early stage in the Universe's history. For this reason, as Tanvir (2010) explains, they are perfectly placed to inform us about star formation and galaxy evolution during the phase of reionization.

This is the context within which the work discussed in this thesis has been carried out. As can be seen, various surveys have identified several $z > 7$ and $z > 8$ candidate galaxies, selected using the Lyman break technique. Spectroscopy undertaken on samples of these objects indicates that there seems to be a turnover in the expected number of Lyman-α emitters when compared to studies at lower redshifts. For the work presented in this thesis spectroscopy was undertaken on several high-z candidate objects, in an attempt to further investigate this early epoch in the universe's history.

Whilst this discussion has focused mostly on galaxies, a high-z object which is worthy of mention is the $z = 7.085$ quasar ULASJ112001.48+064124.3 (Mortlock et al., 2011). As described in Willott (2011), this object can be used to inform us about the ionization state of the IGM at this epoch via two key signatures: the shape of the Lyman-α emission line, and the implied size of the self-ionized region surrounding the quasar, which is partly dependent on the neutral fraction of the IGM before the quasar is switched on (Bolton and Haehnelt, 2007). The Lyman-α emission line of this object exhibits attenuation in the blue-wing, indicative of intervening neutral hydrogen, and the size of the self-ionized region ($R_{NZ,corr} = 2.1 \pm 0.1 Mpc$) is much smaller than near zones in other high-redshift quasars of similar luminosity. This object is also particularly significant due to the estimated mass of its central black hole, $M_{BH} = \left(2.0^{1.5}_{-0.7}\right) \times 10^9 M_{Sun}$; this is higher than expected at this very high redshift and as noted in Mortlock et al. (2011), places very strong constraints on the viable models of accretion mechanisms, merger histories and black hole seed formation.

1.9 Two considerations: Dust and IGM opacity

Both Lyman-alpha and continuum photons can be subject to absorption by dust grains in the Interstellar Medium (ISM) and only a small amount of both of these two kinds of photons will manage to escape from the galaxy without undergoing attenuation by dust (Dayal and Ferrara, 2012), which comes from supernovae and Asymptotic Giant Branch stars in the galaxy. However, the latter have been shown to be less significant at a redshift of about 5.7 and beyond (Dwek et al., 2007, Todini and Ferrara, 2001), the reason being that beyond that redshift, the timescale over which these stars evolve, which is typically of about 1-2 billion years, is actually longer than the age of the universe itself at these redshifts. On the other hand, the IGM suppresses only Lyman-alpha photons.

It has been shown (e.g. in Dayal et al., 2011) that there is a degeneracy between grain properties or dust clumping in high redshift galaxies and the ionization state of the IGM. In order to be able to securely constrain the ionization state of the IGM, it is crucial to understand the relative escape fraction of Lyman-alpha in contrast to continuum photons (Dayal et al., 2011). As Dijkstra (2011) notes, it is immaterial to current observations of the local IGM whether Lyman-alpha photons are scattered into an undectable low surface brightness glow, or if the scenario has dust grains absorbing photons which are then re-radiated in the infrared (IGM Opacity / Dust degeneracy); in either of these two cases, an observer would simply note a suppressed Lyman-alpha flux from the source.

It is important to pay attention to this degeneracy, as this factor has a direct bearing upon any attempt to constrain the IGM's effect on the visibility of Lyman-alpha. Dijkstra et al. (2011) stresses that in order to get a handle on the local IGM opacity, it is essential to gain understanding of how Lyman-alpha transport is affected by galactic winds, which can reduce the opacity of the local IGM. Comparing the shape of the Lyman-alpha line with that of the Balmer (n=3 $\rightarrow$ n=2) non-resonant

line would help in this regard, and indeed some of the first such studies have been carried out by Finkelstein et al. (2012) and McLinden et al. (2011). Also, these winds can cause Lyman-alpha photons to be Doppler-shifted to frequencies on the red side of the galaxy's systemic velocity. Scattering in galactic outflows can change the shape of the Lyman-α line such that a fraction of the emitted Lyman-alpha photons actually still manages to reach the observer, despite having a fully neutral IGM (Dijkstra, 2011); this process is explained in Figure 1.6.

So the interpretation of Lyman-α lines is limited by the assumptions of the underlying models, and dust extinction can give rise to considerable uncertainty in this interpretation. Observations of the Balmer lines for very high redshift objects could provide a handle upon extinction, because whilst dust could extinct the Lyman-α line and the UV continuum by equal amounts, it may extinct the Balmer lines less (Santos, 2004); this would allow one to obtain an estimate of the extinction of Lyman-α and then correct for it. Having said this, as Santos also notes, it could very well be the case that dust extincts resonant Lyman-α photons more than UV continuum photons, since the former resonantly-scattered photons have to travel an extra path-length though the galaxy before managing to escape. This effect cannot be constrained by any direct observable; a Balmer line-derived extinction-corrected star-formation-rate would, however, serve to provide an upper limit on the flux of the Lyman-α line (Santos, 2004). However, this kind of measurement will have to await the James Webb Space Telescope.

Now that we have provided the necessary background and set the scene, we shall outline the structure of the rest of this thesis. Chapter 2 gives a general overview of the workings of CCDs and Infrared Arrays, which are used to capture the faint light from the very distant galaxies discussed in this thesis. It also outlines the methodology used to carry out spectroscopic observations, reduce the data and analyse it. Chapter 3 deals largely with one of the observational projects targeting z-band

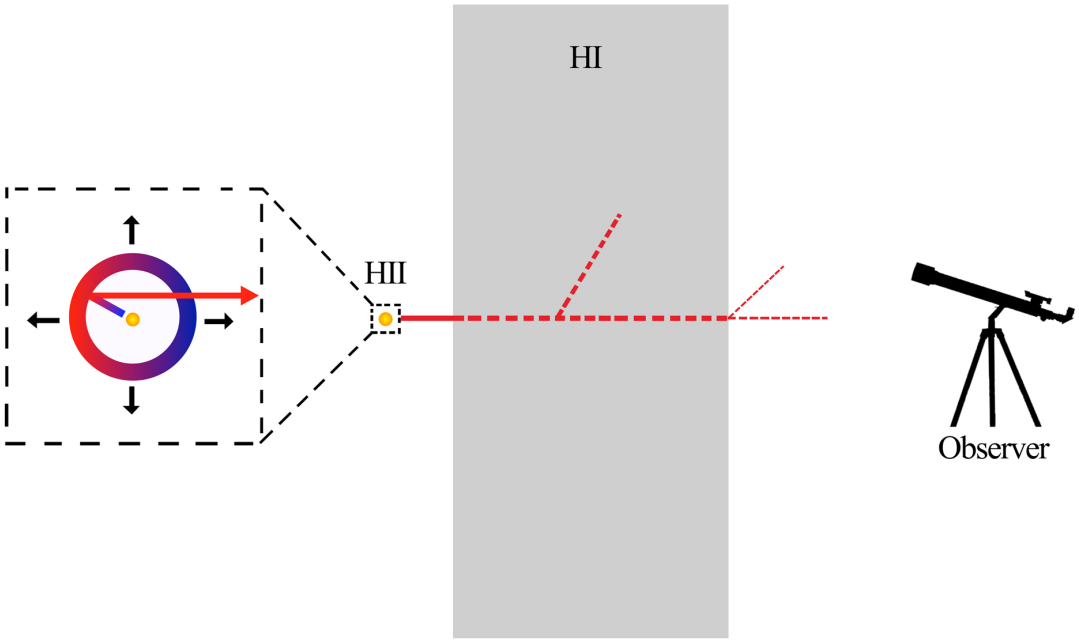

Figure 1.6: This schematic diagram, adapted from Dijkstra (2011), illustrates how outflows surrounding a star-forming region (which in this figure is represented by the expanding ring) can doppler-shift Lyman-alpha photons to a higher redshift, possibly pushing them to a wavelength that lies red-ward of the Lyman-alpha resonance. Thus, the Lyman-alpha photons are shifted into the red wing of the line, and here the opacity of the IGM is lower, meaning that it is possible for a certain fraction of Lyman-alpha photons to reach the observer, even in the absence of a large HII bubble surrounding the source.

dropouts (z $\approx$ 7) and Y-band dropouts (z $\approx$ 8.5) using the Gemini Infra-Red Spectrograph (GNIRS) at the Gemini South Telescope and The X-Shooter spectrograph at the Very Large Telescope (VLT). It provides details about the data reduction, presents the results of our observations using these two spectrographs and lays out the analysis of these results. The reader can also find a detailed discussion of a particular Y-drop, HUDF.YD3 (Bunker et al., 2010) which, as mentioned earlier, was claimed by Lehnert et al. (2010) to exhibit an emission line at 11616Å consistent with Lyman-α emission at z=8.55. This target was observed with VLT/X-Shooter and the Multi-Object InfraRed Camera and Spectrograph (MOIRCS) on the Subaru

Telescope and the findings on this target are presented. Chapter 4 is devoted to the second observational project targeting a large number of z-band dropouts with the VLT FOcal Reducer and low dispersion Spectrograph (FORS2). The data reduction is discussed in detail, the results from the observations are presented and the results analysed. Finally, Chapter 5 provides concluding remarks and outlines the prospects for future efforts in this field.

Chapter 2

Observations and Reduction

The search for the Lyman-alpha emission line in very high redshift galaxies is a difficult task for many reasons. The observations themselves are very challenging, requiring very good and stable seeing ($\sim 0''.5$) and long integration times. In addition, for the highest redshift sources, Lyman-alpha emission is redshifted to the infrared, where the sky background is very variable. Near-Infrared detector arrays for astronomy are relatively recent, arriving in the late 1980's. The first detectors had a small number of pixels (e.g. NICMOS on the Hubble Space Telescope had a 256×256 array), but now, near-IR arrays such as Teledyne HAWAII detectors[1] boast 2048×2048 pixels, with a quantum efficiency (QE) of 70% down to 400nm, and low read noise levels and dark current (Blank and Cabelli, 2012). However, near-IR detectors still remain more problematic than optical arrays. This, combined with a variable sky background, makes data reduction far from trivial. Any potential signal is much fainter than the sky background, and therefore adopting proper reduction techniques is of paramount importance. Very often, standard reduction pipelines supplied by the observatory are not up to the task of reducing such data in an optimal manner and therefore appropriate reduction procedures which are tailored for the task at hand

[1]For further information on the type of array installed in the instruments used for the work presented in this thesis, refer to later sections which discuss each instrument separately.

have to be developed.

This chapter will provide a general overview of the methods and techniques employed in carrying out observations and reducing astronomical data, with a view to laying the ground work for the following chapters, which will give a more detailed, instrument-specific description of the precise reduction methodology employed for our own observations. It begins with a general overview of the relevant concepts pertaining to data acquisition with Charge Coupled Devices (CCDs) and near-IR arrays, and the associated problems which need to be rectified. Following this, it gives an outline of what the overall reduction process entails. Later parts of the chapter describe some of the most common measurements that are necessary for any subsequent analysis. The overall discussion is fairly generic, but has been moulded around the observations and techniques employed for the work presented in this thesis.

2.1 CCD Data and Calibration

An astronomical observing session consists only partly in acquiring the data of the astronomical sources. One has to spend a significant amount of time obtaining CCD frames of calibration data, which are used later in the preparation and calibration of the science frames - a process which is referred to as Data Reduction. Raw data from a scientific instrument, such as a spectrograph, exhibit numerous flaws which need to be corrected prior to presenting credible scientific results.

The details of what calibration frames are required for a specific observation, and the precise manner in which data reduction is carried out, depend both on the type of observation as well as the instrument being used. This section provides a general outlook of the problem, first introducing the basic concepts and outlining the commonly required calibration frames, and then discussing some of the reduction techniques in use, focusing in particular on tasks relevant to the observations carried out for the

work presented in this thesis. (A more detailed instrument-specific discussion will be provided in later chapters.)

2.1.1 The Workings of CCDs and Near-IR arrays

A CCD (Charge Coupled device) functions by converting received photons into electrons, which are stored in pixels. Essentially, a CCD is an array of MOS (Metal-Oxide-Silicon) capacitors forming part of an electronic system whose function is to measure the charge held per pixel following an integration. Each pixel has a limited capacity. During an exposure, arriving photons hit individual pixels and subsequently are converted into electrons which are then held in each pixel's well. The number of electrons that are stored in each pixel is given by a value whose units are ADU (Analogue to Digital Unit) or DN (Digital Number). Thus, the number of electrons in a particular pixel's well is proportional to the number of photons that fell upon that pixel. (It should be noted that the number of counts in a given pixel is connected with the number of photoelectrons via the conversion of electrons to ADU, but normally the two of them are not equivalent.) If we adopt a notation similar to that in Chromey (2010) and denote by $A[x, y]$ the analogue quantity recorded by the CCD sensor at pixel coordinates (x, y), and let $R[x, y]$ be the digital response of the array (e.g. analogue voltage converted to a digital value) at the same coordinates, then the *gain* is defined as the differential change in $A[x, y]$ that would produce a change of just one ADU in $R[x, y]$, that is:

$$\text{gain} = g[x, y] = \frac{dA[x, y]}{dR[x, y]} \tag{2.1}$$

In a CCD, the read-out strategy, or charge-coupling (from which the name of the device is derived), transfers electrons from one pixel to a surrounding one. Now, ideally, every single received photon would be converted to an electron and all these

electrons would in turn be counted accurately during read out. In practice, however there exist a number of factors which bring about noise into the data. These noise sources are discussed below. It is important to point out that near-IR arrays differ from CCDs in that they do not clock the charge out like CCDs.

2.1.2 Problems inherent to Raw Data from a CCD

In this section we highlight some of the main problems inherent to CCD detectors, which problems need to be mitigated by taking suitable calibration frames to be used during the reduction process, as described later. Here, we focus our attention on the problems themselves and their origin.

Bias

If a CCD sees no light, and a zero-length exposure is made, it will still end up registering a certain positive value (offset) for a pixel. This leads to a bias which is added to every frame.

The Various Types of Noise

The usefulness of a detector depends a lot on the amount of noise inherent to the device. The first noise source that shall concern us here is related to the temperature of the device. Even if no exposure whatsoever is made, a detector will produce a response during a given integration, i.e. even if the detector sees no light, thermal excitation leads to a trickle of electrons, which are subsequently collected by the CCD's potential wells resulting in **dark current**. The ensuing problems are numerous. Dark current contributes an amount of unwanted electrons to the number of electrons which would ideally be generated in a pixel only by a real astronomical signal, and this number has to be subtracted in order to retrieve the original number of electrons per pixel. So this quantity represents a constant offset value. If the as-

tronomical signal is weak, then the task of registering it can be rendered extremely difficult, which in turn would call for longer exposure times in order to increase the signal level arising from the astronomical source. At worst, the dark current level can be sufficiently high that it ends up saturating the potential wells in a very short time. Additionally, dark current has its own statistical variation, introducing noise to the signal. This noise is Poissonian in nature, which means that we can describe it as follows. If we denote the dark current per electron per second per pixel in an aperture by DC, then the noise within the aperture is given by: $\sigma_{DC} = \sqrt{DC \times n_{\rm p} \times t}$ where $n_{\rm p}$ is the number of pixels in the aperture and t is the total time of the exposure. Finally, it should also be mentioned that because of imperfections in manufacture, the dark current is not the same for every individual pixel. To mitigate dark current, which for near-IR detectors can be significant, CCD sensors are actively cooled.

Another source of noise in data is due to the random arrival of the photons themselves; this is known as **shot noise**. Since the arrival of photons is a random process, where the arrival of an individual photon is an independent event, the arrival of a certain photon cannot be predicted with absolute accuracy and for a large number of events N, the process is described by Poisson statistics such that $\sigma_{\rm shot} = \sqrt{N}$. We can subdivide shot noise in two categories: (1) Shot noise from the source, and (2) Shot noise from the sky. If $N_{\rm source}$ is the count rate per second of electrons from the source, then the total number of photoelectrons accumulated in time t is $N_{\rm source} \times t$ and the associated noise is $\sigma_{\rm source} = \sqrt{N_{\rm source} \times t}$. Similarly, denoting the count rate of photoelectrons from the sky by $N_{\rm sky}$, the shot noise from the sky per pixel is then: $\sigma_{\rm sky} = \sqrt{N_{\rm sky} \times t}$. (Note that the sky shot noise enclosed by the aperture is: $\sigma_{\rm sky} = \sqrt{n_p \times N_{\rm sky} \times t}$ where n_p is the number of pixels within the aperture.)

The third kind of noise is known as **readout noise**. In order to describe better the origin of readout noise, it is instructive to highlight briefly the principal stages in CCD operation. First, electrons which have been liberated by striking photons are

transferred to an electronic component called an amplifier. The amplifier measures the voltage resulting from this charge. An Analogue to Digital Converter (A/D) then converts the voltage into a discrete voltage value which is then transformed into counts, the previously mentioned Digital Numbers / Analogue-to-Digital Units, which are finally output by the device to the computer to be registered as the value of a pixel. Readout noise can be considered as follows. Firstly, every time charge is transferred from the CCD to the Analogue to Digital Converter (A/D), the process is not faultlessly repeatable, in that the conversion of a given pixel with a particular charge will produce a value that varies each time this is carried out; besides, the electronic components introduce noise which is not discriminated from the electrons from a genuine signal (Howell, 2006). The mechanism underpinning an array's readout is the transfer of one single pixel at a time of the array charges through the amplifier that measures the voltage induced by the transferred charge. The amplifier also introduces an error when quantifying the charge carried by a group of electrons; inherent to this process there is some statistical variation, which is readout noise. This trickling flow though a single amplifier presents a congestion. In order for the amplifier to accurately measure the voltage, readout has to be carried out slowly, and the time required is a function of the size of the array. This long readout time can end up setting a restriction on the maximum number of pixels, as the readout process could end up taking too much valuable time, which is undesirable. Precisely for this reason, CCDs often have more than one amplifier, e.g. one amplifer in each corner, each reading a fourth of the array, such that the readout time is decreased by a factor of four. There exist various methods for reading out the CCD (e.g. orthogonal-transfer, Frame-transfer, Low-light-level, e.g. see Mackay et al., 2004) each of which offers certain specific advantages. However, the details of these methods lie beyond the scope of this discussion.

Response Variation across the Detector

Whilst nowadays CCD arrays are made to meet very high standards, they are still not perfect, and each individual pixel responds slightly differently to incoming photons of light. Apart from this variation ingrained in the quantum efficiency of the detector, defects external to the detector (such as dust particles, vignetting and other problems) could also be present. This variation is usually best counteracted by acquiring a *Flat Field*.

Linearity

An ideal detector would be linear, as then there would exist a straight correlation between its response and the arriving photons. However, in practice, a detector deviates (sometimes significantly) from this ideal scenario and is linear only over a restricted range. A pixel will saturate when its potential well fills up (which is when the MOS capacitor is not able to store any more charge) and cause blooming, which is to say leaking its charge onto surrounding pixels (see Howell, 2006 for details).

2.1.3 Mitigating the problems: Calibration Frames

Bias Frames

To eliminate the bias level, one reads out the detector with the light path blocked and with no integration time; the resulting frame is called a bias frame, which embodies an electronic offset that is added to every frame. The normal procedure is to acquire several bias frames and then combine them so as to alleviate noise issues. This also has the added advantage of mitigating cosmic rays, which might occur throughout the acquisition of bias frames. Combining the separate bias frames by means of taking their mean is not ideal if cosmic rays are present, as this would only diminish their influence but not eliminate them completely. The alternative is to take the median

instead, which is better suited to rejecting them. (It is best to use an odd number of frames for the median.) The master combined bias frame is then subtracted from all the scientific exposures (i.e. the exposures containing scientific data) in order to eliminate the bias level.

Flat Fields

The procedure required to correct response variation across the detector by means of an appropriate flat field is indeed a principal aspect in the preparation of science data. In basic terms, the procedure requires the telescope to be aimed at a uniformly blank source of light and taking an exposure of this source, choosing an exposure time that does not result in an underexposed or saturated final output. The resulting image is called a flat field. If the sensitivity of the setup is perfectly identical across the detector, then a uniform signal should create a uniform result. However, as we have seen before, problems such as vignetting, dust, as well as variation in the detector's efficiency, lead to a departure from this ideal uniformity. By applying a flat field to the science data, non-uniformity can be eliminated.

In practice, several complications make flat-fielding far from a straight-forward procedure (see Djorgovski and Dickinson, 1989). The instrument setup might undergo alterations during the time between the acquisition of the flat fields and that of science data (e.g. slight shifts might occur when the telescope is moved to point at a different target, new dust particles might fall somewhere etc.), which can be quite problematic. Also, adequate uniformity is not easy to achieve. Finally, the sensitivity of a system often has a wavelength dependence, so this introduces the requirement that the spectrum of the source used to acquire a flat field is similar to that of the astronomical object.

The question that comes up next is: What source is suitable for the acquisition of a flat field? There exit three different sources that can be used for this, namely

the dark night-sky, the twilight sky, or a blank nearby source such as a uniformly-illuminated source inside the observatory itself. All of these offer their own specific advantages. Each of these are briefly reviewed below.

- **Dark Night-Sky Flats** are acquired when there is no moon in the sky. They are a good choice when observing very faint objects (such as is the case with our own targets for instance, which are much dimmer than the sky), especially in the infrared region of the spectrum which, as has been mentioned previously, is quite bright. Also, since the source of illumination is the sky itself, the spectrum of a night-sky flat is very similar to that of the background, which is a useful advantage. One obvious disadvantage to using dark night-sky flats is that due to the low photon count when exposing the CCD to just a patch of dark sky, the exposure time might be required to be quite long, consequently wasting valuable time. Also, with the onset of darkness, stars are likely to be present in the image, so to alleviate this, one normally tries to target a field which is sparse. Often, one then uses a common technique to further overcome this problem, namely to dither the observations, that is to say shift the telescope between separate exposures such that when all the exposures are combined using a median, the stars are easily rejected (Tyson, 1990).

- **Twilight Flats**, as the name implies, are taken during twilight. However, the sky during twilight presents numerous challenges for flat-field acquisition. A twilight flat has the benefit of having the correct luminosity. But the sky during twilight is far from uniform, brightening considerably toward the horizon. Aiming the telescope at the zenith, one can use a target which is sufficiently uniform over a very small region (see Chromey and Hasselbacher, 1996). Drawbacks include the fact that the time-window to acquire an adequate twilight flat is quite limited (see Tyson and Gal, 1993), the problem of the afore-mentioned brightening towards the horizon, which undermines the extent of uniformity,

and a spectrum which is markedly different from that of astronomical objects, or even the night sky for that matter.

- **Dome flats** are the third and last strategy; the basic method entails aiming the telescope at a blank white surface on the dome's interior. Since there is no requirement to take dome flats during nighttime, valuable time can be saved. Additionally, one can choose both the brightness and the spectral distribution. However, twilight flats are considered to be a better choice (see Mackay, 1986).

Once the flat field frames are acquired, the bias is removed from each flat field frame and any necessary corrections to account for non-linearity are applied. Every individual frame is usually normalised such that the median pixel is equal to one ADU. This makes it easier to combine the separate frames. Combining the frames serves to get rid of cosmic ray strikes (and any stars, if the flat is a dark night-sky flat or twilight flat).

2.2 From Start to Finish: An Overview of the Data Reduction Process

Now that we have looked at the basic concepts related to CCD imaging, some of the associated issues which have to be accounted for, and the different kinds of calibration frames required, we shall next have a brief look at how these frames are used to reduce the data from their raw format to a form useable for scientific analysis. The specific reduction method most suitable for a particular dataset depends both on the particular instrument being used and on the kind of target being observed, so the description given here is a fairly general overview. That being said, the story here is largely told in the context of observations of the high redshift universe; an instrument-specific description of the reduction process is described in later chapters.

2.2.1 Calibration and Science Data Preparation

One of the intitial steps in the reduction process is to combine the individual bias frames into a master bias frame. This is then subtracted from each flat field frame. If the exposure time for the flats is long, it is sometimes also necessary to subtract a dark frame[2] from every individual flat field frame. The prepared flat field frames are then combined together to create a master flat field. The master bias frame is next subtracted from individual science data frames, and these data frames are then divided by the master flat field, in so doing ridding the science data of the undesirable effects of out-of-focus dust, vignetting, non-uniform detector response and other sources of non-uniformity in the output.

In the case of spectroscopic observations, such as the observations presented in this thesis, the spectra very often exhibit some degree of curvature in the following sense: referring to Fig. 2.1 which considers a spectrum with a slit oriented such that it is parallel to the y-axis, the direction of spectral dispersion would be expected to run perfectly horizontally, but often this is not the case, as the figure illustrates. This curvature arises due to various factors, both inherent to the observing setup, and external to it, and include atmospheric refraction and distortions in the imaging system.

This curvature is normally taken out by acquiring a frame taken through a pinhole mask (for an example, see Fig 3.4), which exhibits the curvature inherent to the data. This pinhole frame is then used to trace the curvature in the science data frames themselves, with a view to rectifying (i.e. straightening) the spectra.

Spectroscopic observations are also required to be calibrated in wavelength. This is normally achieved by acquiring a separate spectrum of an emission-line source, such as an Argon arc lamp. Known wavelengths can then be used to calibrate the

[2]A dark frame is a frame which is not exposed to light and which has a time-integration identical to that of the individual science data frames.

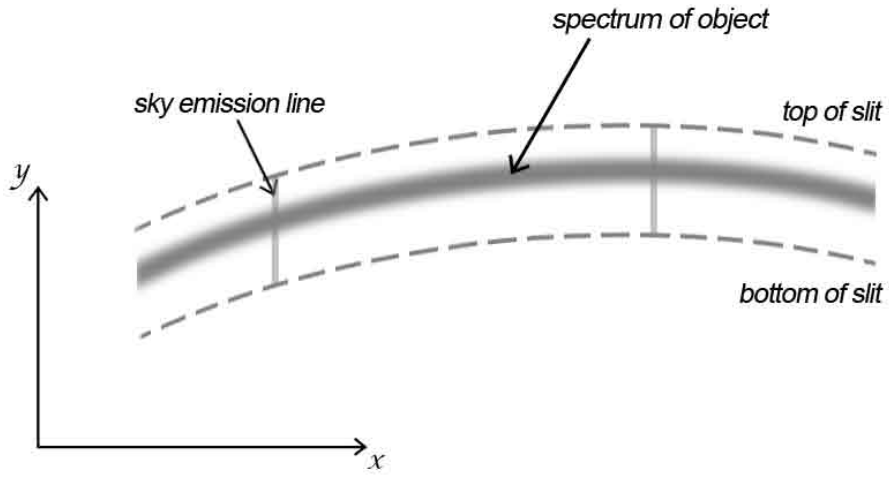

Figure 2.1: This figure adapted from Chromey (2010) illustrates how spectra often exhibit curvature which has to be rectified, usually by utilizing a pinhole frame which exhibits this same curvature to trace the spectrum from one end to the other.

science data in wavelength, normally by fitting some polynomial function to obtain the dispersion solution. Quite often, further optimisation can be achieved by comparing the sky emission lines visible in science data to a catalog of sky-lines.

Ground-based spectroscopic observations are often nodded, which is to say that an object is first observed occupying a certain location in the slit, then the telescope is shifted slightly such that the object can be observed in a different location on the slit. This is done to allow for the subtraction of background sky emission lines. The procedure is best understood by means of a schematic diagram, so the reader is referred to Figure 2.2 and its caption for a more complete description of what the process entails.

Ideally, after this sky-subtraction has been carried out, no sky emission lines would remain in the spectra. However, since sky-emission varies over time, especially in the Near-Infrared, it is likely that there will remain a residue which has to be taken out

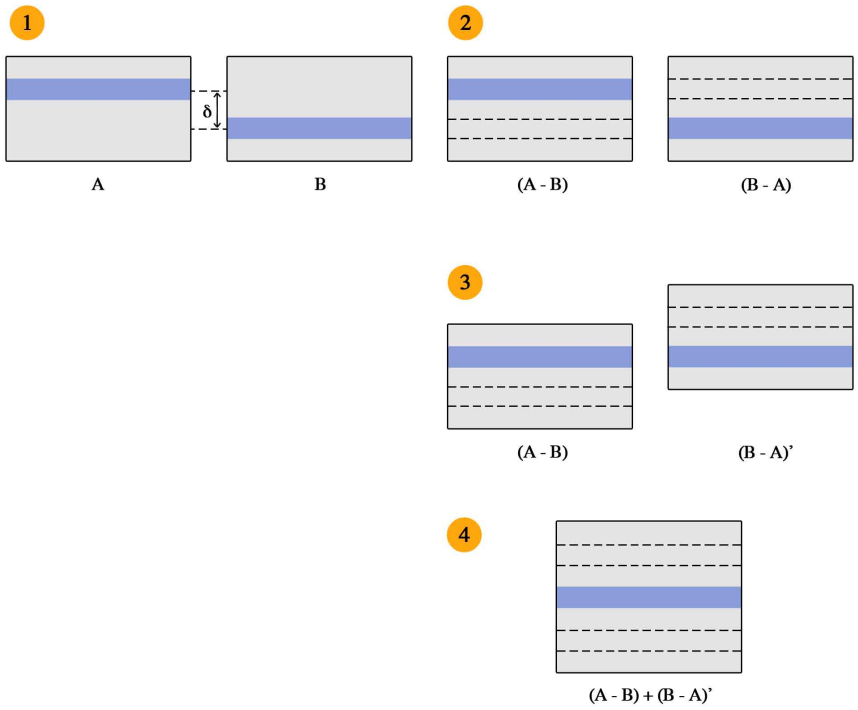

Figure 2.2: This schematic diagram illustrates the nodding procedure commonly used when obtaining spectroscopic observations. Step (1) shows how the telescope is nodded by a small amount such that the astronomical target occupies a different location on the slit in two successive frames. In step (2) the frames are subtracted from each other. The first frame in (2) called (A-B) contains a positive signal which has had the sky-subtracted using the sky lines from B; this sky-subtracted positive signal is represented by the shaded rectangle at the top. At the bottom we find a negative sky-subracted image of the object (dotted rectangle). The second frame in (2) called (B-A) represents the same thing but in reverse. These two frames are then shifted with respect to each other (Step 3) and combined (Step 4).

later, typically by means of fitting a polynomial in the direction of the sky lines (i.e. at each wavelength).

1-dimensional spectra then need to be extracted from the 2-dimensional version. Quite often, a tiny amount of curvature often remains in the spectra, even after the rectification process described previously, so normally, at every x-coordinate, the y-coordinate of the centroid of the spectrum is traced and then the pixel values are averaged over a certain width.

2.2.2 Flux calibration

So far, the spectrum of an astronomical target will still have units of instrumental counts, and the measured counts of the signal depend on various factors, namely the particular instrument system that is in use, the observing conditions at the time, as well as the source's own spectral shape. Ultimately, the signal needs to be expressed in a physical flux unit system, and the method most commonly used to achieve this flux calibration is to obtain spectra of photometric standard stars which have known flux density; these can then serve as calibrators. Atmospheric attenuation becomes very important at optical and near-Infrared wavelengths. The sources of extinction are multiple; the reader is referred to Hayes and Latham (1975) for a detailed treatment. In the near-Infrared, water vapour and Carbon Dioxide (CO_2) are significant absorbers in the Earth's atmosphere. However, whilst CO_2 can be found at a range of altitudes, water vapour is mostly prevalent close to the surface and has a strong dependancy on observatory location. Aerosols, such as dust and anthropogenic pollutants, are another major source of scattering. UV observations are hindered by Ozone (O_3) which absorbs radiation at wavelengths below 0.3μm. And finally, photons which interact with molecules in the atmosphere lead to Rayleigh scattering. Rayleigh scattering has a direct dependence on atmospheric pressure, so higher altitudes exhibit clearer skies. So before anything else, one firstly has to account for atmospheric extinction. Afterwards, the flux measured by the detector is converted to a system whose counts represent the absolute flux of the astronomical target that would be measured outside Earth's atmosphere. This is a standard procedure (e.g. see Modigliani, 2012); the description below follows the notation of Chromey (2010). Inside the Earth's atmosphere, the measure we get of the photon count per unit time for some pixel is given by:

$$I(\lambda) = \Phi(\lambda) \times A \times \Delta\lambda \times Q(\lambda) \times T(\lambda) \times S(\lambda) \times t \tag{2.2}$$

where $\Phi(\lambda)$ denotes the photon flux arriving at Earth before penetrating its atmosphere, A is the telescope's aperture, $\Delta\lambda$ is the wavelength interval per pixel, Q is the quantum efficiency of the detector, T is the spectrograph's throughput, S is the fraction of the photons absorbed by the atmosphere and t is the integration time.

For the star, we have the same expression:

$$I_{\rm star}(\lambda) = \Phi_{\rm star}(\lambda) \times A \times \Delta\lambda \times Q(\lambda) \times T_{\rm star}(\lambda) \times S_{\rm star}(\lambda) \times t_{\rm star} \tag{2.3}$$

From the last equation we can then specify the sensitivity function $R(\lambda)$ as being:

$$R(\lambda) = A \times \Delta\lambda \times Q(\lambda) \times T_{star}(\lambda) = \frac{1}{S_{\rm star}(\lambda)} \left[\frac{I_{\rm star}(\lambda)}{t_{\rm star}\Phi_{\rm star}(\lambda)} \right] \tag{2.4}$$

Considering the terms in square brackets, $I_{\rm star}$ is measured by the astronomer, $t_{\rm star}$ is the chosen exposure time which is of course another known quantity, and Φ_{star} (the flux outside the atmosphere) is looked up in standard star tables. The remaining quantity, $S_{\rm star}(\lambda)$, which measures absorption by the atmosphere, can be found using:

$$S_{\rm star}(\lambda) = e^{-0.9208k(\lambda)\times{\rm airmass}} \tag{2.5}$$

where $k(\lambda)$ is the extinction coefficient for the observing site and the airmass is the optical path length through the Earth's atmosphere for the light coming from the source, which has a $1/\cos\theta$ dependence, where θ is the zenith angle (i.e. the angle subtended from the zenith to the source).

Once the astronomer has a good sensitivity function, the spectrum of an astronomical target can then be flux-calibrated using:

$$\Phi(\lambda) = e^{0.9208k(\lambda)\times{\rm airmass}} \frac{I(\lambda)}{t \times R(\lambda)} \tag{2.6}$$

2.2.3 Aperture Spectrophotometry

In the case of observations of very high-redshift targets, the objects in question are tiny, near-point sources. Measuring the brightness of such sources entails defining an aperture centered on the object which should include a significant amount of flux from the target. However, the larger the aperture, the larger the contribution from background light; additionally the noise within an aperture scales as Noise $\propto \sqrt{\text{Area of aperture}}$. Therefore, the appropriate size of an aperture which is to maximize the signal to noise ratio is in effect a compromise between the total flux captured by the aperture and the total noise within it; the chosen size depends on the size of the object being analysed. Apertures may be circular or rectangular; in either case, if some of the flux from a source is not enclosed within the aperture, then this will be lost (see Fig. 2.3); this flux loss has to be accounted for in subsequent analysis. Assuming one's target has a gaussian profile, one way of measuring the amount of flux not captured by an aperture is to create a fake source with the same profile and with a known number of counts. One then places an aperture on top of this fake source to obtain a measure of the fraction of lost counts.

2.3 Analysis of Spectral Features

In this section, we shall briefly look at what kind of measure is commonly employed to characterize the strength and profile of spectral features, but at this point we shall not be looking closely at the astrophysical interpretation of spectra; this, of course, varies depending on the kind of observations made, so the interpretation and analysis pertaining to our own sample of high-redshift galaxies will be discussed in following chapters.

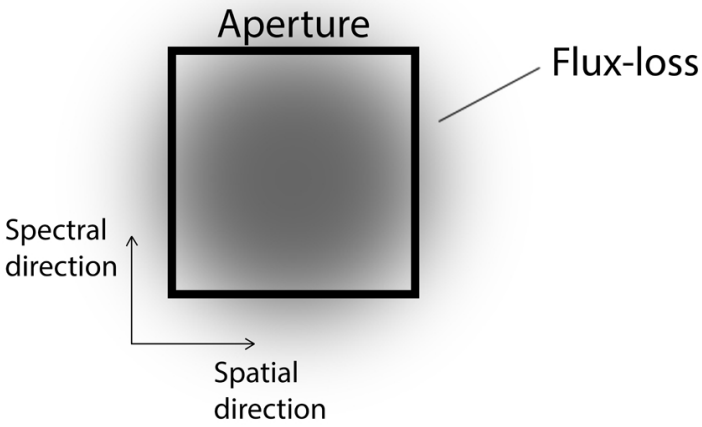

Figure 2.3: This schematic diagram shows a square aperture centered on a source. Some of the flux ends up being lost, and this flux-loss has to be measured and accounted for in subsequent analysis.

2.3.1 The Strength of the Spectral Line

Let us denote by $F_{norm}(\lambda)$ the flux as a function of wavelength, normalized by the continuum. This is referred to as the spectral feature's line profile, and its width is determined by various broadening mechanisms which affect the line's shape. The strength of such a line is measured by the Equivalent Width (EW), which is defined as follows (see, e.g., Vollmann and Eversberg, 2006; Chromey, 2010):

$$EW = \int_{\text{line}} (1 - F_{norm}(\lambda))d\lambda = \sum \frac{F_C - F_\lambda}{F_C} d\lambda \tag{2.7}$$

where F_C and F_λ are the continuum flux and line flux respectively.

Referring to Fig 2.4, the Equivalent Width can therefore be understood as the area contained in a rectangle whose height from a zero reference point is normalised to a value of 1, and which is equivalent to the area enclosed by the spectral line profile. So although it has wavelength units, the Equivalent Width actually gives a measure of the strength of the line.

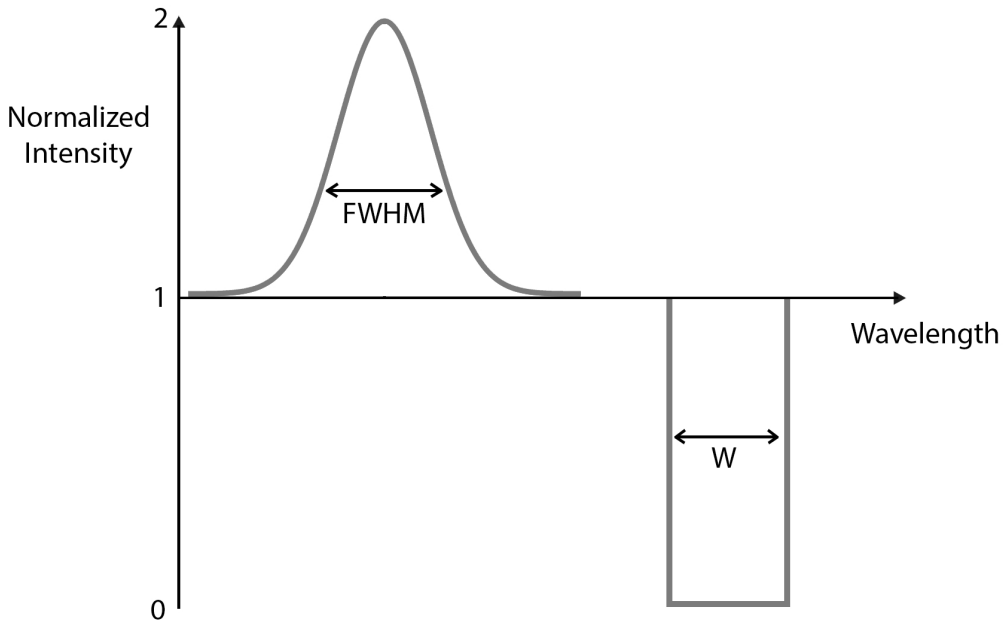

Figure 2.4: This schematic diagram shows how the Equivalent Width gives a measure of the strength of a spectral feature.

2.3.2 The Line Profile

Broadening Mechanisms

A spectral feature is never infinitesimally narrow in wavelength, but is broadened over some wavelength range. The precise shape of a spectral feature associated with some astronomical object is affected by various factors, both astrophysical and instrumental. Since the astrophysical factors are the ones which the astronomer is ultimately interested in, those other factors affecting the shape of a spectral line need to be understood and corrected for. The most relevant cases for our observations are those of Natural broadening and Instrumental broadening. Natural broadening occurs due to the uncertainty principle; since the lifetime of the excited state is related to the uncertainty in its energy, the result is what is called a Lorentzian profile. This kind of broadening is usually too small in spectra of astronomical objects (see, e.g., LeBlanc,

2010), but it contributes in the case of Lyman-α in the interstellar medium.

Another type of broadening is instrumental broadening. A spectrograph has a limitation on its spectral resolving power R ($= \lambda/\Delta\lambda$), and so, if one were to observe an infinitesimally small line, the profile is still observed to be broadened since the spectrograph's own profile is convolved with that of the observed line. So in order to derive the actual width of a spectral line one needs to deconvolve the observed line by the instrumental profile. Denoting the observed FWHM of a line by $\mathrm{FWHM}_{observed}$, the corrected, intrinsic FWHM of the line is given by:

$$\mathrm{FWHM}_{intrinsic} = \sqrt{\mathrm{FWHM}^2_{observed} - \mathrm{FWHM}^2_{instrument}} \tag{2.8}$$

Dynamical broadening can also be a major source of broadening. This type of broadening comes about when an object is rotating, resulting in an observed Doppler shift between two extremities (i.e. as the object rotates on itself, one side of the object appears to be receding from the astronomer whilst the opposite side appears to be approaching). In the case of the Lyman-α line, the main broadening is due to resonant scattering.

The Lyman-α line

The Lyman-α line at high redshifts is known to exhibit a strongly asymmetric profile since radiation shortward of 1216Å is absorbed by intervening neutral hydrogen gas. This leads to a sharp cutoff in the blue-wing of Lyman-α, resulting in a profile like that shown in Fig. 2.5, which is reproduced from Vanzella et al. (2011). This asymmetry is in fact the best diagnostic that an observed emission line in a candidate high-redshift object is indeed Lyman-α emission.

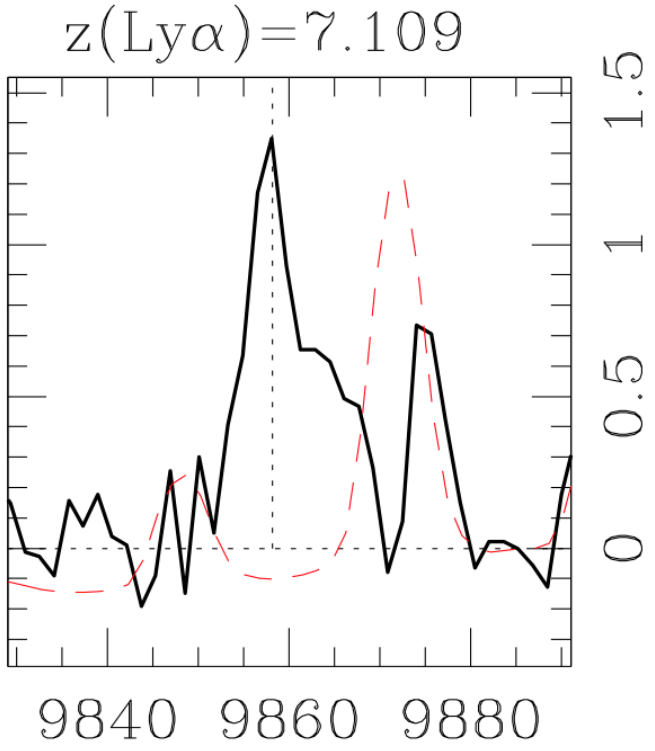

Figure 2.5: This figure shows the characteristic asymmetry exhibited by the Lyman-α line at high redshift, caused by intervening neutral hydrogen absorbing radiation shortward of 1216Å. This figure reproduced from Vanzella et al. (2011) shows BDF-3299, whose Lyman-α emission places it at $z = 7.109$. The dashed line represents the sky spectrum. Units on the x-axis are in Angstroms.

2.4 Determining the S/N of Spectral Features

As we have discussed previously, in observations of high-redshift objects any potential Lyman-α emission will be much fainter than the brightness of the background sky; this often necessitates a statistical approach to determining the reality of any potential spectral features, which involves assessing the signal to noise ratio of any candidate emission line, which is expected to be fairly low.

Once the data have been completely reduced, one needs to characterize the noise and ensure that its behaviour is well understood. Making the initial assumption that the noise is obeying Poisson statistics, various tests can be carried out to ensure that this is truly the case, such as checking that the noise in the combination of several frames (normalised to unit time) scales down as $\sqrt{\text{time}}$, and in general ensuring that the actual, measured noise in the 2D frames is close to what would be expected from a Poisson model characterized by the sky background, dark current, readout noise, etc. Following Poisson statistics, the noise properties for an extracted 1D spectrum are expected be governed by a relation similar to this one:

$$\begin{aligned}\text{Predicted Noise (in cgs units)} \quad &= \\ \text{Cal. Flux} \times \sqrt{W_{spec} \times W_{spat}} \quad &\times \quad \frac{\sqrt{(\{\text{Sky+Data}\} \times t \times N \times g) + N \times (\text{R.N.} \times g)^2}}{(t \times N \times g)}\end{aligned}$$

where Cal. Flux is the wavelength-dependent flux-calibration, W_{spec} and W_{spat} are the spectral and spatial widths of the aperture respectively, {Sky+Data} is the reduced (but not flux-calibrated) data with the sky added to it, t is the exposure time per frame, N is the total number of frames, and g and R.N. are respectively the gain and read-noise of the detector.

Once the astronomer has determined that the noise is well understood, the process of identifying possible Lyman-α features in a 2D spectrum becomes easier. The

process entails dividing the 2D spectrum by a Poisson noise map (which map gives the noise per pixel). If the noise model is indeed correct, then the resulting 2D-frame should be a noise-normalized 2D spectrum, and a measure of the statistical standard deviation in any location on the 2D frame should return a value of 1. Such a measure can easily be attained using standard reduction software packages. (NOAO's `IRAF`, for instance, has an inbuilt task called `imexam` which was used for this purpose in the work for this thesis.) If one wanted to search for any features having a Signal to Noise ratio, $\sigma = X$, then the number of counts corresponding to this is given by:

$$\text{Counts (at } \sigma = X) = \frac{\sqrt{\text{Area of Aperture}}}{\text{Aperture Correction}} \times X \tag{2.9}$$

One can then perform an automated search which scans the spectrum for any features with counts higher than this amount, and even perform a visual inspection of the spectrum, thresholding it such that only features having counts larger than this number are displayed. (Quite often in our work, the frame to be visually inspected was a version of the 2D spectrum to which a boxcar filter has been applied.) This facilitates the process of searching for and identifying any interesting features in the data.

Chapter 3

Observations with Gemini/GNIRS and VLT/XSHOOTER

3.1 Spectroscopic Searches for Lyman-α emission

As was described in Chapter 1, the main aim of this work was to investigate the emergence of Lyman-α emission from high redshift candidate galaxies, with a view to confirm the redshift of these objects, establish the fraction of Lyman-α emitters, and from this attempt to infer the fraction of neutral Hydrogen. The first observations employed for this project were acquired by Andrew Bunker in 2004 and 2005 using the Gemini Near Infrared Spectrograph (GNIRS) at the Gemini South telescope in Chile. The raw data from this observing project were made available for reduction and analysis, and the observations of four z-band dropouts targeted by Gemini/GNIRS are the subject of the first sections of this chapter. Afterwards, observations of 1 z-band dropout and 2 Y-band dropouts carried out much later in 2010 and 2011 using the X-Shooter Spectrograph on the Very Large Telescope (VLT) are discussed. In particular, X-Shooter was used to investigate the claim by Lehnert et al. (2010) that Lyman-α emission was observed in the Y-band dropout HUDF.YD3 (Bunker

et al., 2010; Lorenzoni et al., 2011). The results from observations of this object are presented in the last part of this chapter.

3.2 Observations with Gemini/GNIRS

The four z-band drop-out high-redshift galaxy candidates HUDF.zD1, HUDF.zD2, HUDF.zD3 and HUDF.zD4 (Bunker et al., 2010), hereafter called zD1, zD2, zD3 and zD4, were observed by Andrew Bunker. These objects had initially been selected as candidate $z > 7$ sources with HST/NICMOS imaging as they were undetected in the ACS images of the HUDF (Bunker et al., 2004) and re-confirmed with HST/WFC3 (Bunker et al., 2010, Oesch et al., 2010b). To acquire these observations, Andrew Bunker used the GNIRS spectrograph on the Gemini South telescope as part of programmes GS-2004B-Q-19 and GS-2005B-Q-18 (PI: A. Bunker, see also Stanway et al., 2004). GNIRS is a spectrometer that can perform both long-slit, single-order spectroscopy in the $1.0 - 5.4\mu$m range and cross-dispersed (i.e. multi-order) spectroscopy in the $0.9 - 2.5\mu$m range. The latter cross-dispersed mode was used with the "high-dispersion" 110.5 l/mm grating and short blue camera, with a 7"-long slit. In this mode, one does not get continuous spectral coverage, since not all of the spectral orders fall on the array.

Three of the objects (zD2, zD3 and zD4) were observed using a grating angle of 21 degrees and the XD_G0525 filter, which allowed the observations to include the regions 0.86-0.94μm and 1.005-1.095μm in the range of covered wavelengths, corresponding to redshifts $z \sim 7$ for Lyman-alpha, as expected for z-band dropouts). The observations of zD1 were carried out using two observing settings. For one setting, the same grating angle of 21 degrees was used, but with the XD_G0507 filter instead, whereas for the second setting the grating angle was changed to 23.2 degrees and the XD_G0525 filter was used. This setting enabled the inclusion of the wavelength range between

0.94μm and 1.005μm, as well as the region 0.83μm-0.90μm, thus providing continuous spectroscopy between 0.83μm and 1.095μm ($z = 5.8 - 8.0$ for Lyman-alpha).

The coordinates for these four objects are taken from from Bunker et al. (2010). In acquiring the object, a nearby star (with accurately determined astrometry from HST) was first centered in the slit and then a blind offset (less than 1′) was executed to place the faint z-dropout galaxy in the slit. The Gemini telescope can execute an offset of this size to an accuracy of better than 0.″2[1] when the same guide star is used throughout (as was the case for these observations). A slit width of 0.″675 was used for all observations and the data were acquired in a three-point dither pattern (ABC) at positions +1.″8, 0, -1.″8 along the slit long axis. When calculating the slit losses, a test was carried out to check the effect of offset errors. This was achieved by measuring the flux from fake sources with an aperture which had a positional shift applied to it (corresponding to a given offset error), with the conclusion being that offset errors would have at most a 10 per cent effect on the flux captured by the aperture. Each frame was a 900s exposure. In total, 9 frames were combined for each setting of zD1, and also for zD3 and zD4, whilst 7 frames were combined for zD2. The observations were conducted between 2004 and 2006 (see table 3.1). The seeing measured from the point spread function (PSF) of a star in the acquisition spectrum was about 0.″5 Full Width at Half Maximum (FWHM). The seeing was monitored by the observers in real time via the Peripheral Wavefront Sensor star, and if the seeing degraded then the queue-mode observations of this programme were terminated and observations switched to a programme with a less stringent seeing requirement. In some instances during the observation of our target for extended periods, a reacquisition of the blind offset star was performed. The blind offset star was confirmed to appear in the expected position (i.e. the telescope pointing had not wandered off), and the seeing was again ensured to be consistent (about 0.″5 on

[1]See `http://www.gemini.edu/sciops/telescopes-and-sites/acquisition-hardware-and-techniques?%20q=node/10769`

Object	R.A. (J2000)	Dec (J2000)	$Y_{\rm AB}$-mag	$J_{\rm AB}$-mag	M_{1600}	Exp Time (hrs)	Date
zD1	03:32:42.56	-27:46:56.6	26.71 ± 0.03	26.44 ± 0.03	-20.53	2.25 2.25	27 Nov 2004 20 Dec 2005
zD2	03:32:38.81	-27:47:07.2	27.48 ± 0.06	26.90 ± 0.04	-20.18	1.75	08 Dec 2005
zD3	03:32:42.57	-27:47:31.5	27.50 ± 0.07	27.10 ± 0.05	-19.64	2.25	17 Dec 2005
zD4	03:32:39.55	-27:47:17.5	27.84 ± 0.09	27.34 ± 0.05	-19.79	2.25 2.25	18 Dec 2005 30 Jan 2006

Table 3.1: z-band dropouts targetted with Gemini/GNIRS. The RA & Dec positions are from Bunker et al. (2010). The Y- and J-band magnitudes quoted for zD1, zD2 and zD3 are from Wilkins et al. (2010) using the WFC3 Y_{098m}/Y_{105w} and J_{125W} filters respectively whereas the Y- and J-band magnitudes quoted for zD4 are from Bunker et al. (2010). M_{1600} is the absolute rest-frame UV magnitude around 1600Å for the most probable redshift.

Object	R.A.	Dec
zD1	03:32:42.56	-27:46:56.58
zD2	03:32:38.79	-27:47:07.14
zD3	03:32:42.57	-27:47:31.42
zD4	03:32:39.54	-27:47:17.41

Table 3.2: The original pointing coordinates used for the Gemini/GNIRS observations, which are stored in the file headers.

average). Hence once can be confident about the seeing used to estimate the slit losses. Flux calibration was carried out using observations of a spectrophotometric A0V telluric standard star which was observed on the same dates as the objects. The spectral resolving power was measured from unblended spectral lines in the sky spectra, and this delivered $R = \lambda/\Delta\lambda_{\rm FWHM} = 3700$.

3.3 Reduction of Gemini/GNIRS data

The GNIRS spectra were reduced with `IRAF` using a customized reduction pipeline, which is partly based on an existing Gemini pipeline. The `IRAF` GNIRS task `nvnoise` was first used on the raw data frames (see Fig. 3.1) to remove a vertical striping pattern (see Fig. 3.2) that arises from offset bias levels. Then `nsprepare` was used to create variance and data quality planes for the frames (see Fig. 3.3).

These frames were combined using the `IRAF` task `imcombine` and `ccdclip` was used

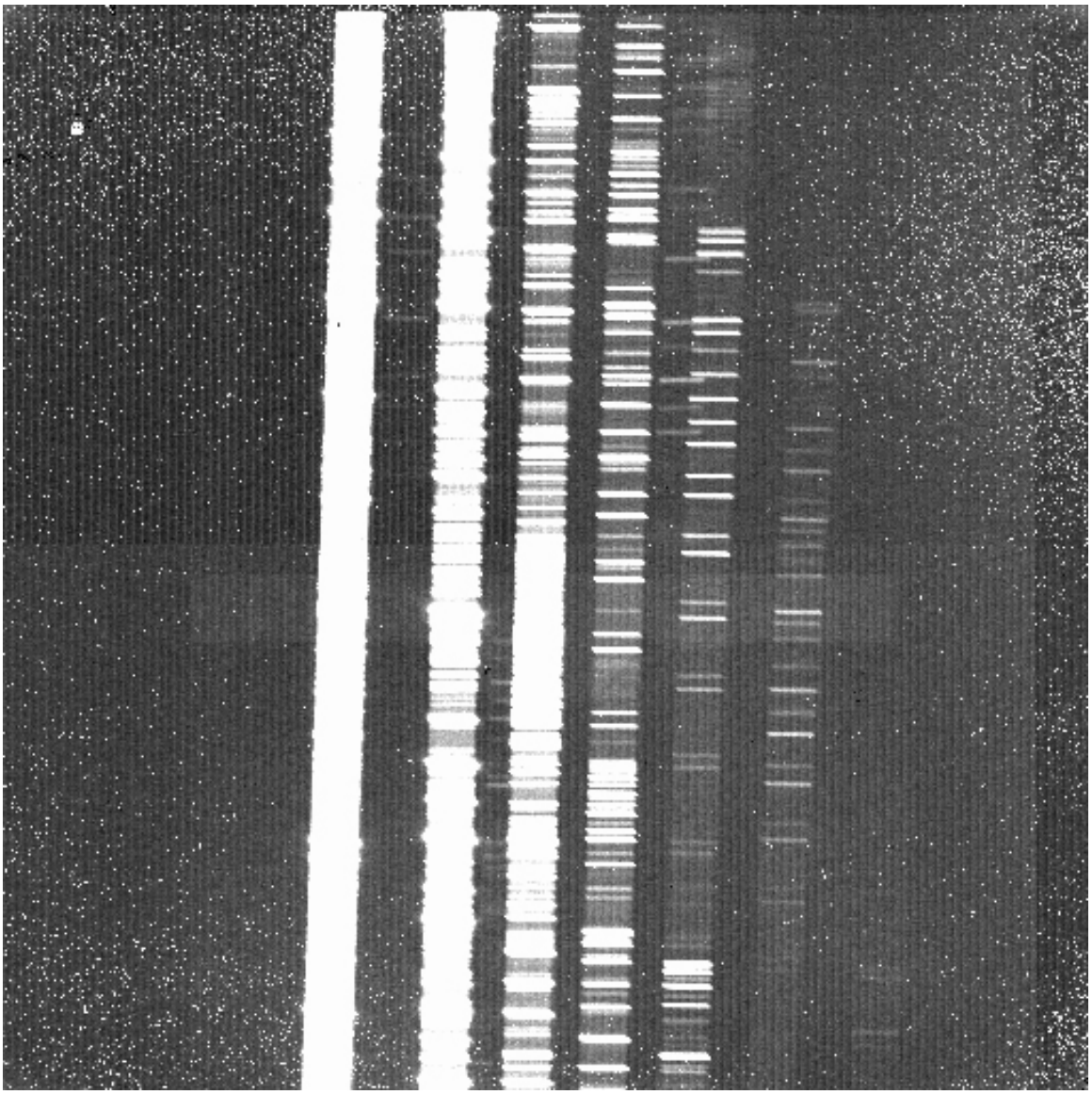

Figure 3.1: An example Gemini GNIRS raw frame from the dataset, exhibiting multi-order data. Numerous problems which need to be addressed prior to analysis are apparent even at first glance. These issues include a vertical striping pattern, many cosmic ray hits, numerous hot pixels, many sky emission lines and a slanting orientation (from the vertical).

to reject remaining cosmic rays (after offsetting, masking and thresholding) given the parameters of the detector. In essence, the noise characteristics of the data are defined if the readout noise and gain parameters for the CCD are known, and the data has been processed in such a way as to preserve the relation between photons/electrons

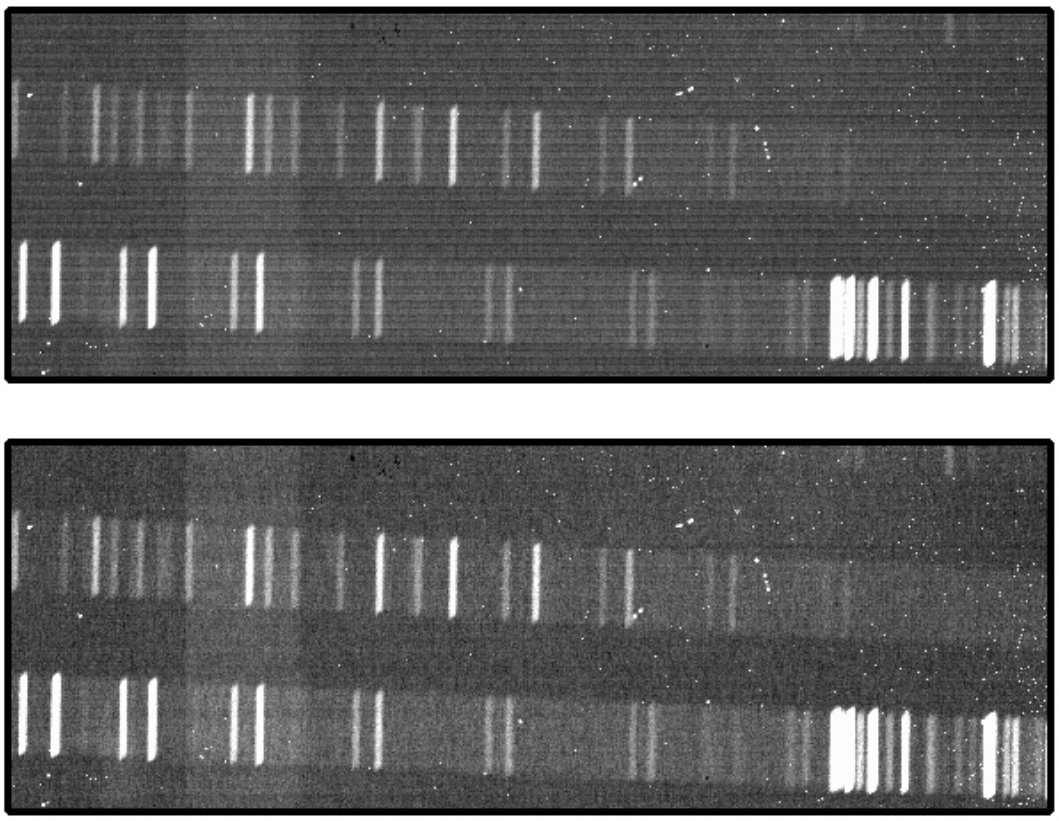

Figure 3.2: The top panel shows a section from a raw GNIRS frame (here showing parts of orders 5 and 6) which exhibits a striping pattern arising from offset bias levels. (Note that in this figure, the striping pattern is oriented horizontally instead of vertically because the original frame has been rotated by 90 degrees.) The bottom panel shows the same region of the frame after having used the `IRAF` task `nvnoise` to remove the striping pattern.

and data values. In the model used by `ccdclip`, the sigma in the data values at a pixel with true value $\langle P \rangle$ is given by:

$$\sigma = \left[\left(\frac{R.N.}{g} \right)^2 + \frac{\langle P \rangle}{g} + (s \times \langle P \rangle)^2 \right]^{1/2} \tag{3.1}$$

where $R.N.$ is the readout noise in electrons, g is the gain in electrons per data value, and s is the sensitivity noise[2] given as a fraction. The algorithm of `ccdclip`

[2]For objects exhibiting high Signal to Noise, the uncertainty in the flat field dominates over the

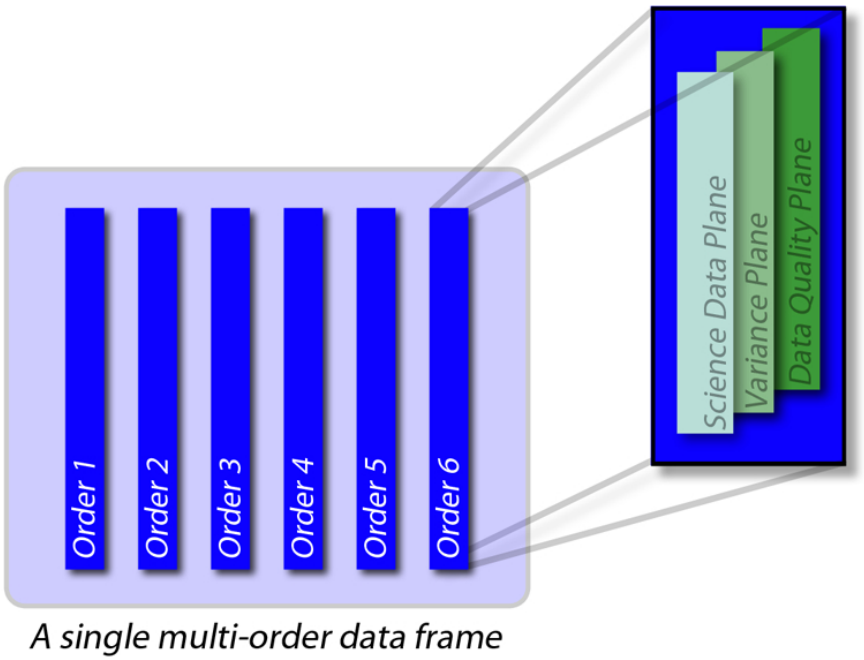

Figure 3.3: This schematic diagram illustrates the structure of GNIRS cross-dispersed data. Each frame consists of multiple orders, each of which is made up of a science data plane, a variance plane and a data quality plane.

treats each output pixel independently. In our case, it takes the average (as opposed to the median) of the unrejected pixels, computes the expected σ using the above equation and then rejects those pixels which are $hsigma \times \sigma$ above this average or $lsigma \times \sigma$ below this average, where $hsigma$ and $lsigma$ are the selected clipping threshold parameters set by the user in `ccdclip`. The number of retained pixels after rejection is checked against a user-set parameter $nkeep$ which limits the number of pixels rejected; if the number of pixels retained is fewer than what is specified by the value of this parameter, then the pixels with the smallest residuals in absolute value

Poisson noise of the object. This means that when one combines individual frames assuming a Poisson model, there is a risk that for very bright objects, the photometry will vary from position to position by a few sigma. The parameter 'sensitivity noise' offers a way around this problem so that one does not over-reject bright sources. It should be noted, however, that the sources targeted in this study are so faint that this term does not really matter in this case.

are added back. Also, if there is more than one pixel with the same absolute residual, these are added back in.

The resulting rejection frames were used to mask those pixels affected by cosmic ray strikes and then the same task was carried out a second time to apply a further pass of cosmic ray rejection, also using the data quality array to mask bad pixels. Flat-field generation was achieved by using the tasks `nsreduce` and `nsflat` on three sets of flats - each appropriate for different orders: the first set being IR lamp flats, the second set being short-exposure Quartz Halogen (QH) lamp flats and the third set being long-exposure QH lamp flats. `nsflat` produces a normalized flat-field image and a bad pixel mask.

Subsections of the data corresponding to each spectral order were then trimmed out from the original 2D spectrum (by means of the `IRAF` task `nscut` called from within `nsreduce`) and these were sky-subtracted to first order by subtracting the average of the other dither positions and flat-fielded using `nsreduce`. The spectra were rectified (spatially and spectrally) using two-dimensional arc-spectra through a pinhole file, correcting for geometric distortion of the optics in the detector, and any remaining skyline residuals were removed using the `background` task. `background` fits a function to a set of columns (i.e. constant wavelengths along slit length) specified by the user. This function is then subtracted from the entire line. (See Fig. 3.5 for an example.) A model of the skylines was then added (see Fig. 3.6) to every frame prior to combining them with `imcombine` to enable the rejection of any remaining cosmic ray strikes using a Poisson noise model. Finally, the sky model was subtracted from the resulting frame. Flux calibration was obtained using the above-mentioned telluric standard star by means of standard `IRAF` techniques. The star was extracted using the `apall` task. `standard` was used to integrate the observations of the standard stars over calibration bandpasses. `standard` was supplied with a blackbody flux distribution model together with the magnitude and spectral type of the star to

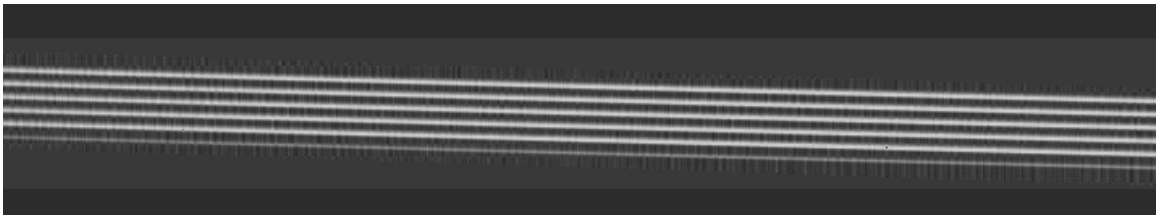

Figure 3.4: This figure shows a section from an example GNIRS pinhole frame which was used to rectify the spectra.

obtain a calibration flux after interpolating over the Balmer absorption lines in the A0 stars. `standard` computes the $m_{\rm AB}$ of the star using:

$$m_{\rm AB} = {\rm mag} + m_{\rm AB}(m = 0) - 2.5 \times log_{10} \frac{B(w_{\rm eff}, t_{\rm eff})}{B(w, t_{\rm eff})} \tag{3.2}$$

where m is the magnitude of the star in the calibration band, $m_{\rm AB}(m = 0)$ is the calibration value in the calibration file representing the magnitude of a $m = 0$ star (which is effectively the m_{AB} of Vega), $w_{\rm eff}$ is the effective wavelength for the calibration file, and $t_{\rm eff}$ is the effective temperature of the star. The function $B(w, T)$ is the blackbody function in f_ν that gives the shape of the calibration.

The task `sensfunc` (which was fed the output of `standard`) was then used to determine the system sensitivity and to apply an extinction correction. Finally the `calibrate` task was used to calibrate the data.

3.4 Observations with VLT/XSHOOTER

Observations were made of the two Y-band dropouts HUDF.YD3[3] (Bunker et al., 2010; Lorenzoni et al., 2011) and ERS.YD2 (Lorenzoni et al., 2011) and the z-band dropout P34.z.4809[4] Wilkins et al. (2011) using the XSHOOTER spectrograph (D'Odorico et al., 2006) on the ESO VLT-UT2 (Kueyen) as part of programme 086.A-

[3]UDFy-38135539 in Bouwens et al. 2010, 1721y in McLure et al. 2010, z8-B115 in Yan et al. 2010, 125 in Finkelstein et al. 2010

[4]This corresponds to the Y-drop UDF092y-03781204 in Bouwens et al. 2011

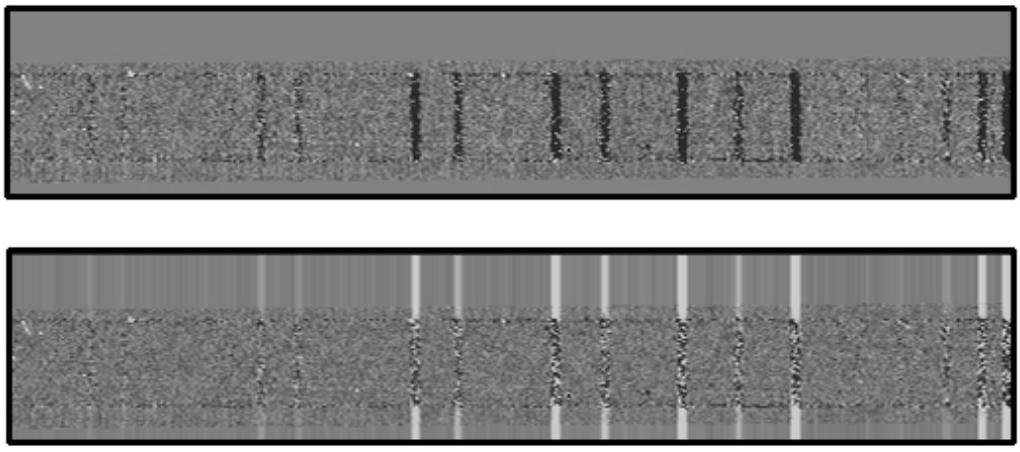

Figure 3.5: The top panel shows a section from an example GNIRS spectrum before sky subtraction, whilst the bottom panel shows the same section after sky subtraction using the `background` task.

Figure 3.6: This figure shows a model of the sky which was obtained by first running the `IRAF` task `background` on the data and then subtracting the result from the data.

0968(B) (PI: A. Bunker). XSHOOTER is an echelle spectrograph, with UV, visible and near-infrared channels obtaining near-continuous spectroscopy from 0.3μm to 2.48μm with a 1.″2-wide and 11″-long slit. HUDF.YD3 will be discussed in detail in a separate section, so here the attention will be focused on spectroscopy of the other two targets. The observations were dithered in an ABBA sequence. For HUDF.YD3 and ERS.YD2, the observations were dithered at positions +3″ and −3″ from the central coordinates along the slit long axis (i.e. a 'chop' size of 6″). In the case of P34.z.4809 the observations were dithered +2.″5 and −2.″5 from the central coordinates along the slit long axis (i.e. a 'chop' size of 5″).

For ERS.YD2 the central coordinates were set to be RA=03:32:02.986 Dec.=-27:43:51.95 (J2000) with coordinates from Lorenzoni et al. (2011). The telescope was first peaked up on a nearby star 68.″51 East and 25.″7 South of the desired central pointing, then did a blind offset. For P34.z.4809 the central coordinates were set to be RA=03:33:03.765 Dec.=-27:51:20.11 (J2000) so that both the position of P34.z.4809 in Wilkins et al. (2011) - see Table3.3, and UDF092y-03751196d from Bouwens et al. (2010) which is 0.″8 away, could be targeted. The P.A. was set to -22.5^o to intercept both objects. The telescope was first peaked up on a nearby star 17.″98 East and 10″ South of the desired central pointing, and then a blind offset was again carried out. For blind offsets of this size, ESO guarantee an accuracy better than 0.″1 where the guide star remains the same. The effect of this positional uncertainty on the fraction of the light falling down the slit was measured as described previously, with the conclusion that this was at most a 5-10 per cent effect.

The ERS.YD2 observations were conducted in 6 observing blocks, each including 49 mins of on-source integration and consisting of a single ABBA sequence with three exposures of the near-IR arm of duration 245 s at each A or B position. The observations were taken on the nights of UT 2010 December 07 and 2011 January 02, 04, 05, 11 & 23. The vast majority of the frames were taken in good seeing

Object	R.A. (J2000)	Dec (J2000)	Mag (J)	M_{1600}	Exp Time (hrs)	Date
HUDF.YD3	03:32:38.135	-27:45:54.03	28.18 ± 0.13	-19.12	0.82	27 Dec 2010
					1.63	29 Dec 2010
					1.63	30 Dec 2010
					0.82	31 Dec 2010
ERS.YD2	03:32:02.986	-27:43:51.95	26.98 ± 0.15	-20.28	0.82	07 Dec 2010
					0.82	02 Jan 2011
					0.82	04 Jan 2011
					0.82	05 Jan 2011
					0.82	11 Jan 2011
					0.82	23 Jan 2011
UDF092y-03751196d	03:33:03.750	-27:51:20.40	26.30 ± 0.00	-20.92	0.82	16 Oct 2010
					1.63	17 Oct 2010
					0.82	19 Oct 2010
					0.82	28 Oct 2010
P34.z.4809	03:33:03.781	-27:51:20.48	26.39 ± 0.03	-20.65	0.82	16 Oct 2010
					1.63	17 Oct 2010
					0.82	19 Oct 2010
					0.82	28 Oct 2010

Table 3.3: The 3 Y-band dropouts and 1 z-band dropout targeted with VLT/XSHOOTER. The RA & Dec positions are from Lorenzoni et al. (2011) for HUDF.YD3 and ERS.YD2, from Wilkins et al. (2011) for P34.z.4809 and from Bouwens et al. (2011) for UDF092y-03751196d. The J-band magnitudes for each object are quoted from the same respective papers using the WFC3 $F125W$ filter. M_{1600} is the absolute rest-frame UV magnitude around 1600Å for the most probable redshift.

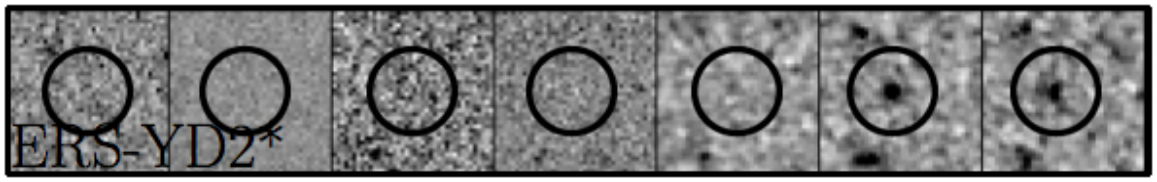

Figure 3.7: This figure shows HST/WFC3 imaging through different filters of ERS.YD2, which drops in the Y-band filter.

conditions of $0\farcs56 - 0\farcs76$ FWHM. The P34.z.4809 observations were conducted in 5 observing blocks, for each 49mins of which consisted of on-source integration. These were taken on the nights of UT 2010 October 16, 17, 19 & 28 with two observing blocks taken on the night of UT 2010 October 17 and single observing blocks on the other nights. Seeing conditions were similar to those during the observations of ERS.YD2. All observations were taken at low airmass, with an average airmass of 1.16, and 83 per cent of the observations were taken at airmasses below 1.3. At such low airmass, the effect of differential atmospheric dispersion is negligible between the red end of the optical channel and the near-infrared 1-3μm (where we expect Lyman-α), and the alignment star was confirmed to be centred in the slit in both the optical and near-infrared spectra. Three piezo controlled mirrors, located in front of each arm, guarantee that the optical path is maintained aligned against instrument flexure and correct for differential atmospheric refraction between the telescope guiding wavelength and each arm central wavelength.

The resolving power attained for our IR-channel observations of ERS.YD2 was $R = \lambda/\Delta\lambda = 5000$. In the case of P34.z4809, data acquired with both the optical arm and the near-infrared arm was considered, since this object is a z-drop, so the expected redshift for Lyman-alpha range extends down to just below 1μm. These optical data were obtained on the same dates as the IR data and were acquired in 5 observing blocks, each including 49 minutes of on-source integration. The resolving power for the optical channel was $R = 6700$. There is a small region of overlap between

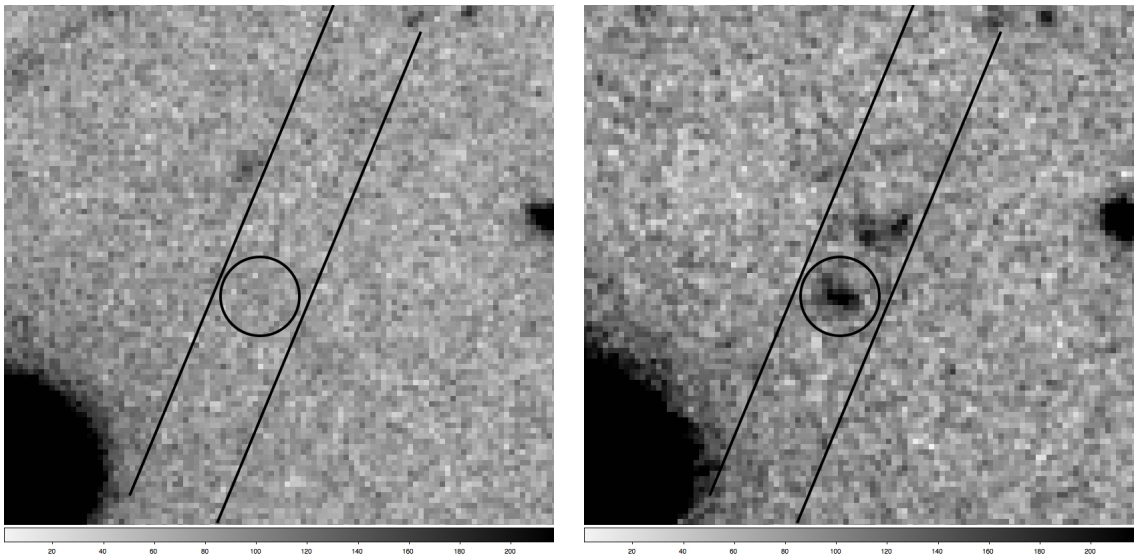

(a) z-band image

(b) Y-band image

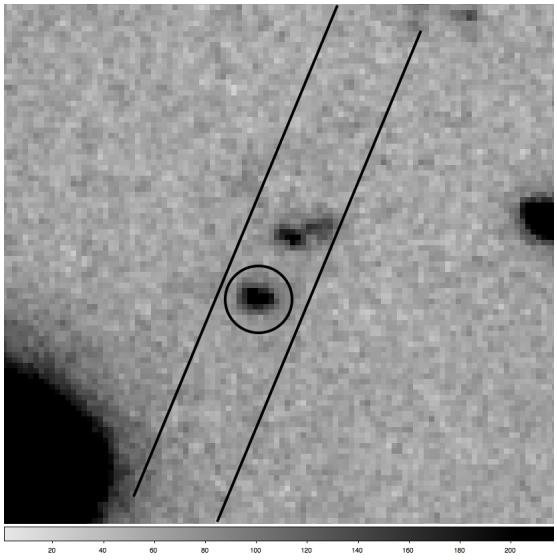

(c) J-band image

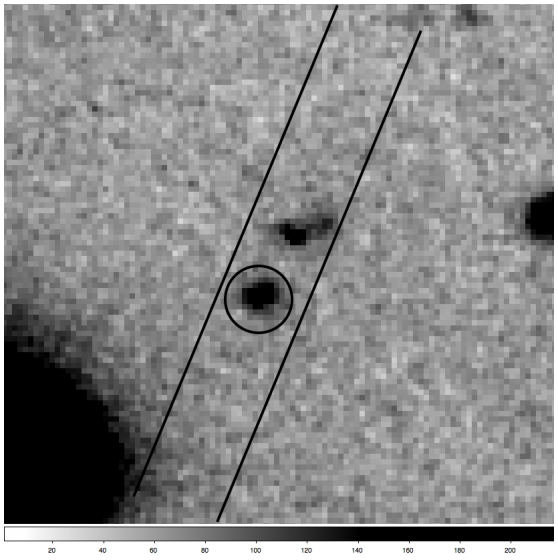

(d) H-band image

Figure 3.8: These figures show HST/WFC3 thumbnail images of P34.z.4809 (taken through different filters), with the X-Shooter slit used for the observations reproduced on each one of them. Figure (a) shows the z-band thumbnail image where the object drops out, (b) shows the Y-band thumbnail image, (c) shows the J-band thumbnail image and (d) shows the H-band thumbnail image. North is up and East is to the left in these thumbnails.

the two arms ($0.994-1.013\,\mu$m) and in this range the 2D spectra were combined using inverse-variance weighting as a function of wavelength, which accounted for the strong variation of throughputs/sensitivities with wavelength in the overlap region and also

the different readout noise characteristics of the two detectors.

3.5 Reduction of VLT/X-Shooter data

The ESO pipeline (Modigliani et al., 2010) was used to reduce our data. This pipeline applied spatial and spectral rectification to the spectra, which exhibited significant spatial curvature (see Fig. 3.9) as well as a non-linear wavelength scale, by using the two-dimensional arc spectra through a pinhole mask (see Fig. 3.10). For the IR channel, it mapped the data to an output spectral scale of $1\,\text{Å}\,\text{pix}^{-1}$ and a spatial scale of $0\farcs21$ (from original scales of about $0.5\,\text{Å}\,\text{pix}^{-1}$ and $0\farcs24$ respectively). For the z-drop P34.z.4809 one might expect that Lyman-α falls at the red end of the optical spectrum (around 0.9μm), hence the optical channel was also inspected for this object. In the optical channel data were mapped to an output spectral scale of $0.4\,\text{Å}\,\text{pix}^{-1}$ and a spatial scale of $0\farcs16$. In both channels, the data were flat-fielded and cosmic rays were identified and masked using the algorithm of van Dokkum (2001). The two dither positions were subtracted to remove the sky to first order, and the different echelle orders were combined together into a continuous spectrum (taking into account the different throughputs in different overlapping echelle orders) before spatially registering and combining the data taken at the two dither positions, and removing any residual sky background. Flux calibration was achieved through observations of standard stars LTT3218, GD-71 and Feige 110 taken on the same nights as the science data. A subset of the standard star observations that were taken in similar seeing conditions and at similar airmass to our science data was chosen.

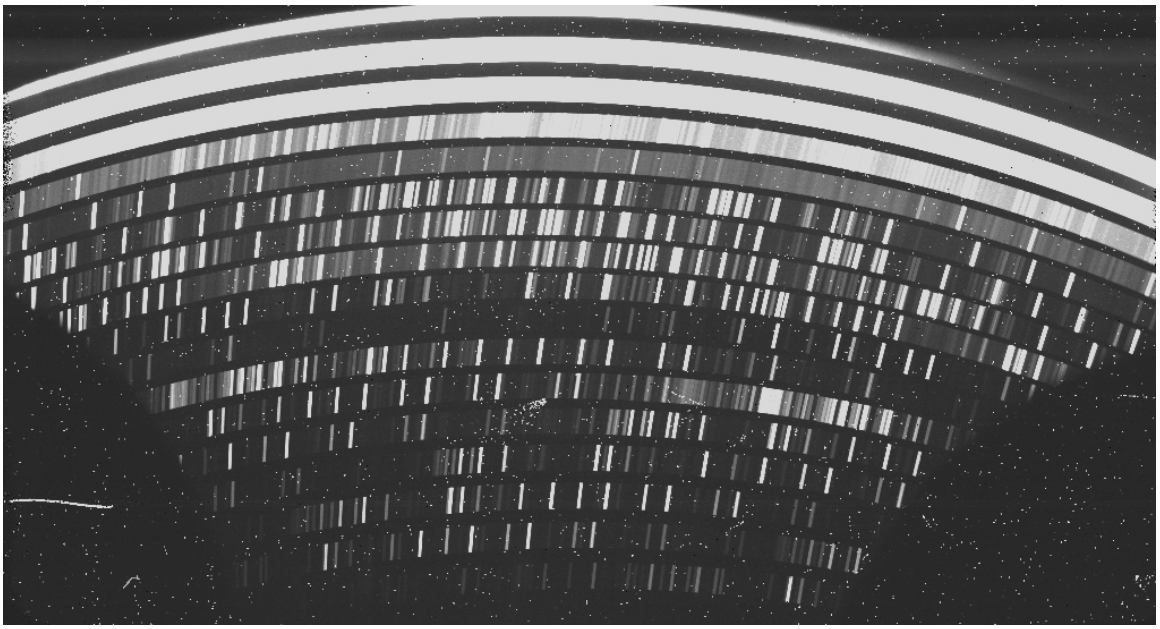

Figure 3.9: An example VLT X-Shooter IR raw frame from our dataset, exhibiting multi-order data. Numerous problems which had to be mitigated throughout the reduction process prior to analysis include numerous cosmic ray hits and several hot pixels, many sky emission lines and strong curvature.

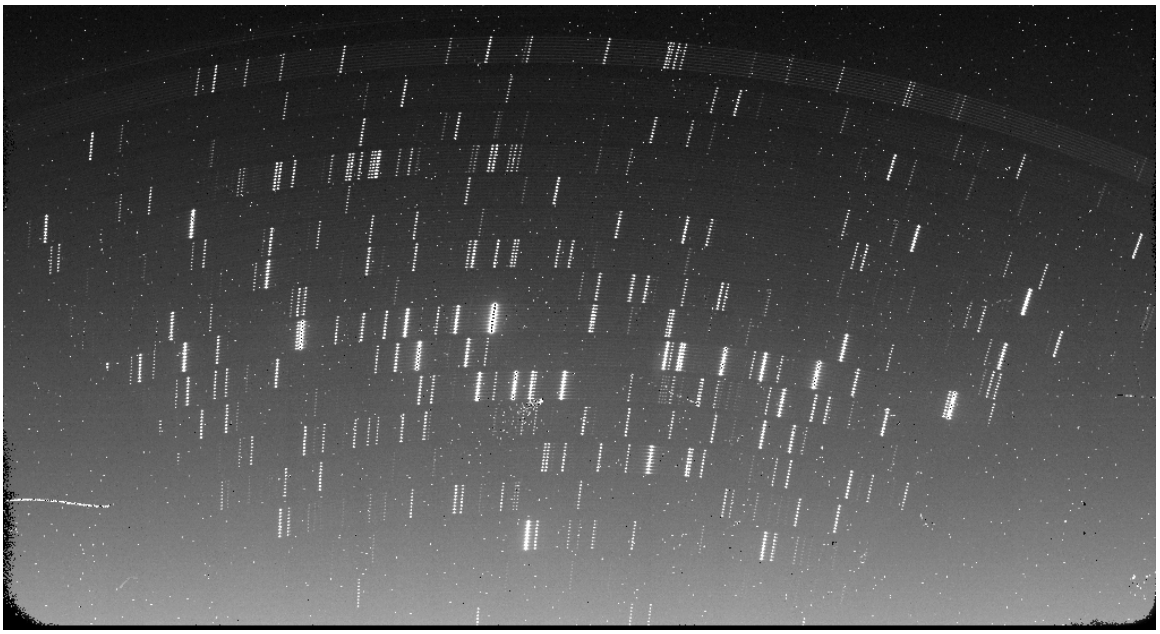

Figure 3.10: This figure shows a two-dimensional arc spectrum (for IR data) taken through a pinhole mask which was used to rectify the spectra spatially and spectrally.

3.6 RESULTS

All the 2D spectra were inspected, with attention being focused in particular on the expected location for the target and the wavelength ranges between 0.8 and 1.2 microns where Lyman-α might be expected. This was done through visual inspection, including examining frames which had been smoothed by means of convolution with a Gaussian with similar FWHM to the spatial seeing and spectral resolution to bring up any faint feature. A noise model was developed, based on the Poisson counts of the sky background and dark current, the sensitivity of the detector (as a function of wavelength and position on the array) and the readout noise of the array. Dividing the reduced 2D spectrum by the noise model provided a map of signal-to-noise ratio. SExtractor (Bertin and Arnouts, 1996) was run on the 2D spectrum after division by the noise model to identify possible emission lines which might have been missed through visual inspection. As a check on contamination by spurious sources and noise spikes, the negative image was also examined to confirm that there were no significant detections.

No significant line emission was detected in any of the objects in the sample. To test the recoverability of possible line emission in our spectroscopy, fake sources of various intensity were added in random locations in the 2D spectra and these were checked to ascertain if the sources would have been detected. Initally, an emission line with an elliptical Gaussian profile was used, adopting a FWHM of 200 $\mathrm{km\,s^{-1}}$ in the spectral direction, and compact spatially (to match the typical small sizes of the Lyman break population at $z > 6$). This was then convolved with another Gaussian to reflect the instrumental spectral resolution and the ground based seeing (i.e. FWHM of about $0\farcs5$ and 2.56 Å for the near-infrared spectroscopy, and 1.4 Å for the XSHOOTER optical arm). One should note that the effect of the strong Lyman-α forest absorption at these redshifts would be expected to absorb the entire blue wing of this line emission, so the actual line width and flux before absorption might be twice

as large. To reflect this, a truncated Gaussian was also introduced before convolution with the instrumental resolution, where the initial FWHM was $400\,\mathrm{km\,s^{-1}}$ and the blue half of the profile was set to be zero (i.e. the FWHM is now $200\,\mathrm{km\,s^{-1}}$). This profile produced similar recoverability statistics to the complete Gaussian simulations. For the XSHOOTER observations, it was found that a typical Lyman-α emission line with an intrinsic velocity width of about $200\,\mathrm{km\,s^{-1}}$ would be robustly picked up in the spectroscopy if it represented a S/N of 3.5-4σ (using a 5Å $\times 0\farcs8$ aperture for the Near-IR channel and a 4Å $\times 0\farcs8$ aperture for the optical channel). In the case of the GNIRS observations, whose data reduction is subject to more systematics than our XSHOOTER observations, a stricter 5σ detection threshold is imposed for a line with intrinsic velocity of $200\,\mathrm{km\,s^{-1}}$. Some of the GNIRS systematics arise from the low-refractive index layers of the anti-reflection coatings on the GNIRS lenses which contain radioactive thorium, causing the array to be peppered with spikes during long exposures. Additionally, the GNAAC controller of GNIRS superimposes systematics (vertical striping and horizontal banding).

In conjunction with the continuum flux inferred from the HST imaging, the spectroscopy is deep enough to allow us to place interesting rest-frame equivalent-width (EW) limits on Lyman-α emission from our objects as shown in Figures 3.11 – 3.19. The continuum is inferred from the broad-band photometry from HST, from the filter above the Lyman-α break, i.e. the F105W Y-band for the z'-drops at $z \approx 7$, and the F125W J-band for the Y-drops at $z \approx 8-9$. We assume here a rest-frame spectral slope above the Lyman-α break of the form $f_\lambda \propto \lambda^\beta$, where $\beta = -2$ (equivalent to a spectrum flat in f_ν) is adopted, as found to be typical of $z > 6$ galaxies (e.g. Wilkins et al. 2011), including the galaxies surveyed here (Bunker et al., 2010). A range of spectral slopes were experimented with, these varying between a redder slope of $\beta = -1.5$ and a bluer slope of $\beta = -2.5$, and it was found that this only changed the inferred rest-frame equivalent width limits by about 5 per cent (because the filter

used to infer the continuum lies at wavelengths just beyond Lyman-α). At the high redshift extreme of the expected redshift distribution (Figure 3.28), the Lyman-α break can encroach on the shortest wavelengths of the HST bandpass used to infer the continuum, and this was corrected for assuming total absorption below the Lyman-α wavelength at these redshifts (the Gunn-Peterson effect). In these cases a correction was also made for possible Lyman-α line emission contamination of the broad-band magnitude, given the upper limits on the line flux. The significance of the upper limits on the flux of an emission line, given the non-detections, depends on the wavelength (because the sky spectrum, atmospheric transmission and detector sensitivity vary with wavelength), and also on the spatial and spectral extent of any line emission.

The Lyman break galaxies at $z > 6$ are typically very compact in HST images (e.g., Oesch et al. 2010b finds a half-light radius $< 1\,\mathrm{kpc}$) and are unresolved in ground-based seeing. Hence a spatial extraction aperture about 1.5 times the seeing disk was adopted, in order to maximize the signal-to-noise ratio. The spectral extent (i.e. velocity width) of the Lyman-α emission is less certain. Two scenarios were considered: one where the line emission is unresolved at the spectral resolution of GNIRS or XSHOOTER (i.e. $\Delta v_{\mathrm{FWHM}} < 100\,\mathrm{km\,s^{-1}}$), and the other where the intrinsic line width is around $200\,\mathrm{km\,s^{-1}}$, similar to that seen in some Lyman break galaxies at $z \approx 6$ which have Lyman-α emission (e.g. Bunker et al., 2003, Stanway et al., 2004).

For XSHOOTER, the spectral resolution is $\approx 2.5\,$Å FWHM in the near-infrared (the optical arm of XSHOOTER has higher resolution of $1.4\,$Å), and a line with intrinsic velocity width of $\Delta v_{\mathrm{FWHM}} = 200\,\mathrm{km\,s^{-1}}$ would result in observed line widths of $6.5 - 8\,$Å FWHM, after convolution with the spectral resolution of the instruments. Hence a spectral extraction width of $4\,$Å (10 pixels) was adopted in the optical channel and $5\,$Å (5 pixels) was adopted for the infrared channel, intermediate in size between the wavelength spread of the emission lines in the two scenarios. Spatially, a size of

0.″8 was adopted for our aperture (which is 5pix in the optical channel and 4pix in the infrared channel). In the case of an unresolved line, 95.4% of the flux is captured with our aperture in the optical data and 87% of the flux is captured in the Near-Infrared data. For a $200\,\mathrm{km\,s^{-1}}$ line 48.5% of the flux is captured with our aperture in the optical data and 52.6% of the flux is captured in our Near-Infrared data. The above aperture corrections were applied in computing the flux limits.

In the case of the GNIRS observations, the spectral resolution is $\approx 2.56\,$Å FWHM, and a line with an intrinsic velocity width of $\Delta v_{\mathrm{FWHM}} = 200\,\mathrm{km\,s^{-1}}$ would correspond to an observed line width of $\approx 7\,$Å FWHM after convolution with the spectral resolution of the instrument. A spectral extent of $3.96\,$Å was adopted for our aperture (corresponding to 5 pixels in our pipeline output) and a spatial extraction width of 0.″75 (5pixels). Our square aperture (5×5-pixels) would capture 88% of the flux from a spectrally unresolved object, whereas for a $200\mathrm{kms}^{-1}$ it would capture 45% of the flux.

The validity of our 2D noise model was checked by placing the chosen extraction apertures at random on the 2D spectrum normalised by the noise model, and fitting a Gaussian to a histogram of the measured fluxes within the apertures (Figure 3.25 shows the results of this for all spatially-independent apertures in one of our XSHOOTER near-infrared spectra). The noise distribution was well-fit by a Gaussian with the expected noise properties. Some excess power in the wings (both positive and negative) was attributable to occasional isolated hot pixels or cosmic rays which had survived clipping in the data reduction, or sky line subtraction residuals. All $> 4\,\sigma$ events (measured in the adopted apertures) were investigated and none were found to be consistent with emission lines.

One of the objects targeted by our GNIRS spectroscopy, HUDF.zD1, has previously been investigated by Fontana et al. (2010), their source G2_1408, and they observe a tentative Lyman-α emission line at 9691.5Å with $f_{Ly\alpha} = 3.4{\times}10^{-18}\,\mathrm{erg\,cm^{-2}\,s^{-1}}$.

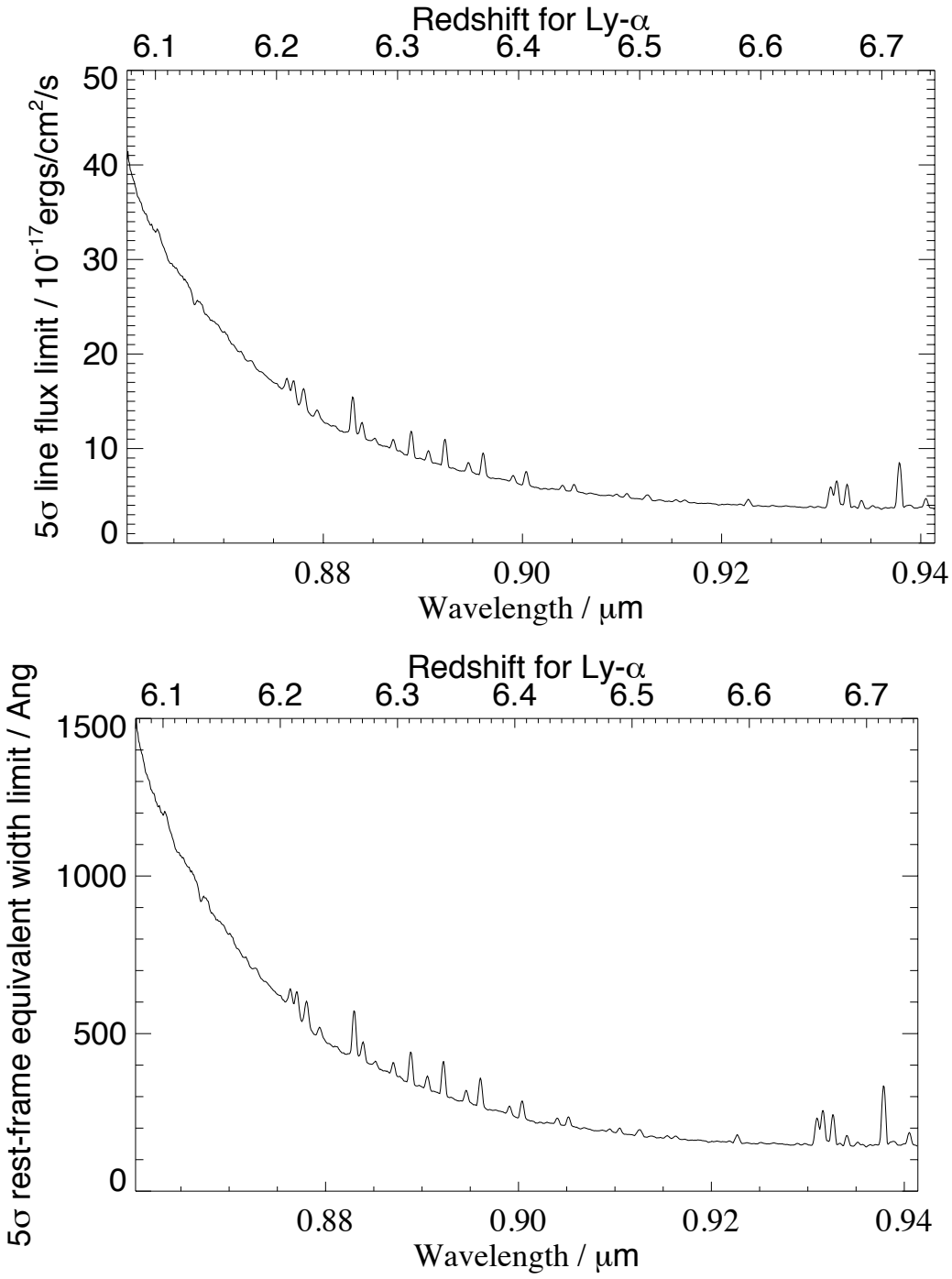

Figure 3.11: Line flux and Rest-Frame Equivalent Width limits for HUDF.zD1 from GNIRS observations. The upper panel shows the 5σ line flux limit probed by Order 5 of our spectroscopy using a grating angle of 21 and the XD_G0507 filter. This filter does not have good transmission in the 0.8-1.2μm range, which is why the sensitivity is not very good. The lower panel shows the 5σ Rest-Frame Equivalent Width limit for the redshift range probed by the same order of the same spectroscopic setting. Y_{AB}: 26.71. This plot (and all other EW upper-limit plots for GNIRS) assumes a spectrally unresolved source; a typical line with intrinsic velocity width of 200kms^{-1} would have to be about 2 times brighter than an unresolved line to be robustly detected in our GNIRS spectroscopy.

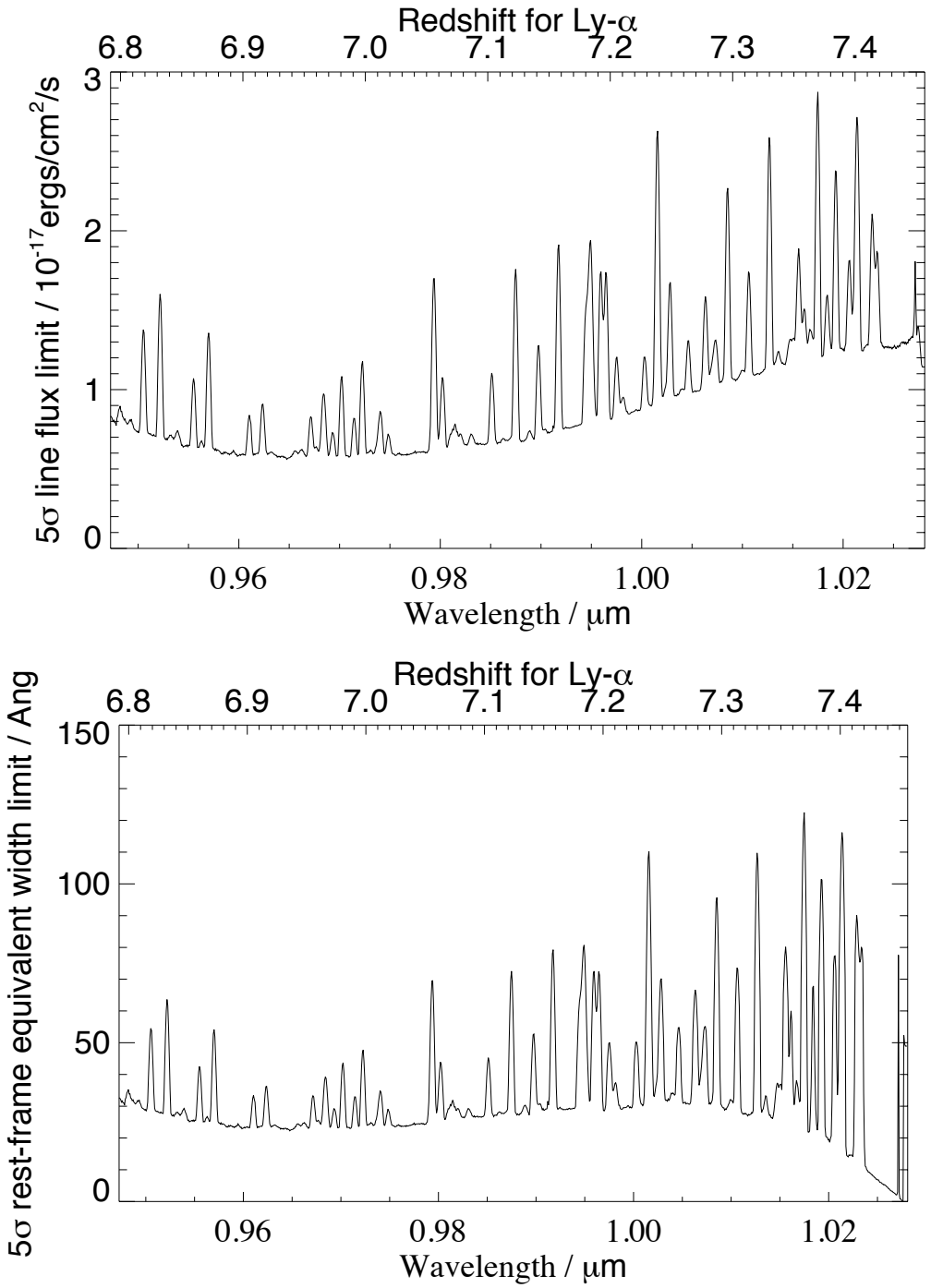

Figure 3.12: Line flux and Rest-Frame Equivalent Width limits for HUDF.zD1 from GNIRS observations (continued). The upper panel shows the 5σ line flux limit probed by Order 5 of our spectroscopy using a grating angle of 23.2 and the the XD_G0525 filter. The lower panel shows the 5σ Rest-Frame Equivalent Width limit for the redshift range probed by the same order of the same spectroscopic setting. Y_{AB}: 26.71.

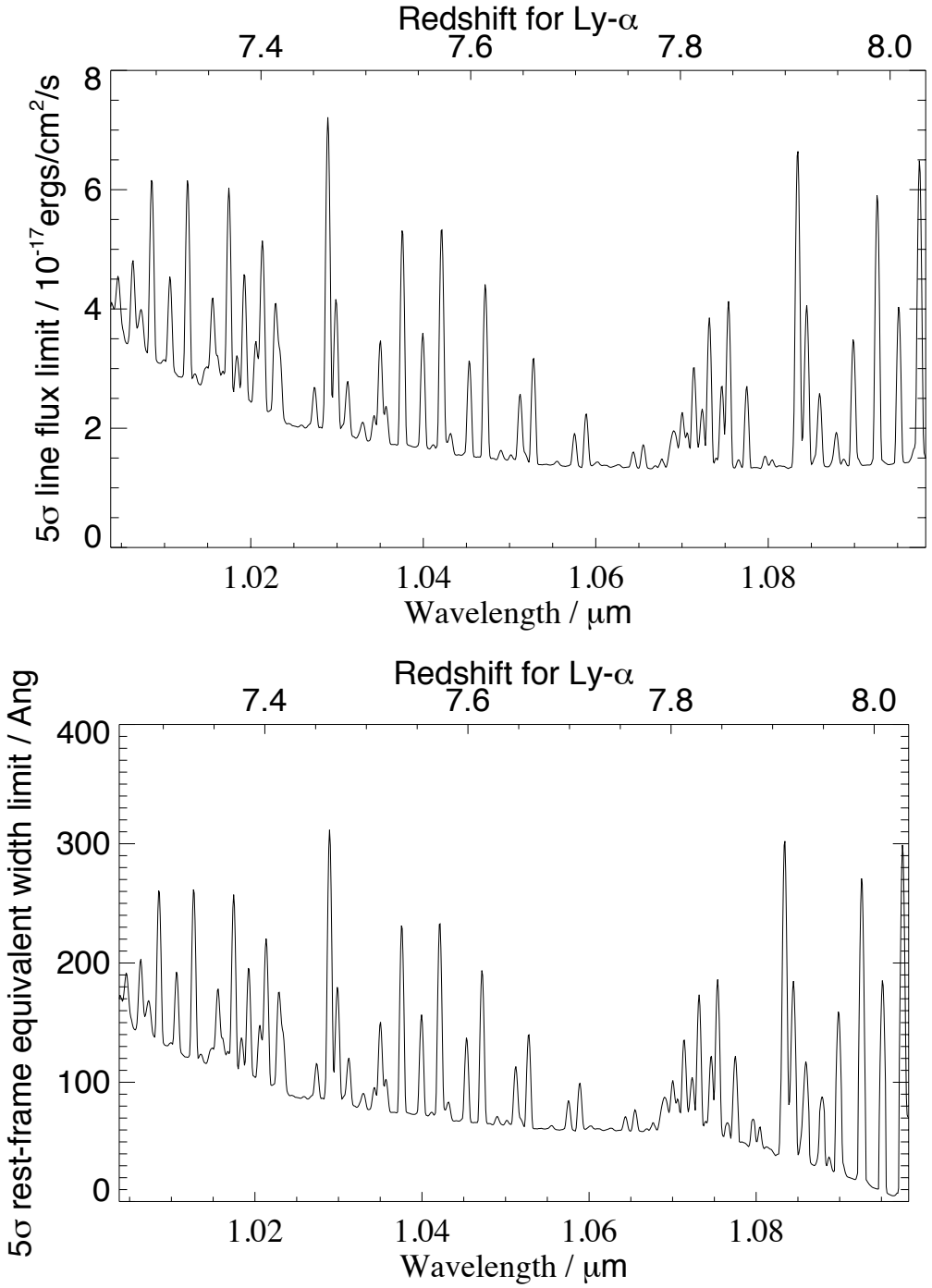

Figure 3.13: Line flux and Rest-Frame Equivalent Width limits for HUDF.zD1 from GNIRS observations (continued). The upper panel shows the 5σ line flux limit probed by Order 4 of our spectroscopy using a grating angle of 21 and the XD_G0507 filter. The lower panel shows the 5σ Rest-Frame Equivalent Width limit for the redshift range probed by the same order of the same spectroscopic setting. Y_{AB}: 26.71.

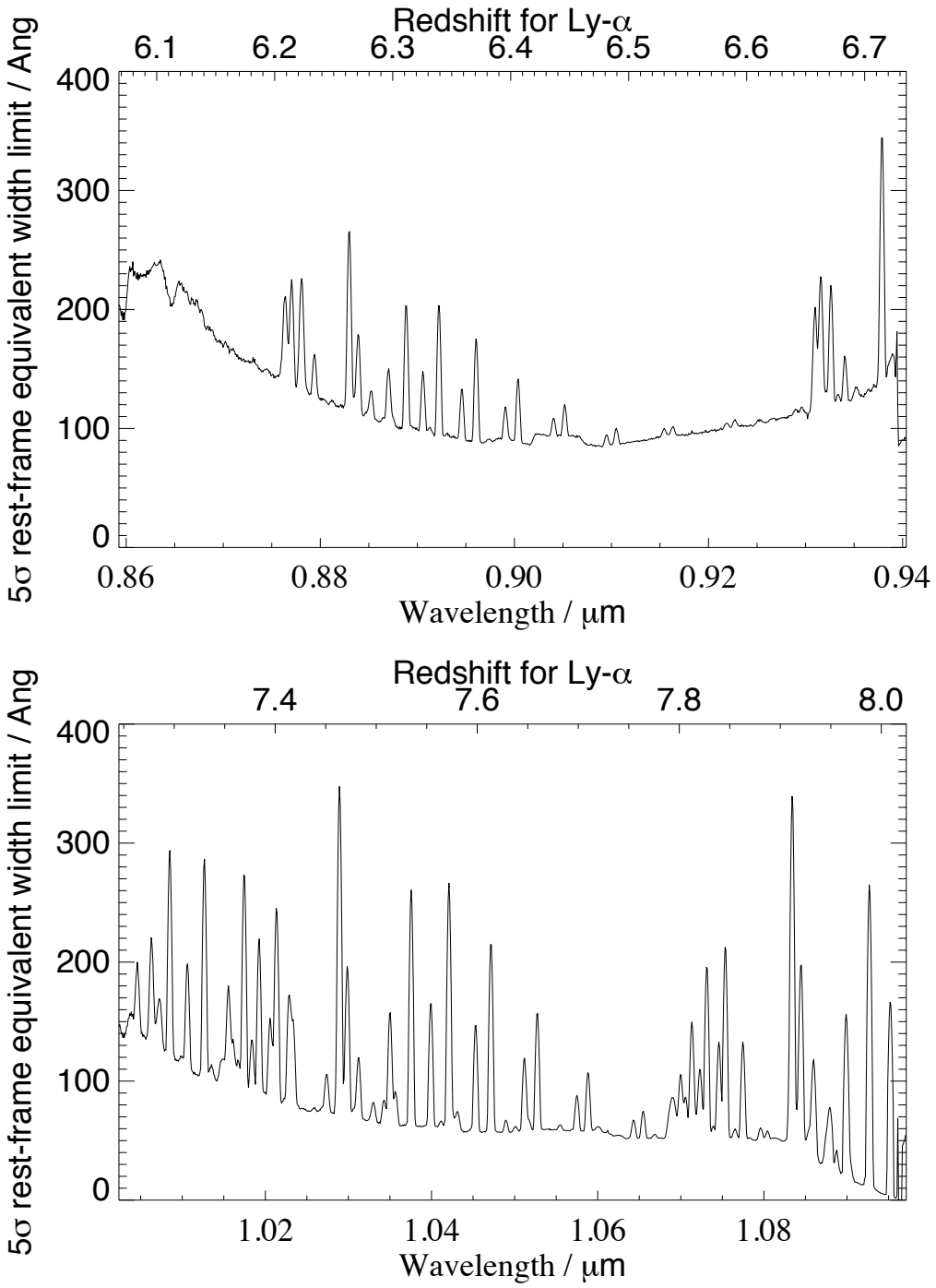

Figure 3.14: 5σ Rest-Frame Equivalent Width limit for HUDF.zD2 from GNIRS observations. The upper panel shows the redshift range probed by Order 5 of our spectroscopy using a grating angle of 21 and the XD_G0525 filter. The lower panel shows the redshift range probed by Order 4. Y_{AB}: 27.48.

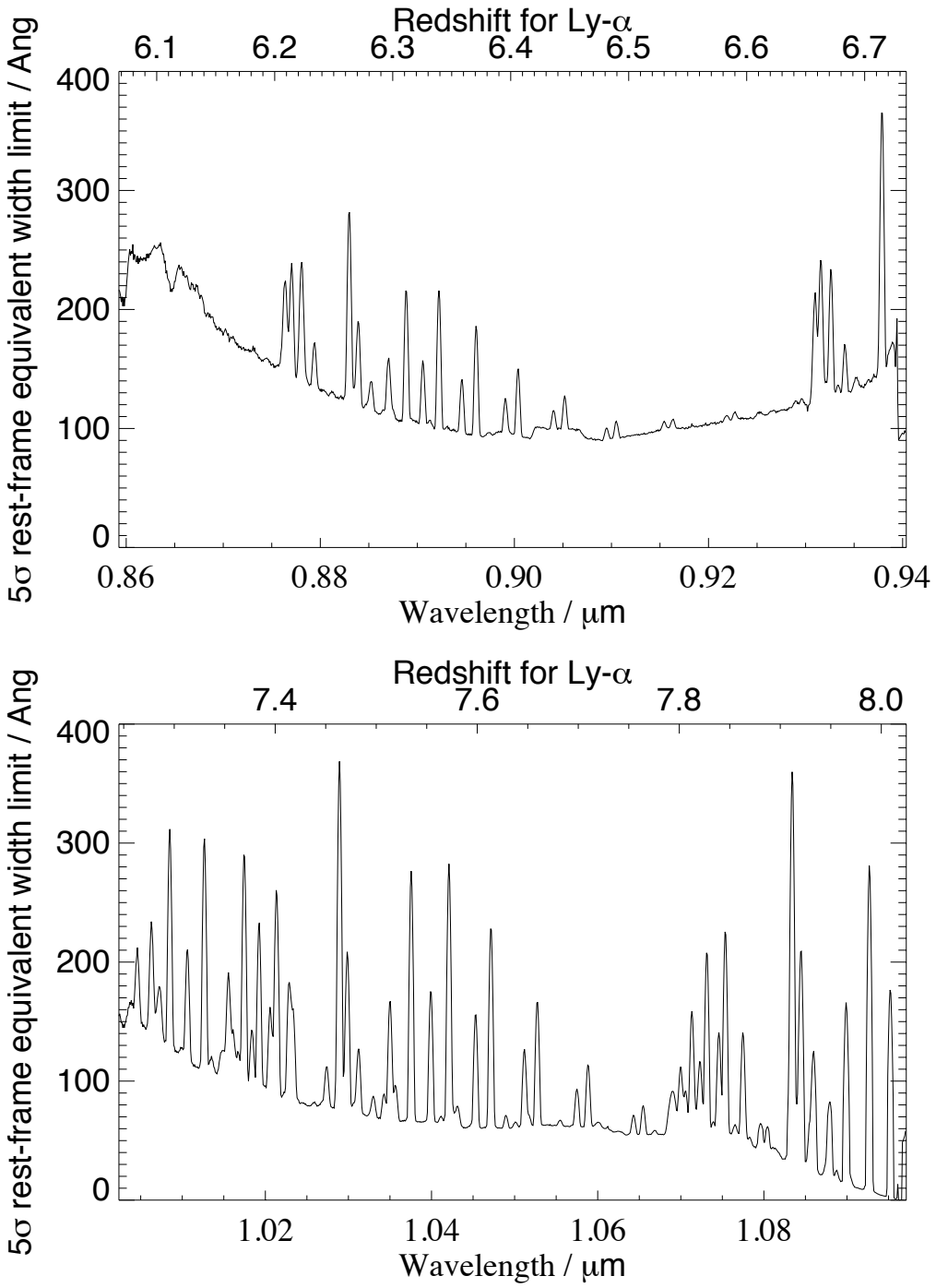

Figure 3.15: 5σ Rest-Frame Equivalent Width limit for HUDF.zD3 from GNIRS observations. The upper panel shows the redshift range probed by Order 5 of our spectroscopy using a grating angle of 21 and the XD_G0525 filter. The lower panel shows the redshift range probed by Order 4. Y_{AB}: 27.5.

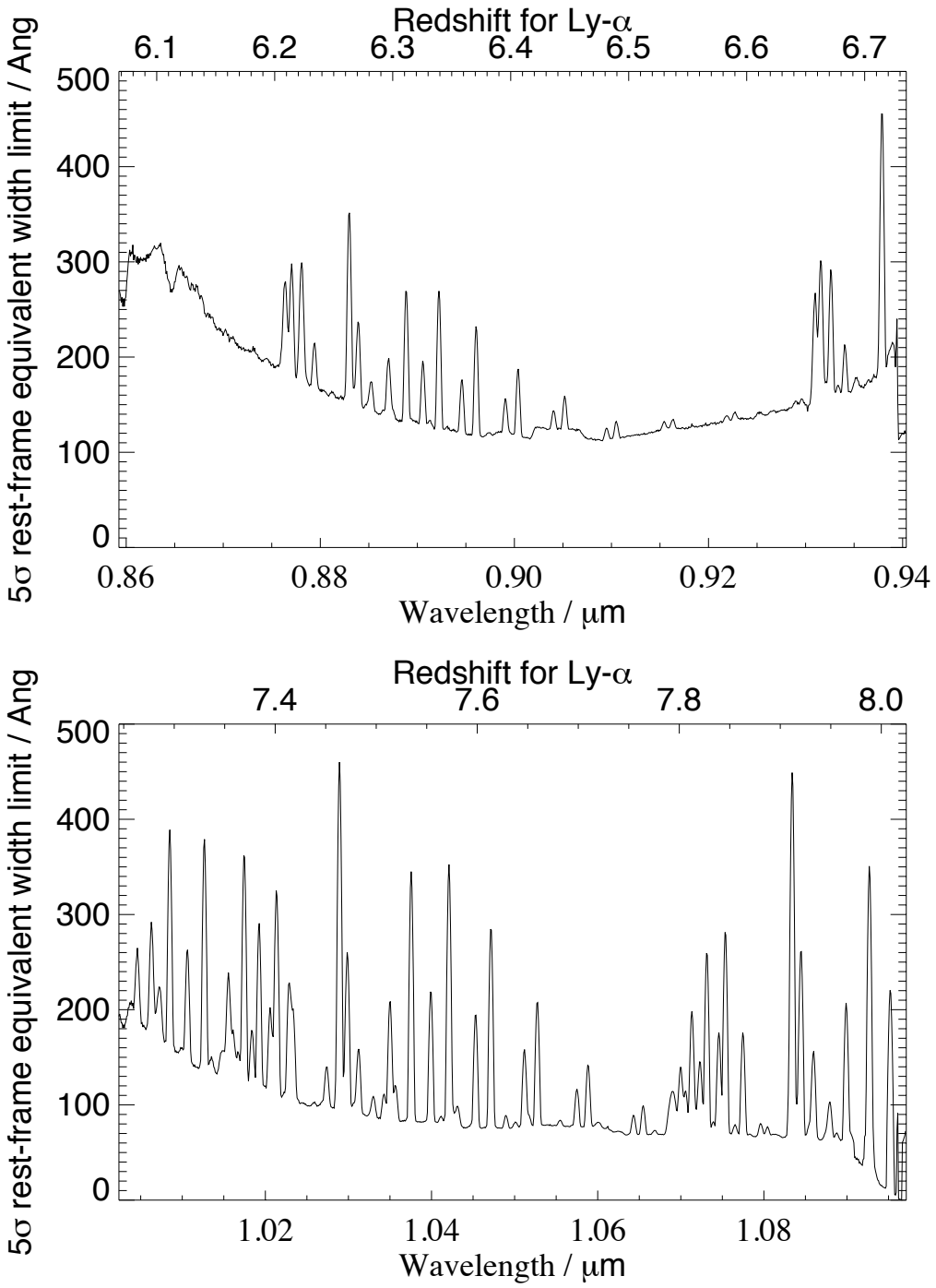

Figure 3.16: 5σ Rest-Frame Equivalent Width limit for HUDF.zD4 from GNIRS observations. The upper panel shows the redshift range probed by Order 5 of our spectroscopy using a grating angle of 21 and the XD_G0525 filter. The lower panel shows the redshift range probed by Order 4. Y_{AB}: 27.84.

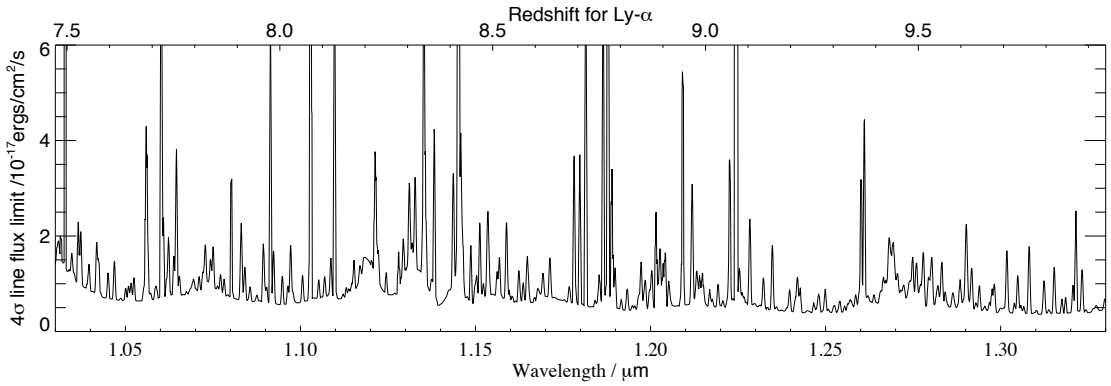

Figure 3.17: 4σ line flux limit for our observations with the Near-IR channel of XSHOOTER.

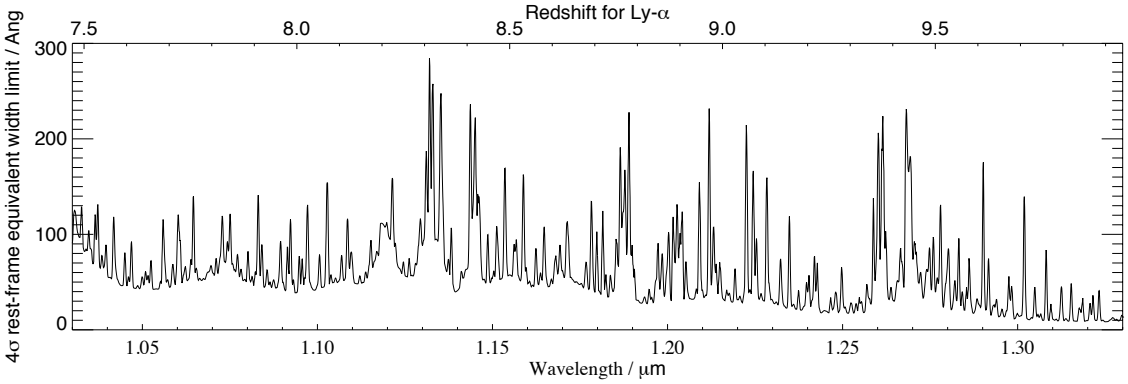

Figure 3.18: 4σ Rest-Frame Equivalent Width limit for ERS.YD2 from observations with XSHOOTER. This plot and the next two EW upper-limit plots for XSHOOTER observations of HUDF.YD3 and P34.z.4809 assume a spectrally unresolved source; a typical line with intrinsic velocity width of 200kms^{-1} would have to be about 1.5 times brighter than an unresolved line to be robustly detected in our XSHOOTER spectroscopy (i.e. the limits plotted here correspond to $\approx 3\sigma$ for such a spectrally resolved line).

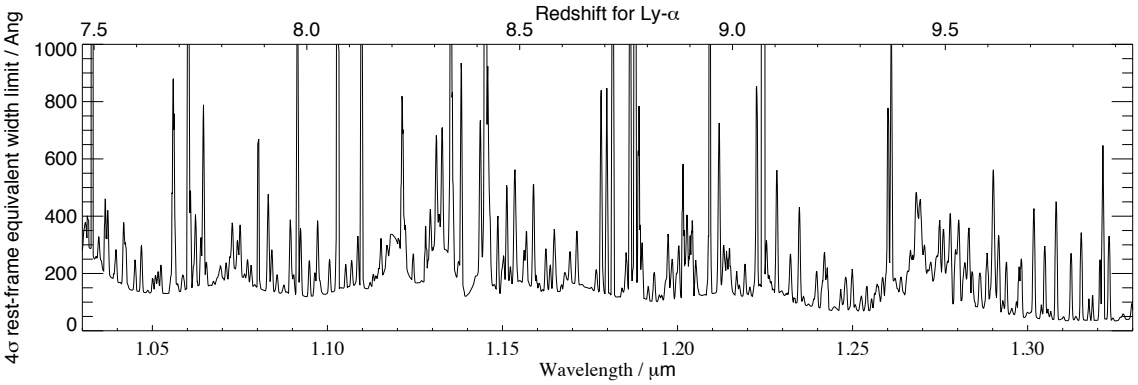

Figure 3.19: 4σ Rest-Frame Equivalent Width limit for HUDF.YD3 from observations with XSHOOTER.

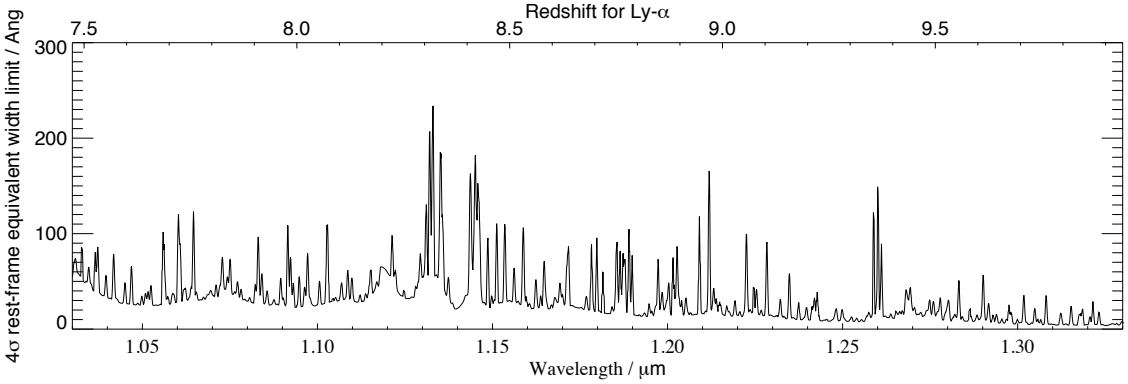

Figure 3.20: 4σ Rest-Frame Equivalent Width limit for UDF092y-03751196d from observations with XSHOOTER.

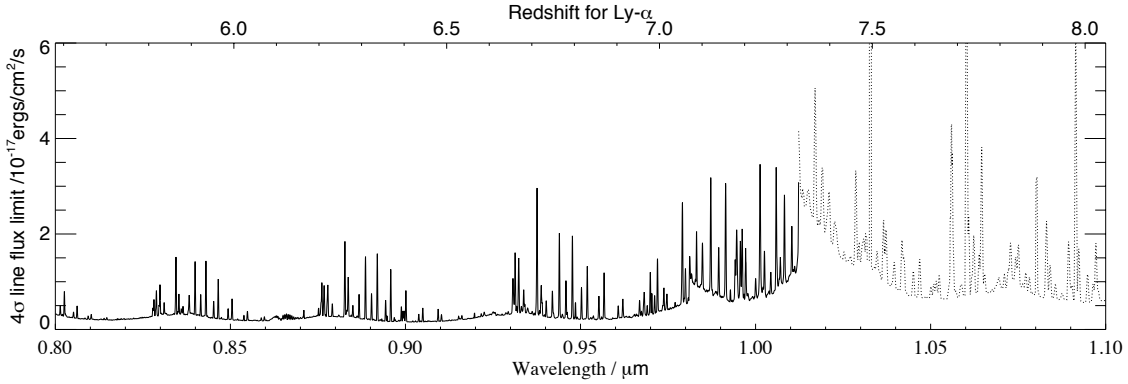

Figure 3.21: 4σ line flux limit for our observations of P34.z.4809 with the Optical and Near-IR channels of XSHOOTER. The region of the figure shown with a dotted line represents the limit obtained form data acquired with the NIR channel.

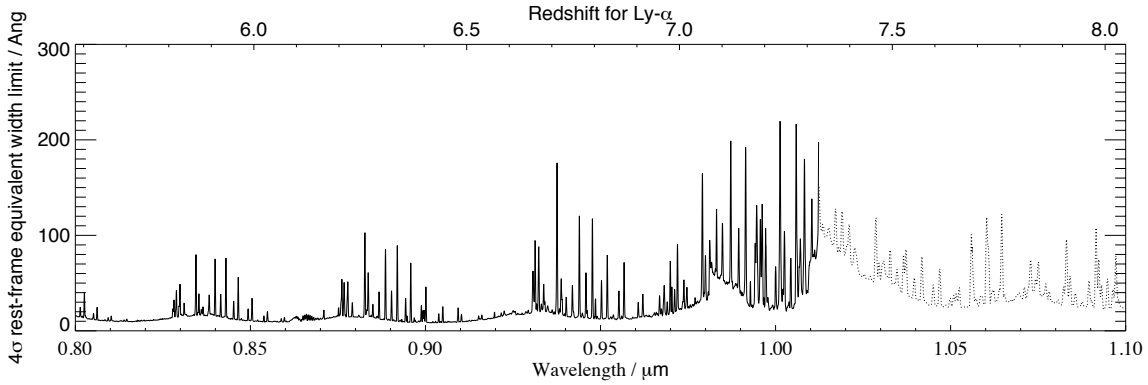

Figure 3.22: 4σ Rest-Frame Equivalent Width limit for P34.z.4809 from observations with XSHOOTER. The region of the figure shown with a dotted line represents the limit obtained from data acquired with the NIR channel.

This wavelength region in our GNIRS spectrum of this object was looked at closely. At this wavelength, our measured $1\,\sigma$ noise using a 3.96Å$\times$0.″75 aperture (5$\times$5 pixels) is $1.01 \times 10^{-18}\,\mathrm{erg\,cm^{-2}\,s^{-1}}$. For a spectrally-unresolved emission line with the same flux as the Fontana et al. object, one would expect a $3\,\sigma$ detection in our GNIRS data. However, Fontana et al. report a marginally spectrally-resolved line profile of 10 Å FWHM (with an instrumental width of 7 Å FWHM for FORS 2), corresponding to an intrinsic velocity spread of $200\,\mathrm{km\,s^{-1}}$ FWHM, after deconvolution with their instrumental resolution. At our GNIRS resolution one would expect such a line to have 7 Å FWHM. For this velocity profile and line flux, one would only expect a $1.7\,\sigma$ signal within our 5×5 pixel aperture. Hence our non-detection does not rule out the Fontana et al. line detection, particularly if it has significant velocity extent. One should note that although HUDF.zD1 is well resolved in the WFC 3 imaging and indeed comprises two distinct components separated by 2 kpc (0.″37) and with half-light radii of $0.5 - 0.8$ kpc (Oesch et al. 2010b), in ground-based seeing this galaxy pair is unresolved. The effects of the finite source size (before seeing) was included in our calculation of the slit losses. The same target was also observed with VLT/FORS2, and the results are discussed in the next Chapter.

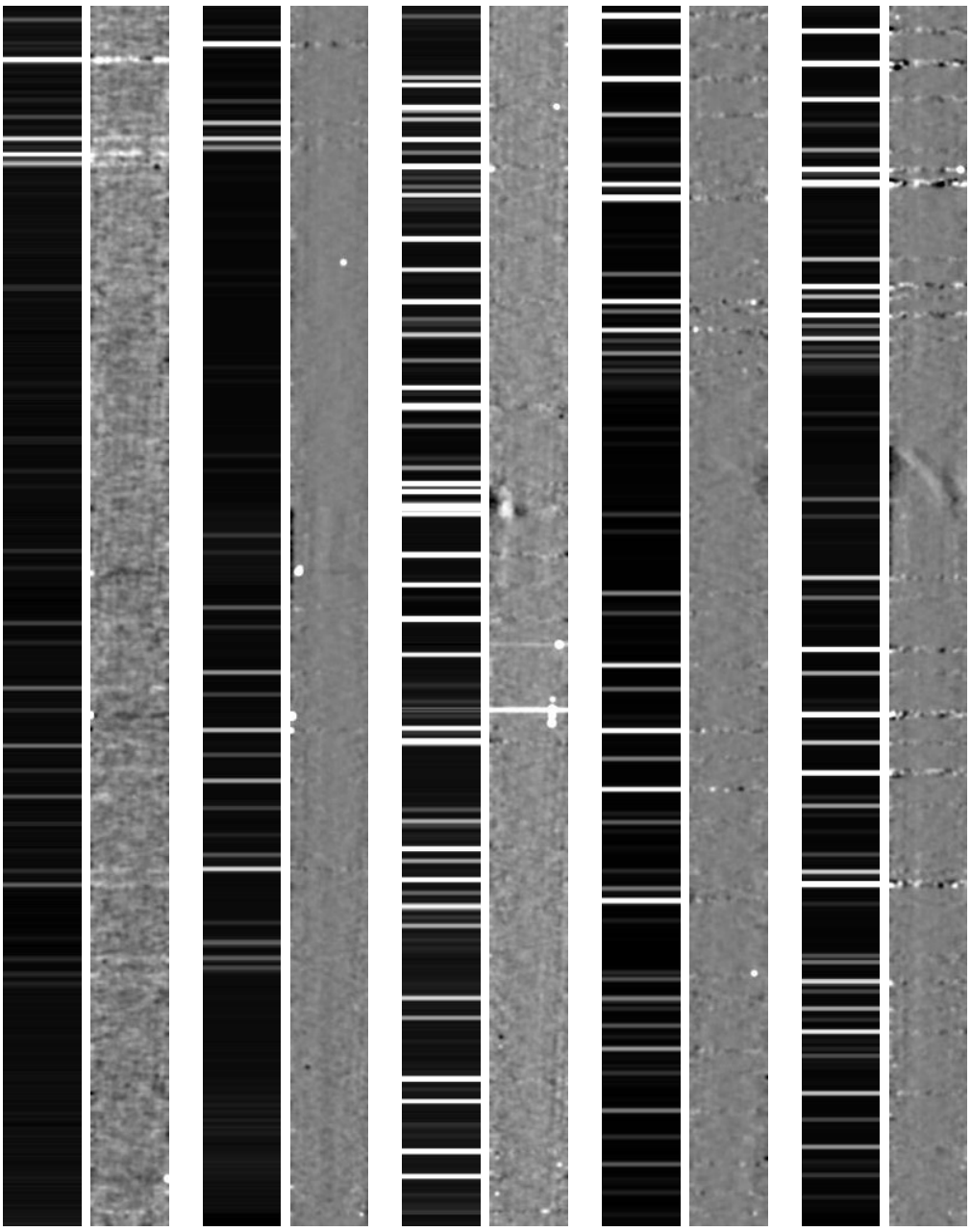

Figure 3.23: This figure shows typical reduced 2D frames from all the different spectroscopic settings used for our GNIRS observations, together with the corresponding 2D frames showing sky emission lines. From top to bottom, (a) the 0.84-0.94μm wavelength range covered with the XD_G0507 filter and a grating angle of 21 (order 5), (b) the same wavelength region covered with the XD_G0525 filter and a grating angle of 21 (order 5), (c) the 0.95-1.03μm wavelength range covered with the G_0525 filter and a grating angle of 23.2 (order 5), (d) the 1.005-1.095μm wavelength range covered with the G_0507 filter and a grating angle of 21 (order 4), and (e) the same wavelength region covered with the XD_G0525 filter and a grating angle of 21 (order 4). Wavelength increases from bottom to top.

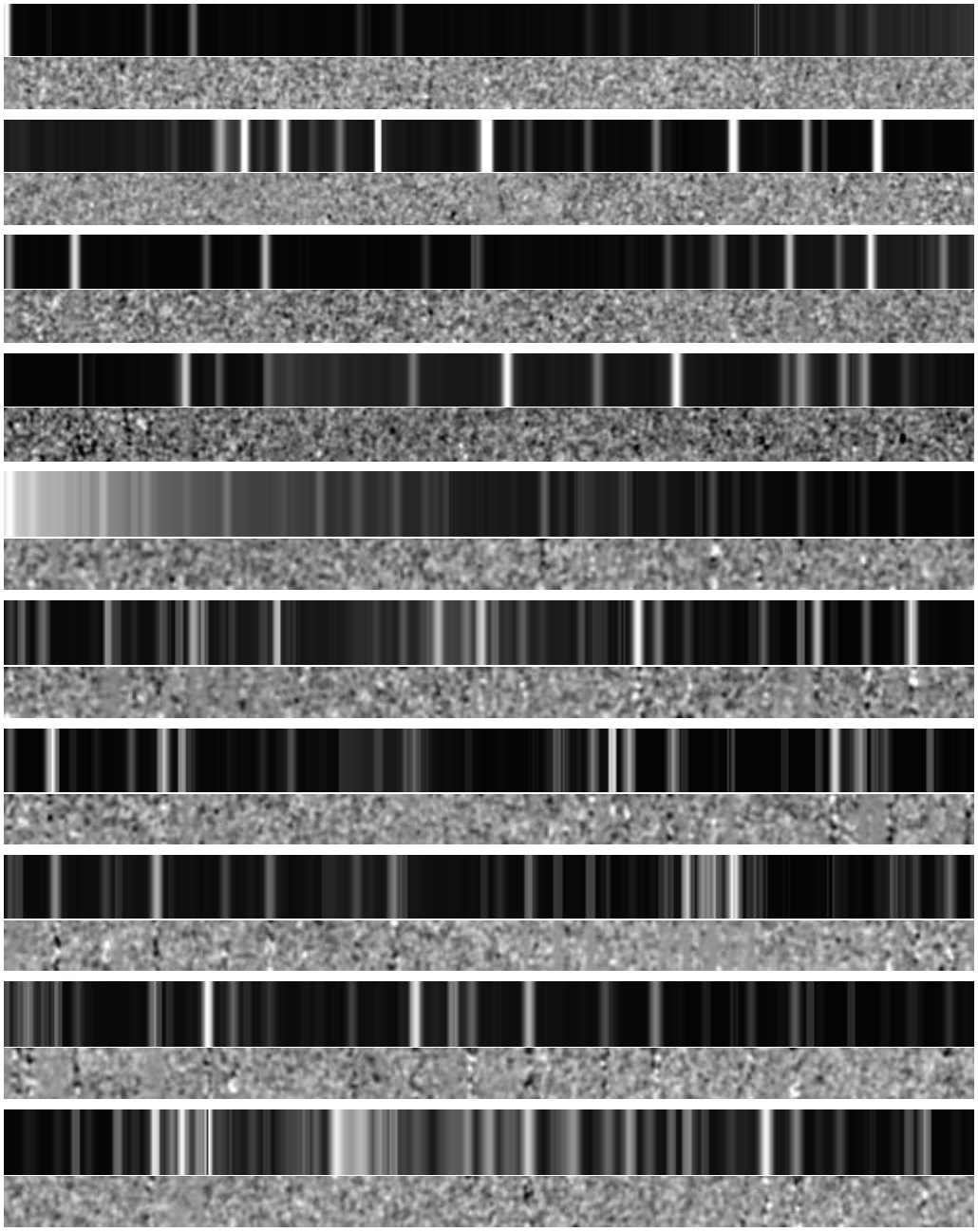

Figure 3.24: This figure shows typical reduced 2D frames for XSHOOTER, together with the corresponding 2D frames showing sky emission lines. Displayed here is the wavelength range where Lyman-α is expected to lie for z-drops and y-drops. From top to bottom, the first four panels show reduced data from the optical channel (here showing P34.z.4809), and together span the 0.9μm-1.0μm wavelength range, each panel spanning 0.025μm with wavelength increasing from left to right. The following six panels show reduced data from the Near-IR channel (here showing UDF092y-03751196d) and together span the 1.0μm-1.3μm wavelength range, each panel spanning 0.05μm with wavelength increasing from left to right.

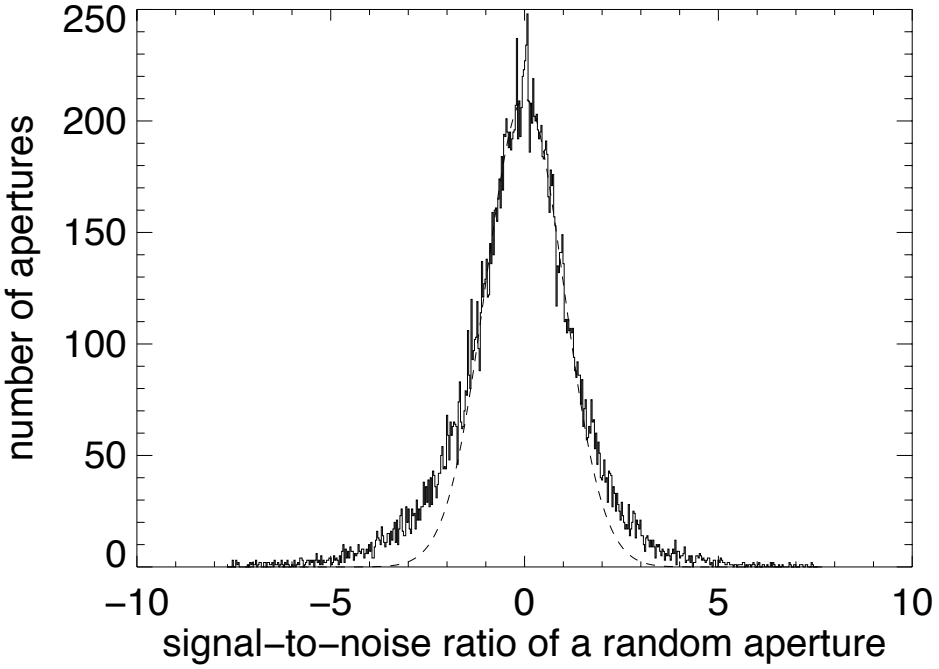

Figure 3.25: This plot for one of our XSHOOTER Near-InfraRed spectra shows the histogram of measured counts in independent 5×4 pixel apertures. The core distribution is well-fit by a Gaussian with the expected noise properties. The non-Gaussian extremes of the distribution are due to a small number of data reduction artefacts.

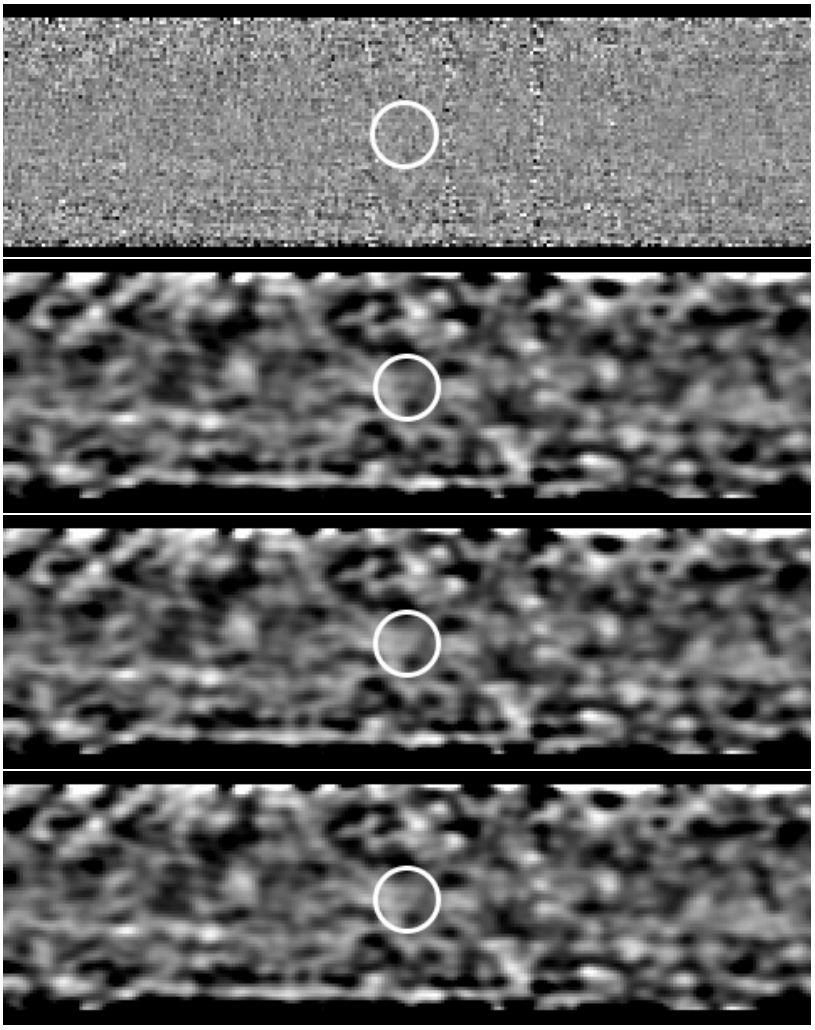

Figure 3.26: The calibrated GNIRS spectrum, with the location of HUDF.zD1 and the expected wavelength of the tentative Lyman-α emission reported by Fontana et al. (2010) marked with a white circle. Wavelength increases from left to right, and we show the 95 Å either side of 9691.5 Å. From left to right: (a) the reduced data. The three vertical lines of higher noise are due to night sky emission lines; (b) the reduced data convolved with an elliptical Gaussian with σ of 1.4 pixels spatially and 2.2 pixels spectrally, matching the profile of a Gaussian emission line with FWHM of 0.″5 and 2.6 Å. (c) a fake source with the same line flux (3.4×10^{-18} erg cm^{-2} s^{-1}) and wavelength as the Fontana et al. (2010) line added into the frame. The resulting frame has been Gaussian smoothed. A spatially and spectrally unresolved source is assumed. If the line is spectrally resolved, the S/N would be lower – panel (d) shows the expected 2D Gaussian-smoothed spectrum for an emission line with an intrinsic velocity width of 200 km s^{-1} (FWHM) and the same line flux as reported in Fontana et al. (2010).

3.7 Analysis

3.7.1 The EW distribution and Constraints on the Neutral Fraction χ_{HI}

Given the fact that no Lyman-α emission is detected in any of our spectra, what can one say about the strength of Lyman-α emission in $z > 7$ galaxies? The broad-band filters used to colour-select candidates with the Lyman break technique introduce a selection function on the redshift. The expected redshift distribution used for our sample is taken from the simulations described in Wilkins et al. (2011) at $z = 7$ for the z-band dropouts and Lorenzoni et al. (2011) at $z = 8$ for the Y-band dropouts, which are reproduced in Fig.3.28. The probability of recovering a galaxy as a function of redshift is computed for different rest-frame UV absolute magnitudes around $\lambda_{rest} = 1600\,\text{Å}$ (M_{1600}). For each spectroscopic target, calculated M_{1600} is calculated so that for every object, the most appropriate scenario to use from the simulations in Fig.3.28 could be determined, choosing the relevant curve for a given M_{1600} and field (eg. HUDF, P34 etc). These curves give the probability of recovering a galaxy at a given redshift.

Different thresholds on the rest-frame EW (50 Å, 75 Å and 120 Å) were then considered for each of our targets. For each particular target and chosen EW threshold, the fraction of our spectroscopy that had EW limits lower than our chosen threshold (i.e. the fraction of the spectrum where $\text{EW}_{\text{upperlimit}} < \text{EW}_{\text{threshold}}$, which is called $\text{Frac}_{\text{EW<thres}}$ was computed, weighted by the redshift probability distribution for the dropout galaxy).

By considering the likelihood function for a galaxy to be lying at a particular redshift, one can compute the fractional probability, Frac_z, that a galaxy drawn from the dropout sample would fall within the spectral coverage of that spectrograph setup (tabulated in column 3 of Table 3.5). Multiplying Frac_z by $\text{Frac}_{\text{EW<thres}}$ (found in

columns 5-7 of Table 3.5) and computing the sum over all the galaxies observed gives the effective total number of galaxies, $N_{\rm eff}$, where the sensitivity is greater than the chosen EW threshold. These are tabulated in Table 3.6.

Given that no Lyman-α emission is detected in the data, what scenarios of EW evolution from lower redshift can be ruled out? From Poisson statistics, if a given model predicts that on average $\lambda_{\rm ex}$ galaxies are expected to be detected in the survey, the probability f_n of detecting n galaxies is given by:

$$f_n = \frac{(\lambda_{\rm ex})^n e^{-\lambda_{\rm ex}}}{n!} \tag{3.3}$$

No galaxies are detected in our survey ($n = 0$), and so, models which predict $\lambda_{\rm ex}$ detections can be rejected at the $(1 - f_n)$ level; i.e. a model which predicts 1 galaxy is rejected at the 63 per cent level (roughly corresponding to $1\,\sigma$ for a Normal distribution), and a model which predicts 3 galaxies are detected is rejected with 95% confidence (corresponding to about $2\,\sigma$ for a Normal distribution).

Specifically, one can rule out at the 63 percent ($\approx 1\,\sigma$) level any scenario that predicts a fraction of galaxies with Lyman-α emission above the threshold EW, of $X_{Ly\alpha} > 1/N_{\rm eff}$ (taking $\lambda_{\rm ex} = X_{Ly\alpha} \times N_{\rm eff} = 1$ in the above equation). Here the results of this work are compared with the work of Stark et al. (2010), building on the previous work of Stanway et al. (2007) at $z = 6$ and Shapley et al. (2003) at $z = 3$. Stark et al. (2010) determined the fraction of dropout galaxies with EW $\gtrsim 75\,$Å at lower redshift ($z = 4 - 6.5$), and showed that over this redshift range the fraction of strong Lyman-α emitters increased with increasing redshift. The four data points with error bars in Figure 3.27 are from Stark et al. (2010) and show the fraction of strong Lyman-α emitters at different redshifts in their spectroscopic dropout sample, which covers a range in UV luminosities of $-19.5 > M_{UV} > -20.5$, similar to the range of luminosities of our higher-redshift sample presented here. A point at $z = 3$

is also added from Shapley et al. (2003), who carried out a study of 957 U-band drop-out galaxies. A simple linear extrapolation in redshift of this trend is made out to $z = 8.5$ (dotted line), where our observations are sensitive with the Y-drops. This scenario would correspond to constant evolution (linear with redshift) in the intrinsic Lyman-α EW distribution coupled with no evolution in the neutral fraction from lower redshifts, with $\chi_{HI} = 0$. The three upper-limit arrows in Figure 3.27 show the constraints derived from our observations; the tail and head of the arrows represent the expected fraction of Lyman-α emitting galaxies with EW< 75 Å and EW< 120 Å respectively. The arrow at $z = 7$ shows the constraint obtained from our z-drops, and the one at $z = 8.5$ shows the constraint from our Y-drops. The mean redshift for z-drops and Y-drops was derived from the simulations by Wilkins et al. (2011) and Lorenzoni et al. (2011). The arrow in the middle at $z = 7.8$ is the constraint obtained by considering the z-drops and Y-drops together, at a mean redshift of $z = 7.8$. For a spectrally-unresolved line, we would expect on average 1.2 galaxies to be detected in our combined sample if the extrapolated evolution of the Lyman-α fraction holds (i.e. $X_{Ly\alpha} \approx 0.3$ at $z = 7.8$); no galaxies are detected, and hence the hypothesis is mildly inconsistent with our upper limits at the 70 per cent level. If the emission lines have intrinsic velocity widths of $\approx 200\,\mathrm{km\,s^{-1}}$, then one would expect only 0.64 galaxies to have detectable Lyman-α emission in our sample adopting the extrapolated $X_{Ly\alpha}$, so this scenario cannot be ruled out with these current data (it is formally inconsistent with our upper limit only at the 47 per cent level).

3.7.2 Comparison with other studies

In this section, our observations are directly compared with the studies made by Fontana et al. (2010), Pentericci et al. (2011), Vanzella et al. (2011), Schenker et al. (2012) and Ono et al. (2012) which were discussed in Chapter 1. All of the objects discussed above were brighter in the Y-band than any of our spectroscopic targets.

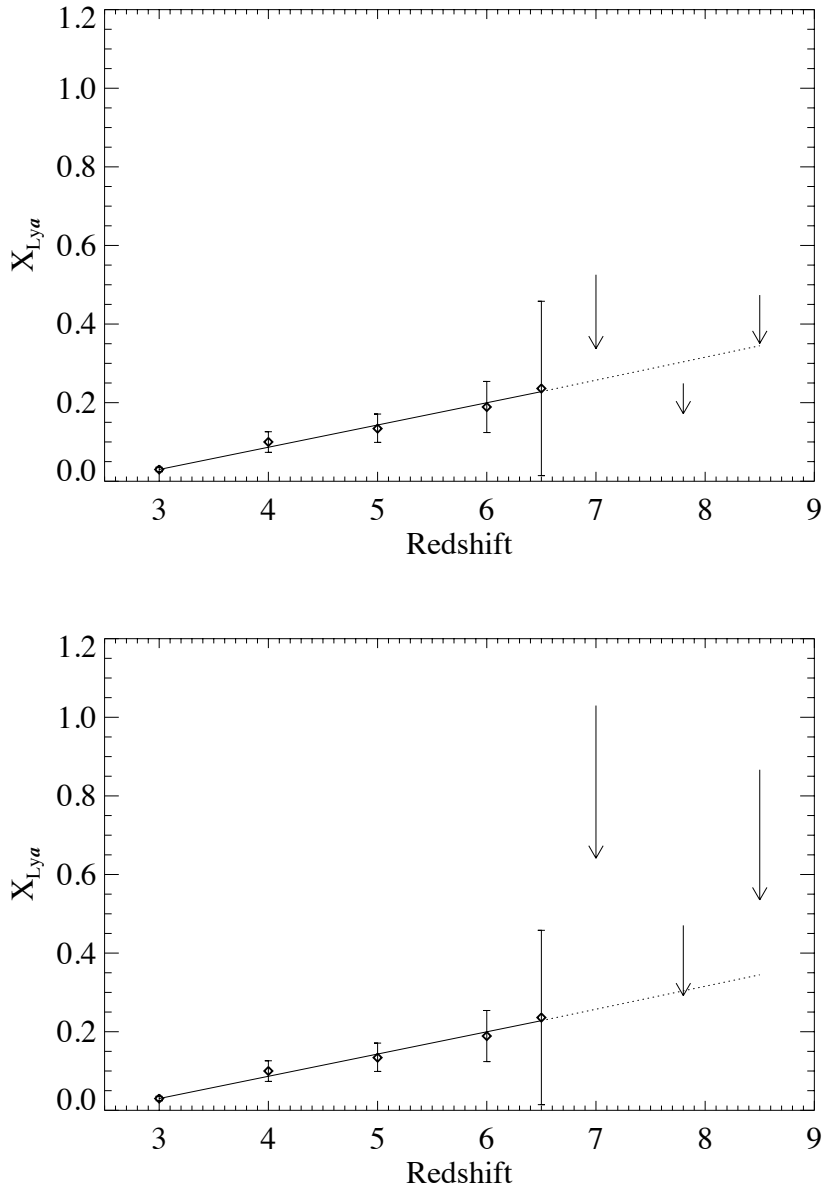

Figure 3.27: Our upper limits on the fraction of high rest-frame equivalent Lyman-α emission at $z \geq 7$ are shown for the z-drops ($z = 7$), the Y-drops ($z = 8.5$) and our complete sample (with mean $z = 7.8$). The head of each arrow is the 120 Å limit and the tail of each arrow is the 75 Å limit. The diamond symbols are results obtained at lower redshift by Shapley et al. (2003) at $z = 3$ and Stark et al. (2010) at $z = 4 - 6.5$. For comparison, we extrapolate the low-redshift trend to higher redshifts (dotted line). Our upper limits appear inconsistent with this extrapolation at the $1\,\sigma$ level, perhaps indicating that the IGM neutral fraction $\chi_{HI} > 0$ at $z > 7$. The upper figure shows our constraints when considering an unresolved line, whereas the lower figure considers a line with an intrinsic velocity width of 200km/s.

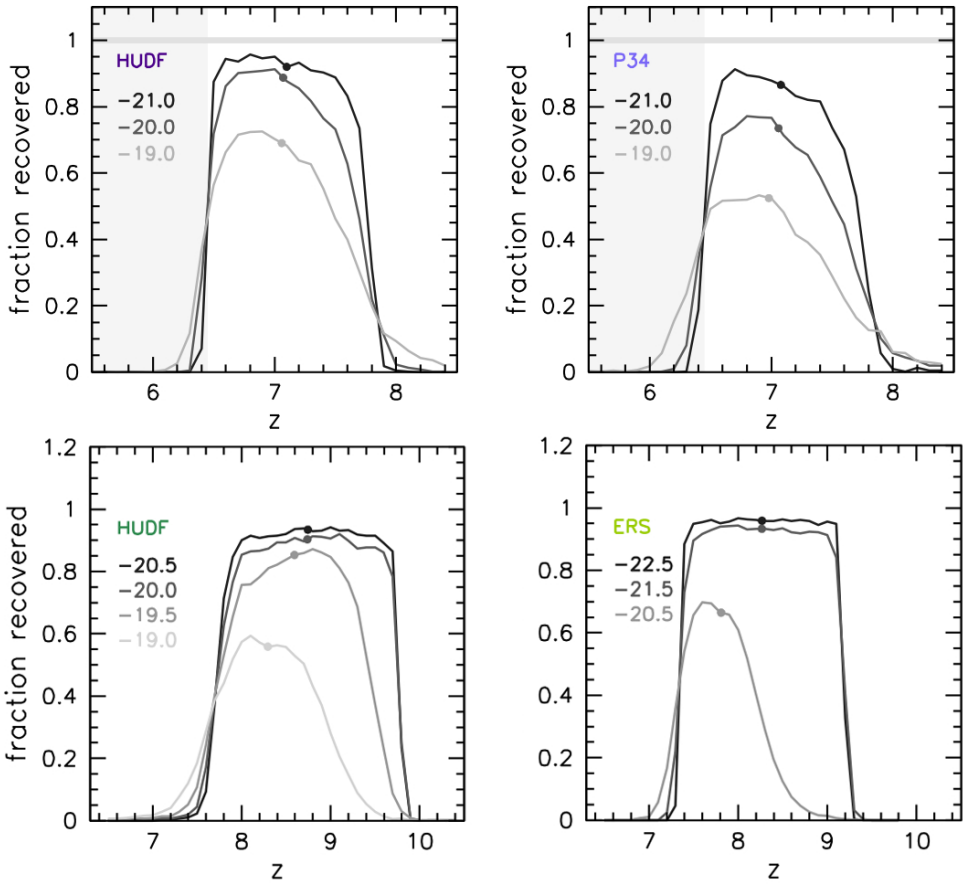

Figure 3.28: The probability of recovering a galaxy in the simulations described in Wilkins et al. (2011) and Lorenzoni et al. (2011) for different fields as a function of redshift for several different absolute rest-frame M_{1600} magnitudes. In this thesis, we use the results of these simulations to provide the expected redshift distributions. The upper two figures show the simulations for z-band dropouts (Wilkins et al., 2011) whereas the lower two figures are for Y-band dropouts (Lorenzoni et al., 2011). In each case, the mean redshift is denoted by a dot.

Would Lyman-α emission from any of these objects have been detected in the spectroscopy presented here, these objects were targeted? To perform these comparisons an appropriate line profile was first considered for each individual object; in each case, the emission was assumed to be spatially unresolved, whereas for the spectral extent of the lines the published values were adopted, and these were convolved with the spectral resolution of our instruments[5]. Our aperture was chosen to be about twice the size of the adopted emission line profile (spatially and spectrally) and aperture corrections were performed to allow for any loss in flux in our apertures. The results of these comparisons are reported in Table 3.4. In summary, the conclusion is that nearly all objects with the line fluxes detected by other groups would have been clearly detected in our spectroscopy[6]. However, one should note that the detections presented by other groups are typically for objects with brighter broad-band magnitudes, and hence the equivalent widths are small. Only 4 of the 9 objects in Table 3.4 have rest-frame equivalent widths $\geq 50\,\text{Å}$, where our observations are sensitive over an appreciable redshift range. The others have smaller rest-frame equivalent widths, which would be probed only by our spectra of P34.z.4809 and zD2 (around 1.05μm). This suggests that whilst there might indeed be no Lyman-α emission escaping the objects which we targetted in our spectroscopy, the negative results could also be due the the possibility of the emission being fainter than our detection limits, particularly given that our targetted objects are fainter than any of the other objects in literature discussed above. It has been suggested, however, that the fraction of high equivalent-width Lyman-α emitters is larger for faint galaxies (Stark et al. 2010, 2011), which

[5]A1703_zD6 was unresolved in the observations of Schenker et al. using NIRSPEC ($\Delta\lambda_{\text{FWHM}} = 6.5$Å), so here it is assumed that this object would be unresolved in our observations with GNIRS and XSHOOTER.

[6]As can be seen from Table 3.4, the only two objects which would not have been detected in either GNIRS or XSHOOTER are NTTDF-6345 and NTTDF-474, whose Lyman-α flux is measured to be quite low. ERS 8496 (which also has a relatively low measured Lyman-α flux) would have been undetected in our GNIRS observations, but would have been clearly detected in our XSHOOTER data. BDF-3299, on the other hand, would have been detected in our GNIRS observations, but not in our XSHOOTER data.

means that our derived upper limits on the equivalent width of these objects, shown in figures 3.11 - 3.22, may offer stronger constraints on χ_{HI}.

3.8 CONCLUSIONS

This chapter presented spectroscopic observations made with GEMINI/GNIRS and VLT/XSHOOTER of a sample of $z > 7$ candidate galaxies. Significant Lyman-α emission was not detected in any of them. This is consistent with the fraction of high rest-frame equivalent width Lyman-α emitters dropping at $z > 7$, as would be expected if the neutral HI fraction was greater at these epochs. A tentative emission line published by Fontana et al. (2010) in HUDF.zD1 (from the catalogue of Bunker et al. 2010) was also investigated, and the analysis presented in this chapter does not confirm the presence of this line, although the possibility of it being real cannot be ruled out, especially if it has considerable velocity extent.

Given the lack of Lyman-α emission in our spectroscopy in conjunction with the continuum flux derived from HST imaging of these objects, upper limits on the rest-frame equivalent width of our objects were derived. Extrapolating the Lyman-α fraction observed at lower redshifts by Stark et al. (2010) and Shapley et al. (2003), the lack of Lyman-α detection rules out at a level of $1\,\sigma$ (70%), for spectrally unresolved lines, the scenario in which the Lyman-α fraction evolves with the same trend found at lower redshifts. The limits are weaker if the lines have significant velocity width extent. A diminished Lyman-α fraction at higher redshift is consistent with other published studies. This attenuation in the Lyman-α fraction can be attributed either to physical evolution of the galaxies or, more likely, an increase in the neutral fraction of hydrogen at $z > 7$, i.e. these observations can most likely be interpreted as implying that the neutral fraction at $z \sim 8$ can be ruled out as being $\chi_{HI} = 0$ at a level of $1\,\sigma$. Larger-number statistics are required to confirm this hypothesis at a higher level of

Object	Redshift	Mag (Y_{AB})	Lyman-α flux (erg cm^{-2}s^{-1})	EW / Å	GNIRS σ	XSHOOTER σ
ERS 8496	6.441 ± 0.002	$J_{125} = 27.3$	$0.91 \pm 1.4 \times 10^{-17}$	69 ± 10	1.52	6.5
A1703_zD6	7.045	$J_{125} = 25.8$	$2.84 \pm 5.3 \times 10^{-17}$	65 ± 12	18.93	16.7
BDF-521	7.008 ± 0.002	25.86	$1.6 \pm 0.16 \times 10^{-17}$	64^{+10}_{-9}	6.67	5.93
BDF-3299	7.109 ± 0.002	26.15	$1.2 \pm 0.14 \times 10^{-17}$	50^{+11}_{-8}	4.80	2.00
GN-108036	7.213	25.50	2.5×10^{-17}	33	5.00	3.57
SDF-63544	6.965	25.10	2.8×10^{-17}	43	8.62	5.19
SDF-46975	6.844	25.20	2.7×10^{-17}	43	7.20	13.50
NTTDF-6345	6.701	25.46	0.72×10^{-17}	15 ± 3	0.48	2.4
NTTDF-474	6.623	26.50	0.32×10^{-17}	16 ± 5	0.64	1.78

Table 3.4: This table shows the significance levels at which objects discussed in literature would have been detected in our spectroscopy if they had been targetted with Gemini/GNIRS or VLT/XSHOOTER.

significance. To this end, spectroscopy was undertaken on a large sample of z-band and Y-band dropouts with VLT/FORS2; the results of that spectroscopy is discussed in detail in the next Chapter.

3.9 HUDF.YD3 - a galaxy lying at $z = 8.55$?

There has only been one recent claim of line emission beyond z $\approx$ 7.1, despite the large number of Lyman-break candidates now known at these redshifts. Lehnert et al. (2010) presented a VLT/SINFONI spectrum of one of the brightest Y-drops in the WFC3 imaging of the Hubble Ultra Deep Field, which had previously been independently selected on the basis of its broad-band ACS and WFC3 photometry by three independent groups (the galaxy HUDF.YD3 in the catalogue of Bunker et al. 2010, object 1721 in McLure et al. 2010[7], and galaxy UDFy-38135539 in Bouwens et al. 2010[8]). The Lehnert et al. (2010) spectrum shows a 6σ line at 11616Å which is consistent with being Lyman-α emission at z = 8.55, close to the photometric redshift of z = 8.45 from McLure et al. (2010). If real, the emergence of Lyman-α emission well within the Gunn-Peterson epoch would have significant implications for the size of H II regions around galaxies, and would mean that Lyman-α might still be a useful redshift indicator for very distant galaxies even at a time when most of the Universe is optically thick to this line. However, previous claims of Lyman-α emission at a similarly large redshift (e.g. Pelló et al., 2004, Chen et al., 1999) have not survived critical re-analysis (e.g. Bremer et al., 2004, Weatherley et al., 2004, Stern et al., 2000). The galaxy HUDF.YD3 from (Bunker-2010) was re-observed for this thesis with VLT/XSHOOTER and Subaru/MOIRCS spectroscopy to see if the detection of Lyman-α at z = 8.55 made by Lehnert et al. (2010) can be repeated.

[7]The naming of this galaxy changes to HUDF 2003 in McLure et al. (2011).

[8]Note that in a subsequent paper (Bouwens et al. 2011), this galaxy has a different identification number, UDFy-38125539.

Object	z-Range spanned by data (for Ly-α)	Frac$_z$	Median EW	Frac$_{\mathrm{EW<50\AA}}$	Frac$_{\mathrm{EW<75\AA}}$	Frac$_{\mathrm{EW<120\AA}}$
zD1	5.82 - 6.40	0.01	54.69	0	0.4583	1.0000
	6.08 - 6.74	0.24	243.2	0	0	0
	6.79 - 7.45	0.50	29.35	0.8349	0.9415	0.9990
	7.25 - 8.05	0.36	85.29	0	0.3326	0.6299
zD2	6.09 - 6.73	0.24	113.5	0	0	0.7697
	7.25 - 8.00	0.33	76.10	0.285052	0.4109	0.6883
zD3	6.09 - 6.73	0.24	120.4	0	0	0.7262
	7.25 - 8.00	0.33	80.72	0	0.3601	0.6413
zD4	6.09 - 6.73	0.24	150.2	0	0	0.1869
	7.25 - 8.00	0.33	100.8	0	0.0689	0.5326
P34.z.4809	3.60 - 7.40 (Optical Channel)	0.70	19.45	0.8268	0.9188	0.9856
P34.z.4809	7.42 - 19.40 (NIR Channel)	0.30	35.21	0.8191	1.2917	1.7287
ERS.YD2	7.42 - 19.40 (NIR Channel)	0.86	67.19	0.6529	1.1551	1.4293
HUDF.YD3	7.42 - 19.40 (NIR Channel)	0.98	241.6	0.0550	0.1881	0.6516
UDF092y-03751196d	7.42 - 19.40	0.996	28.64	0.8400	0.9374	0.9872

Table 3.5: This table for all objects targeted by our spectroscopy shows the redshift range spanned by our data for Lyman-α in Column 2. Column 3 shows the fractional probability that a galaxy drawn from the dropout sample would fall within the spectral coverage of that particular spectrograph setup. Column 4 gives the median EW for each object for the most probable redshift range (see Figure 3.28). The remaining three columns tabulate the fraction of our spectroscopy that has EW limits lower than our chosen threshold (50 Å, 75 Å and 120 Å respectively.) The figures in this table are for an unresolved line.

	Average Redshift	$N_{\text{eff}} = \sum \text{Frac}_z \times \text{Frac}_{\text{EW<thres}}$		
		$\text{EW}_{\text{thres}} = 50$ Å	$\text{EW}_{\text{thres}} = 75$ Å	$\text{EW}_{\text{thres}} = 120$ Å
z-drops	7.0	1.242	1.903	2.963
Y-drops	8.5	1.452	2.111	2.851
z-drops & Y-drops	7.8	2.694	4.014	5.814

Table 3.6: This table shows the total effective number of sampled galaxies with an EW upper limit lower than a set threshold. These figures are presented separately for z-drops, Y-drops and both z-drops and Y-drops combined. The figures in this table are for an unresolved line.

Object	z-Range spanned by data (for Ly-α)	Frac$_z$	Median EW	Frac$_{\mathrm{EW<50\AA}}$	Frac$_{\mathrm{EW<75\AA}}$	Frac$_{\mathrm{EW<120\AA}}$
zD1	5.82 - 6.40	0.01	107.4	0	0	0
	6.08 - 6.74	0.24	476.2	0	0	0
	6.79 - 7.45	0.50	69.38	0.1958	0.5460	0.8672
	7.25 - 8.05	0.36	167.3	0	0	0.1016
zD2	6.09 - 6.73	0.24	222.5	0	0	0
	7.25 - 8.00	0.33	149.3	0	0	0.2177
zD3	6.09 - 6.73	0.24	235.9	0	0	0
	7.25 - 8.00	0.33	158.4	0	01	0.1062
zD4	6.09 - 6.73	0.24	294.4	0	0	0
	7.25 - 8.00	0.33	197.7	0	0	0
P34.z.4809	3.60 - 7.40 (Optical Channel)	0.70	38.87	0.5759	0.6811	0.8617
P34.z.4809	7.42 - 19.40 (NIR Channel)	0.30	58.65	0.2650	0.7361	1.2627
ERS.YD2	7.42 - 19.40 (NIR Channel)	0.86	112.4	0.1583	0.4344	1.0600
HUDF.YD3	7.42 - 19.40 (NIR Channel)	0.98	400.3	0	0	0.0431
UDF092y-03751196d	7.42 - 19.40	0.996	50.63	0.5331	0.7838	0.9181

Table 3.7: This table for all objects targeted by our spectroscopy shows the redshift range spanned by our data for Lyman-α in Column 2. Column 3 shows the fractional probability that a galaxy drawn from the dropout sample would fall within the spectral coverage of that particular spectrograph setup. Column 4 gives the median EW for each object for the most probable redshift range (see Figure 3.28). The remaining three columns tabulate the fraction of our spectroscopy that has EW limits lower than our chosen threshold (50 Å, 75 Å and 120 Å respectively.) The figures in this table are for a 200km/s line.

	Average Redshift	$N_{\rm eff} = \sum \mathrm{Frac}_z \times \mathrm{Frac}_{\rm EW<thres}$		
		$\mathrm{EW}_{\rm thres} = 50\,$Å	$\mathrm{EW}_{\rm thres} = 75\,$Å	$\mathrm{EW}_{\rm thres} = 120\,$Å
z-drops	7.0	0.581	0.971	1.559
Y-drops	8.5	0.667	1.154	1.868
z-drops & Y-drops	7.8	1.248	2.125	3.427

Table 3.8: This table shows the total effective number of sampled galaxies with an EW upper limit lower than a set threshold. These figures are presented separately for z-drops, Y-drops and both z-drops and Y-drops combined. The figures in this table are for a 200km/s line.

3.9.1 Observations with VLT/XSHOOTER

The Y-band drop-out high-redshift galaxy candidate HUDF.YD3 was observed using the XSHOOTER spectrograph (D'Odorico et al., 2006) on the ESO VLT-UT2 (Kueyen) as part of programme 086.A-0968(B) (PI: A. Bunker). Here the attention is focused on the near-infrared spectroscopy around 1.12 μm, at the location of the emission line claimed by Lehnert et al. (2010) in their ESO/VLT SINFONI spectroscopy, potentially Lyman-α at z=8.55.

The main target, HUDF.YD3, has a position RA=03:32:38.135, Dec.= −27:45:54.03 (J2000), with coordinates from Lorenzoni et al. (2011). The position angle of the 11″-long XSHOOTER slit was set to 54.0 degrees East of North. The central coordinates were set to be RA=03:32:38.086, Dec.=−27:45:54.71 (J2000), such that HUDF.YD3 lay 1″ away along the slit long axis. The observations were dithered in an ABBA sequence at positions +3″ and −3″ from the central coordinates along the slit long axis (i.e. a 'chop' size of 6″), so that the expected position of HUDF.YD3 should be +4″ above the slit centre in the 'A' position, and −2″ in the 'B' position. To acquire the target, the telescope first peaked-up on a bright star 76.1″ East and 10.6″ South of the desired central pointing, then did a blind offset. Such an offset should be accurate to $< 0\farcs5$, less than half of the slit width used ($1\farcs2$) – it should be noted that our blind offset of $1\farcm3$ is less than that of $1\farcm5$ used by Lehnert et al. (2010). The XSHOOTER slit width is also much greater than the limit of $< 0\farcs4$ set on any positional offset between the continuum position and that of the claimed line emission from Lehnert et al. (2010).

The XSHOOTER observations were conducted in 6 observing blocks, each of 1 hour duration (49 min of which was on-source) and consisting of a single ABBA sequence with three exposures of the near-IR arm of duration 245 s at each A or B position. The observations were taken on the nights of UT 2010 December 27, 29, 30 & 31, with two observing blocks taken on the nights of UT 2010 December 29

& 30 and single observing blocks on the other nights. Observing conditions were reported to be clear, and the seeing conditions were typically $0\farcs5 - 0\farcs6$ FWHM (from DIMM measurements taken at the time, and this was checked to be consistent with observations of standard stars taken close in time to our observations). One of the two observing blocks taken on UT 2010 December 30 had significantly worse seeing of $1\farcs2$ FWHM, and the full dataset was reduced twice, with and without this bad-seeing block. This did not appear to have a significant impact on the final results. Our total on-source exposure time for HUDF.YD3 with XSHOOTER was 4.9 hours, with 4.1 hours taken in good seeing conditions of $0\farcs5 - 0\farcs6$.

From unblended spectral lines in the calibration arc lamp spectra and in the sky spectra, a spectral resolution of $R = \lambda/\Delta\lambda_{\rm FWHM} = 5000$ was measured. Our arc and sky lines fill the slit, so for compact sources which do not fill the slit in the good seeing the resolution will be better than this (this is expected to be the case for HUDF.YD3).

The XSHOOTER spectroscopy was reduced in two different ways. Initially the ESO pipeline (Modigliani et al., 2010) was used, which utlized the two-dimensional arc spectra through a pinhole mask to rectify the spectra both spatially and spectrally (the echelle spectra exhibited significant spatial curvature and a non-linear wavelength scale), mapping on to a final output spectral scale of $1\,\text{Å}\,\text{pix}^{-1}$ (from an original scale of about $0.5\,\text{Å}\,\text{pix}^{-1}$ at wavelengths close to 11616 Å), and a spatial scale of $0\farcs21$ (from an original scale of $0\farcs24$). The pipeline applied a flat-field, identified and masked cosmic ray strikes using the algorithm of van Dokkum (2001), differenced the two dither positions to remove the sky to first order, and combined the different echelle orders together into a continuous spectrum (taking into account the different throughputs in different overlapping echelle orders) before spatially registering and combining the data taken at the two dither positions, and removing any residual sky background.

It should be noted that the ESO pipeline interpolates the data onto a uniform grid, which has the effect of correlating the noise (making the measured noise an underestimate of the true noise), and also potentially spreading the effect of cosmic ray strikes and hot pixels around neighbouring pixels. Hence, an independent reduction of the XSHOOTER spectroscopy was also carried out, where the data were not interpolated, keeping each pixel statistically independent. The data were flat-fielded using halogen lamp spectra (that had been normalized by division by the spectral shape of the lamp), and multiple exposures at each dither position were averaged using the IRAF task `imcombine`, using a Poisson noise model to reject cosmic ray strikes. The the two dither positions were then combined, with known hot pixels masked. The measured noise in the reduced two-dimensional spectrum was close to the expected Poisson noise from the sky background, dark current and readout noise, and when combining several exposures the noise (normalized to unit time) decreased as $\sqrt{\mathrm{time}}$ as expected. The wavelength and spatial position of each pixel in the two-dimensional spectrum was determined from the sky lines in the actual data and the arc line calibration spectra taken through a pinhole mask. The spectrograph setup seemed very stable between different nights of observation, with shifts of only ≈ 0.2 pixels between nights. Residual skyline emission was removed using the `background` task in IRAF. The expected position of Lyman-α at $z = 8.55$ appears at the red end of order 23 (and at the blue end of order 22, but the throughput here is lower). The pipeline optimally combines the orders of the echelle spectrum, but in our independent reduction both echelle orders were inspected independently. The depths quoted in Section 3.9.1 come from the deepest spectrum, order 23.

A flux calibration was obtained from observations of spectrophotometric standard stars taken over UT 2010 December 26–31, around the dates when our HUDF.YD3 spectra were obtained. Our flux calibration is based on observations of the standard star LTT 3218 on UT 2010 December 28 taken in good seeing of $0\farcs6$, which is a

close match to the seeing in our spectroscopy of HUDF.YD3. The shape of the spectral response was checked to be similar on other nights where the flux standards LTT 3218 and Feige 110 were taken in worse seeing. It should be noted here that although the region of interest around 11616 Å is close to atmospheric absorption features, the depth of the absorption at this wavelength was not great and was stable night-to-night. Around our wavelength of interest, 1 count in a single 245 s integration corresponds to a line flux of 3.4×10^{-19} erg cm^{-2} s^{-1}.

3.9.2 Upper Limits on the Lyman-α Flux at $z = 8.55$ from VLT/XSHOOTER

The observed flux at the location of HUDF.YD3 in the XSHOOTER long-slit spectrum was measured, 1 arcsec above (North-East of) the slit centre, and at the expected wavelength of Lyman-α from Lehnert et al. (2010), $\lambda_{vac} = 11615.6$ Å ($\lambda_{air} = 11612.4$ Å). No sign of an emission at this location is detected. Spectrophotometry was performed using a square aperture, of extent 5 Å (10 pixels across in the wavelength domain for our own reduction of the data, and 5 pixels in the pipeline reduction), which is more than twice as large as the width of a spectrally unresolved line. For the spatial extent of our aperture, 3 pixels (0.″72) are adopted for our reduction, and 4 pixels (0.″84) for the pipeline reduction (the XSHOOTER pipeline resamples the original pixel scale slightly), which is marginally larger than the size of the seeing disk. Hence in our reduction, where the pixels are unresampled, the total flux is measured in 30 independent pixels, and from the pipeline data (which involves interpolation) the flux is measured over 20 pixels.

No significant line emission is detected – the flux in our aperture is measured to be $(-0.45 \pm 1.2) \times 10^{-18}$ ergs cm^{-2} s^{-1}, where the error is the measured 1 σ noise. The aperture was also moved by ± 2 pixels in x and y in a 3×3 grid to bracket the maximum uncertainty in the position of the Lehnert et al. (2010) Lyman-α emission ($< 0.''4$),

and no detection of line emission at any of these locations is made. Our measured noise is consistent with the online ESO Exposure Time Calculator for XSHOOTER. The Lehnert et al. (2010) line flux would be detected at the $5\,\sigma$ level if all the line emission fell within our aperture. In order to quantify the expected flux, corrected for aperture losses, artificial emission lines were created to add in at this spatial and spectral location, as shown in Figure 3.29. From the HST/WFC3 imaging, HUDF.YD3 should be unresolved in our 0.″5-0.″6 FWHM seeing. While it is conceivable that resonantly-scattered Lyman-α line emission may come from a larger halo than the stellar UV continuum (e.g., Bunker, Moustakas, and Davis, 2000, Steidel et al., 2011), the emission line reported in HUDF.YD3 by Lehnert et al. (2010) is compact spatially (unresolved in their 0.″6 seeing). Hence, a Gaussian profile is adopted for the spatial extent with a FWHM of 0.″6. For the spectral direction, a Gaussian profile is also adopted for the fake sources, and two scenarios for the velocity width are considered. The emission line in Lehnert et al. (2010) is unresolved or marginally resolved (with a FWHM of 9.2 Å, only $1\,\sigma$ larger than the resolution of SINFONI which has $R = 1580$). Our first scenario has the source spectrally unresolved by XSHOOTER, which has a higher resolving power of $R = 5000$ (so $\Delta\lambda_{FWHM} = 2.3$ Å). In this case, our photometric aperture would capture 87 per cent of the line flux, and one would expect a line with the same total flux as in the Lehnert et al. (2010) to be detected at $4.5\,\sigma$. The second scenario takes the reported (marginally-resolved) spectral width of 9.2 Å from Lehnert et al. (2010), deconvolves this with the SINFONI resolution to obtain an intrinsic line width of 5.5 Å FWHM ($140\,\mathrm{km\,s^{-1}}$), then convolve this with our spectral resolution for XSHOOTER to obtain an observed line width of 6 Å FWHM. For this broader line, our photometric aperture captures 66 per cent of the line flux, and one would expect a line with the same total flux as in the Lehnert et al. (2010) to be detected at $3.5\,\sigma$. Our XSHOOTER spectroscopy appears to rule out the existence of the Lyman-α line reported by Lehnert et al. (2010) at the $3.5 - 4.5\,\sigma$

level, depending on the velocity width of the line.

3.9.3 Observations with Subaru/MOIRCS

HUDF.YD3 was observed using the Multi-Object InfraRed Camera and Spectrograph (MOIRCS) (Suzuki et al., 2008; Ichikawa et al., 2006) on Subaru. MOIRCS provides wide-field imaging and long-slit / multi-object (MOS) spectroscopic capabilities in the $0.9 \sim 2.5$ μm spectral range under the natural seeing conditions. MOIRCS has a $4' \times 7'$ field of view (although there is vignetting beyond a diameter of $6'$ from the field centre) which is covered by two Hawaii-2 2048×2048 arrays. MOIRCS was used in slitmask mode to observe HUDF.YD3 with a slit that was $4\farcs5$ in length, with the long axis of the slit (the Position Angle of the mask) set to +57 degrees East of North. Individual integrations of 1200 s were obtained, moving the telescope along the slit axis by a small dither size of $2\farcs0$–$2\farcs5$ in an ABABAB sequence to enable background subtraction. The HUDF mask was observed on U.T. 2010 October 21 & 22, with a slit width of $1\farcs0$, and using the zJ500 grism. This instrument set-up has a spatial scale of $0\farcs117\,\mathrm{pix}^{-1}$ and a spectral scale of $5.57\,\text{Å}\,\mathrm{pix}^{-1}$. The resolving power for objects which fill the slit is $R = \lambda/\Delta\lambda_{FWHM} = 300$ (determined from Thorium-Argon arc lines), but the typical seeing was $0\farcs5$ FWHM so for unresolved sources (such at most of the high-redshift galaxies targetted) the resolving power is $R = 500$. On U.T. 2010 October 21, 8 exposures of 1200 s were obtained, with a dither step of $2\farcs5$ (i.e. placing the target at $+1\farcs25$ and $-1\farcs25$ above and below the slit centre). On U.T. 2010 October 22 the dither step was reduced to $2\farcs0$, given the good seeing, and another 12 exposures of 1200 s were obtained for a total integration time of 400 min (6.67 hours) in October 2010. HUDF.YD3 was observed again with Subaru/MOIRCS on U.T. 2010 December 07, obtaining 12 exposures of 1200 s (a total of 4 hours) with a dither size of $2\farcs0$. To take full advantage of the good seeing at Subaru (which again was $0\farcs5$ for the December 2010 observations) the size of the slit width was reduced

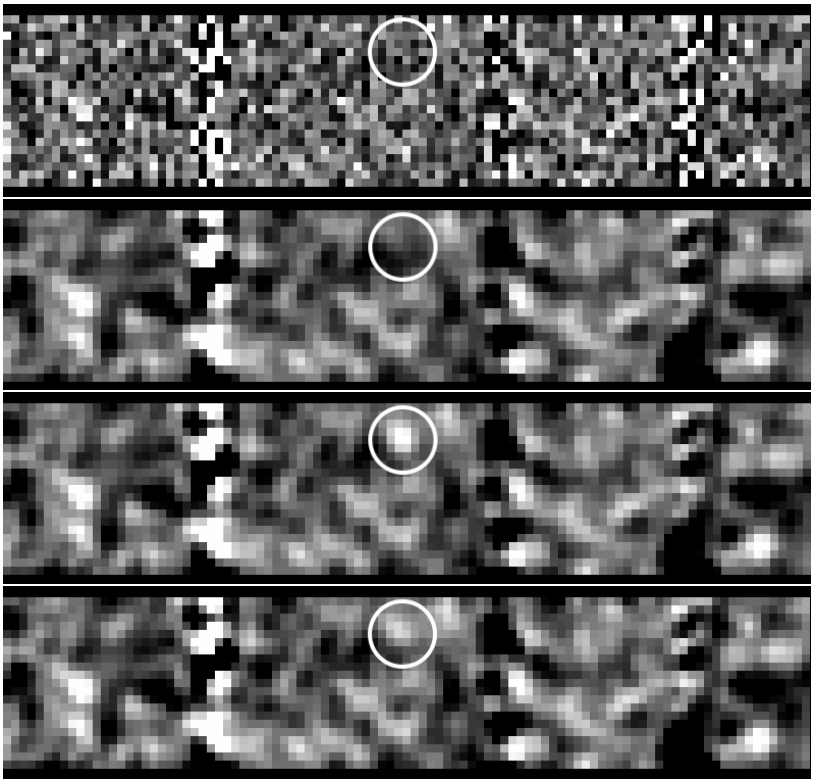

Figure 3.29: The pipeline-calibrated XSHOOTER spectrum, with the location of HUDF.YD3 (1arcsec above the centre of the long slit) and the expected wavelength of the Lyman-α emission reported by Lehnert et al. (2010) marked with a white circle. Wavelength increases from left to right, and we show the 50 Å either side of 11616 Å, and the vertical axis is the 4.4 arcsec covered in both nod positions of the XSHOOTER slit. From top to bottom: (a) the pipeline-reduced data; (b) the pipeline-reduced data convolved with a Gaussian of $\sigma = 1$ pixel (1 Å, $0''.21$). (c) a fake source with the same line flux ($6 \times 10^{-18}\,\mathrm{erg\,cm^{-2}\,s^{-1}}$) and wavelength as the Lehnert et al. (2010) line added into the frame. We assume a spatially and spectrally unresolved source, with FWHM= $0''.6$ spatially and FWHM= 2.3 Å spectrally. The resulting frame has been smoothed with a Gaussian with $\sigma = 1$ pixel. (d) a fake source with the same line flux and wavelength as the Lehnert et al. (2010) line added into the frame, with a broader FWHM= 5 Å and again unresolved spatially. The three vertical lines of higher noise are due to night sky emission lines.

to 0.″7, instead of 1.″0 used in October 2010, achieving a resolving power $R = 500$. The narrower slit reduced the sky background, while still capturing most of the flux from the unresolved galaxy, significantly improving our sensitivity at the expected Lyman-α wavelength, 11616 Å (which is close to OH sky lines).

The MOIRCS data were reduced using standard techniques in `IRAF`, treating the October 2010 and December 2010 separately due to the different slit width. The average of many dark currents was subtracted from each frame, and a flat field applied (obtained from dome flats, normalized by the spectrum of the lamp). All the data frames in the A position of the dither were then combined separately, using `ccdclip` in `imcombine` to reject cosmic rays given the parameters of the detector (gain of $3.3\,e^-\,\mathrm{count}^{-1}$ and readout noise of $29\,e^-\,\mathrm{pix}^{-1}$). The same was done for the B positions, and the combined B frame was subtracted from the combined A frame to remove the sky background to first order. This resulted in a frame where a positive signal is expected from a source at position A, and a negative signal at position B (offset along the slit by the dither step). These signals were then shifted and combined, and residual sky emission was subtracted through polynomial fits along the slit length.

Flux calibration was achieved through observation of the A0 star HIP116886, and checked against the flux of the alignment stars of known J-band magnitude seen through the 3.″5-wide alignment boxes in the data frames. Around 11616 Å (the wavelength of interest), 1 count in an individual 1200 s exposure corresponds to a line flux of $5.6 \times 10^{-20}\,\mathrm{erg\,cm^{-2}\,s^{-1}}$.

3.9.4 Upper Limits on the Lyman-α Flux at $z = 8.55$ from Subaru/MOIRCS

For the Subaru/MOIRCS data, an aperture of size 5×5 pixels was used, centred on the expected position of Lyman-α, corresponding to $0.''6 \times 28$ Å, which is slightly larger

than a resolution element. The $1\,\sigma$ noise within this aperture was measured to be $2.1\times 10^{-18}\,\mathrm{erg\,cm^{-2}\,s^{-1}}$ for the December 2010 observations, and $2.4\times10^{-18}\,\mathrm{erg\,cm^{-2}\,s^{-1}}$ for the October 2010 observations (which had higher noise due to the wider slit used and hence more sky emission). For the $0\farcs5$ seeing and a spectrally unresolved line (where the resolution is $600\,\mathrm{km\,s^{-1}}$), such an aperture encloses 68 per cent of the total flux. Hence one would expect an emission line of the flux and wavelength reported by Lehnert et al. (2010) to be present at the $2.7\,\sigma$ level in our total Subaru/MOIRCS spectrum, with most of the sensitivity coming from the December 2010 data using a narrower slit (where such a line should be present at the $2.0\,\sigma$ level). However, in both sets of MOIRCS observations this line is undetected, with a total aperture-corrected flux of $(1.6\pm3.1)\times10^{-18}\,\mathrm{erg\,cm^{-2}\,s^{-1}}$ for the deeper December 2010, and a total flux of $(-0.1\pm2.3)\times10^{-18}\,\mathrm{erg\,cm^{-2}\,s^{-1}}$ when combining all the MOIRCS observations together from all three nights (using inverse-variance weighting). Although the MOIRCS spectrum is less deep than our XSHOOTER spectrum (on account of the lower spectral resolution of MOIRCS), the MOIRCS spectrum still is useful because our confidence about the slit position is very high, at the $0\farcs1$ level, due to the number of alignment stars used to position the slitmask. For the XSHOOTER spectrum (and indeed the Lehnert et al., 2010 SINFONI spectrum) a blind offset was performed from a nearby star, which does introduce some uncertainty – although the tolerance is supposed to be less than $0\farcs4$ (the maximum positional uncertainty for the Lyman-α line given by Lehnert et al. (2010)). Both our VLT/XSHOOTER and Subaru/MOIRCS spectroscopy yield consistent results: no emission line at $\lambda_{vac} = 11615.6\,\text{Å}$ is seen at the position of HUDF.YD3, whereas if the flux reported by Lehnert et al. (2010) is accurate a signal should be detected at $3.5-4.5\,\sigma$ with XSHOOTER and $2.7\,\sigma$ with MOIRCS. Combining the results from two different spectrographs with inverse-variance weighting, the Lehnert et al. (2010) line flux is ruled out at the $5\,\sigma$ level.

3.9.5 HST Photometry

Our VLT/XSHOOTER and Subaru/MOIRCS spectroscopy of HUDF.YD3 strongly suggests that there is no line at the wavelength and line flux claimed by Lehnert et al. (2010) on the basis of their VLT/SINFONI spectroscopy. This section briefly consider whether the Lehnert et al. (2010) emission line would have been consistent with the HST/WFC 3 broad-band photometry of this object reported by several groups (Bunker et al. 2010; Bouwens et al. 2010; McLure et al. 2010; Lorenzoni et al. 2011). The WFC3 observations of the HUDF taken as part of the programme GO-11563 (PI: G. Illingworth) used the F105W ("Y-band"), F125W ("J-band") and F160W ("H-band") filters. An emission line at 11615.6Å would lie entirely within the Y-band (and also within the wide J-band), in the area of peak transmission of the sharp-sided Y-filter. If one takes the line flux of $6.1 \times 10^{-18}\,\mathrm{erg\,cm^{-2}\,s^{-1}}$, then this would be equivalent to an observed broad-band magnitude of $Y_{AB} = 28.89$. There should also be a contribution from the UV-continuum photons long-ward of Lyman-α (assuming near-total absorption by the Lyman-α forest at shorter wavelengths). Only 20 per cent of the Y-band filter transmission would lie at wavelengths above Lyman-α at the claimed redshift of $z = 8.55$ (Lehnert et al. (2010)), which would imply a broad-band magnitude from the claimed line and continuum of $Y_{AB} = 28.57$. In calculating the UV flux density the measured HST/WFC3 broad-band magnitudes of $J_{AB} = 28.18 \pm 0.13$ and $H_{AB} = 28.10 \pm 0.13$ are used (Lorenzoni et al. 2011), and a rest-UV spectral slope of $f_\lambda \propto \lambda^{-2.0}$ is adopted, consistent with the HST/WFC3 after the J-band is corrected for the small fraction of flux within this filter that would fall below Lyman-α (a correction of 0.15 mag, comparable to the measurement error). HUDF.YD3 is undetected in the deep Y-band image, which reaches a $2\,\sigma$ limiting magnitude of $Y_{AB}(2\,\sigma) = 29.65$ in a $0\farcs6$-diameter aperture. Hence the broad-band photometry in the Y-band is inconsistent with the Lehnert et al. (2010) line flux and redshift being real – if the line was real, then the deep HST/WFC3 Y-band should have obtained

a clear $5.4\,\sigma$ detection, whereas the actual result was a formal non-detection (below the $2\,\sigma$ limiting magnitude). The broad-band photometry alone seems to rule out the claimed line from Lehnert et al. (2010) at the $5\,\sigma$ level – consistency with the Lehnert et al. (2010) result would require both that the broadband flux is underestimated due to noise and that the line flux is overestimated, a coincidence which is statistically unlikely.

Chapter 4

Multi-Object spectroscopy with FORS2

4.1 Furthering the search for Lyman-α emission in the Early Universe

Following the analysis of the Gemini/GNIRS and VLT/X-Shooter data, which together comprised a fairly small sample (and limited sensitivity in the case of GNIRS), deeper observations of a large number of objects were undertaken with the FOcal Reducer and low dispersion Spectrograph (FORS2) at the Very Large Telescope in Chile. These observations were designed to target many z-band dropouts (as well as a number of i-band dropouts as "filler targets") using a multi-object mask, in order to significantly increase the sample of objects used for this project. This chapter deals with the reduction and analysis of these data.

4.2 Observations with VLT/FORS2

FORS2 is a multi mode (imaging, polarimetry, long slit and multi-object spectroscopy) optical instrument which works in the 330-1100 nm wavelength range and has a maximum field size of $6.8' \times 6.8'$ covered by a mosaic of two 2k×4k MIT CCDs (hereafter referred to as Chip 1 and Chip 2). It was used in Mask Exchange Unit (MXU) mode to observe a number of z-band and i-band dropouts. For these observations, the 600z holographic grism and OG590 order separation filter were employed; this allows one to span the 737-1070nm region. (The precise wavelength range covered for any given slit varies slightly depending on the position of the slit on the detector).

The main targets for our FORS2 observations were a number of z-band dropouts (Table 4.1) which were identified via imaging with the Hubble WFC3 camera in searches conducted by Wilkins et al. (2011), Bouwens et al. (2011), and McLure et al. (2010). The selection was geometric, satisfying the constraint that the slits must be $6''$ long and cannot overlap, with higher priority[1] targets winning, given a choice. A number of i-band dropouts was also observed (Table 4.2), 3 of which were identified by Bunker et al. (2004), 2 by Bouwens et al. (2006) in the HUDF and 11 were chosen from the Chandra Goods-South field, but in the case of i-drops the observations are very incomplete as these were intended to be filler objects. Some other lower redshift galaxies were also put on the mask (typically objects at z$\sim$1 to get [OII] 3727, H-β, and [OIII] 5007) as "filler objects" on our mask but these are not discussed in this thesis. The mask used is shown in figure 4.1.

The observations were carried out in service mode over two semesters. The first set of observations (as part of programme 086.A-0968A) was made in 2010 on October 27, 28, 29 & 30. These observations comprise 11 pairs of nodded frames, each frame having an integration time of 1400 seconds. The second set of observations (as part

[1]A target with a more reliable dropout colour and non-detection in the optical bands was given priority. In the event that two candidates ended up being assigned the same priority, the brighter target was chosen.

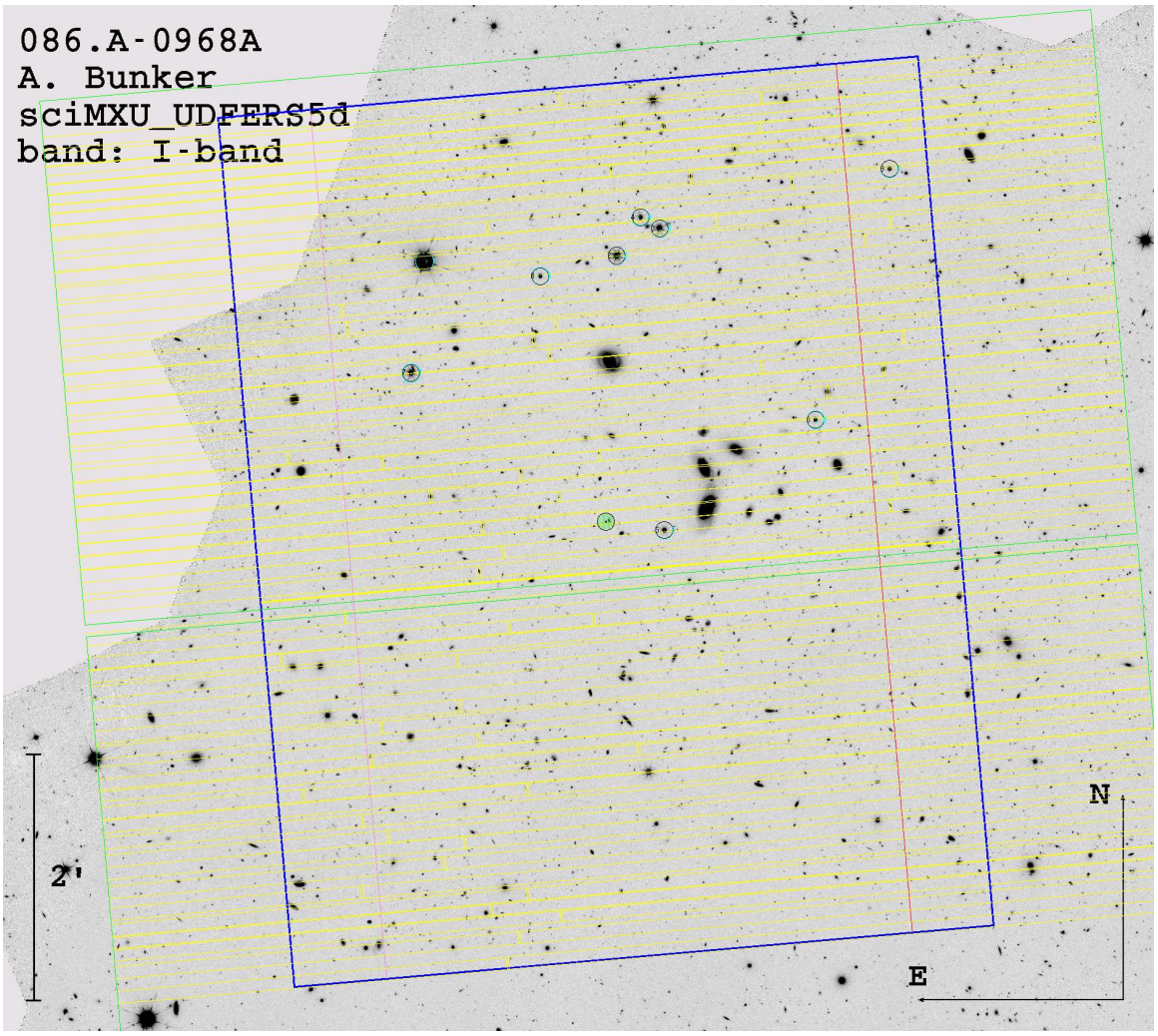

Figure 4.1: The VLT/FORS2 mask. The blue circles are alignment stars, the green filled circle marks the centre of the field, and the yellow lines represent the slits.

of programme 088.A-1013A), carried out using an identically cut mask, was made on November 08 & 16, December 03, 06, 10, 11, 14 & 16 2011 and on January 2012, and March 14, 26 & 27 2012. These observations comprise 22 pairs of nodded frames, with each frame again having an integration time of 1400 seconds. The total integration time on the science targets was 25.67 hours. An acquisition frame was first obtained to check the pointing. The observations were dithered in an ABBA sequence at positions +3" and -3" from the central coordinates along the slit long axis (i.e. a 'chop' size of 6") to enable background subtraction. The average seeing during the

observations was of 0.7″. All observations were taken at low airmass, which varied between 1.001 and 1.297, the vast majority of the frames had an airmass of about 1.0, so the effect of differential atmospheric dispersion is negligible. (Only two frames were acquired at a higher airmass; for these two frames, the airmass at the start and end of the integration varied between 1.609 - 1.818 and 1.868 - 2.176 respectively.)

The resolving power attained for these observations at a wavelength of 1μm was measured from sky emission lines to be $R = 1800$.

4.3 Reduction

The first stages of the data reduction were carried out using the ESO FORS2 pipeline[2]. In particular, the two pipeline recipes *fors_calib* and *fors_science* were used for the preparation of the calibration frames and science data respectively. In this section, we first review what the pipeline-reduction entailed, then move on to discuss the later stages of the reduction process which required custom-made procedures.

4.3.1 Preparing the calibration files with *fors_calib*

The *fors_calib* recipe was used for three main purposes:

- Identifying reference lines on our MXU arc lamp exposures to perform wavelength calibration.
- Tracing the spectral edges on the flat field exposures.
- Creating a normalized flat-field from a number of input flat-field exposures.

fors_calib requires various input files. The two main types of required calibration files are: (1) Lamp_MXU files, which are raw arc-lamp spectra used to perform wavelength-calibration (see figure 4.2), and (2) A set of raw Bias Frames which

[2]The FORS2 pipeline is available here: http://www.eso.org/sci/software/pipelines/fors/fors-pipe-recipes.html

Object	R.A. (J2000)	Dec (J2000)	J_{AB} (F125W)	M_{1600}	Wavelength Range Spanned	Chip
ERS.z.87209	03:32:29.53	-27:42:04.5	26.84	-19.8963	7373 - 10169	Chip 1
ERS.z.90192	03:32:24.08	-27:42:13.9	26.48	-20.2063	7373 - 9720	Chip 1
ERS.z.26813	03:32:22.93	-27:44:09.9	26.83	-20.2263	7373 - 9679	Chip 1
ERS.z.87326	03:32:23.15	-27:42:04.6	26.96	-19.1763	7373 - 9628	Chip 1
ERS.z.46030	03:32:22.66	-27:43:00.7	26.11	-20.9863	7373 - 9620	Chip 1
ERS.z.70546	03:32:27.90	-27:41:04.2	25.97	-20.4263	7373 - 10000	Chip 1
HUDF.z.2677	03:32:42.18	-27:46:27.9	27.7	-19.2163	8104 - 10995	Chip 2
HUDF.z.4444	03:32:42.54	-27:46:56.6	26.44	-20.5263	8155 - 10995	Chip 2
HUDF.z.6433	03:32:42.55	-27:47:31.5	27.1	-19.6363	8181 - 10995	Chip 2
HUDF.z.7462	03:32:36.76	-27:47:53.6	27.75	-19.1163	7720 - 10981	Chip 2
HUDF.z.5141	03:32:38.79	-27:47:07.2	26.9	-20.1763	7848 - 10995	Chip 2
HUDF.z.1889	03:32:41.81	-27:46:11.3	28.44	-18.0263	8062 - 10987	Chip 2
UDFy-39537174	03:32:39.52	-27:47:17.4	26.6	-20.5363	7916 - 10995	Chip 2
UDFy-44706443	03:32:44.69	-27:46:44.3	29.1	-19.8363	8340 - 10995	Chip 2
UDFy-37218061	03:32:37.21	-27:48:06.1	27.6	-19.3363	7800 - 10995	Chip 2
HUDF.z.6497	03:32:36.45	-27:47:32.4	28.31	-18.7563	7680 - 10938	Chip 2
UDFz-41597044	03:32:41.59	-27:47:04.4	28.3	-18.3363	8080 - 10990	Chip 2
M2560z	03:32:37.79	-27:47:40.4	28.87	-17.8063	7795 - 10986	Chip 2
ERSz-2432842478	03:32:43.27	-27:42:47.8	25.9	-21.1363	8083 - 10995	Chip 1
ERSz-2354442550	03:32:35.43	-27:42:55.0	26.1	-20.7363	7422 - 10692	Chip 1
ERSz-2225141173	03:32:22.50	-27:41:17.3	27.2	-19.8363	7373 - 9555	Chip 1
ERSz-2352941047	03:32:35.28	-27:41:04.7	27.6	-19.5363	7373 - 10000	Chip 1

Table 4.1: z-drops targeted with FORS2. The first 6 ERS.z. objects in this table come from Wilkins et al. (2011), as do the 6 HUDF.z. objects. The three UDFy objects were selected from Bouwens et al. (2011). HUDF.z.6497 is a lower priority object from Wilkins et al. (2011). The next two objects in the list are low priority objects listed by Bouwens et al. (2011) and McLure et al. (2010) and the last four ERSz objects are low-priority ERS sources from Bouwens et al. (2011). The absolute magnitude at 1600Å is computed assuming that the object lies at the peak of the expected redshift distribution for the z-drop selection.

Object	J_{AB} (F125W)	R.A. (J2000)	Dec. (J2000)
46574	26.71	03:32:38.28	-27:46:17.2
49117D	27.74	03:32:38.96	-27:46:00.5
42806	28.21	03:32:36.49	-27:46:41.4
HUDF-39065387	26.92	03:32:39.06	-27:45:38.7
HUDF-35237429	29.23	03:32:35.23	-27:47:42.9
CDFS-2379542076	25.80	03:32:37.95	-27:42:07.6
CDFS-2452643595	26.08	03:32:45.26	-27:43:59.5
CDFS-2278843156	26.19	03:32:27.88	-27:43:15.6
CDFS-2294145379	26.35	03:32:29.41	-27:45:37.9
CDFS-2340645186	26.87	03:32:34.06	-27:45:18.6
CDFS-2323746215	26.92	03:32:32.37	-27:46:21.5
CDFS-2431845175	26.92	03:32:43.18	-27:45:17.5
CDFS-2373844457	26.98	03:32:37.38	-27:44:45.7
CDFS-2455245382	27.13	03:32:45.52	-27:45:38.2
CDFS-2418044023	27.23	03:32:41.80	-27:44:02.3
CDFS-2279641190	27.41	03:32:27.96	-27:41:19.0

Table 4.2: i-drops targeted with FORS2. The first three objects are from Bunker et al. (2004) and the rest are from Bouwens et al. (2011).

are used to create a median master bias frame. Additionally, the recipe was supplied with three further file-types: (1) A GRISM_TABLE provided with the pipeline which contains a number of parameters controlling the extraction of spectra for a given grism, (2) A MASTER_LINECAT file, which is a master line catalog containing reference wavelengths in Angstrom for the arc lamp, and (3) A number of SCREEN_FLAT_MXU files (see Fig. 4.3), which are raw spectral flat exposures; these are subsequently stacked into one master flat field by *fors_calib*.

4.3.2 Reducing the science data with *fors_science*

The *fors_science* recipe was used to separately reduce each raw frame containing the science spectra (shown in Figures. 4.4 and 4.5) applying the normalized master flat-field and extraction mask created by *fors_calib*. It was also used to perform bias-subtraction and flat-fielding of the data. The flat-fielding procedure entailed dividing the bias subtracted input scientific frames by the normalised flat field frame. Addi-

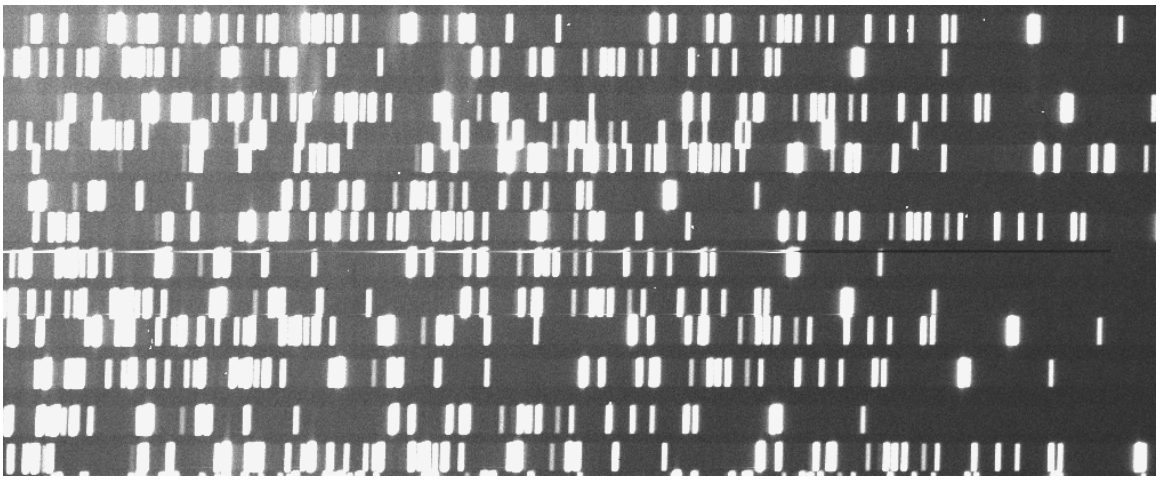

Figure 4.2: Part of a raw arc-lamp spectrum used to wavelength-calibrate the data.

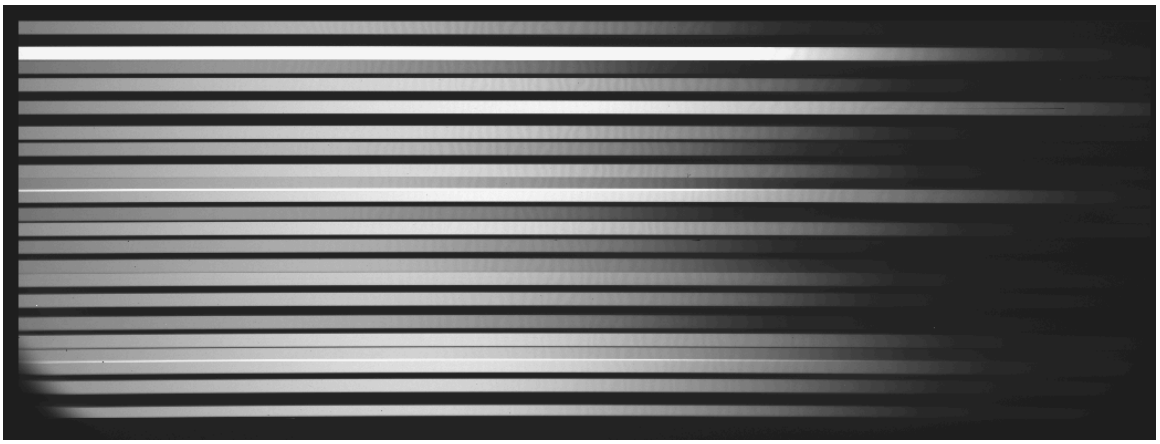

Figure 4.3: A raw FORS2 flat field (here showing Chip 2).

tionally, the raw science spectra were remapped to a spectral pixel scale of 1.63Å/pix and a spatial pixel scale of 0.25″/pix; the remapping carried out by this recipe gets rid of optical distortions, which manifest themselves in problems such as spatial curvature in the raw frames. Local sky subtraction was performed by modelling the sky for each column of pixels for each spectrum. This was done prior to resampling the data in order to minimize small-scale interpolation issues. Cosmic rays were also eliminated using this recipe.

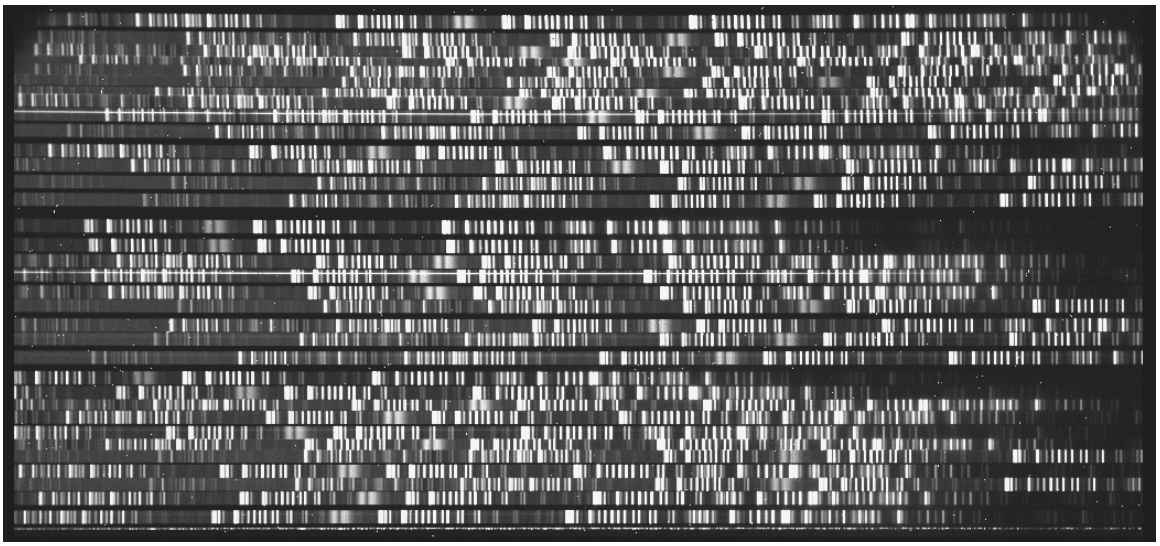

Figure 4.4: A raw FORS2 science frame (Chip 1).

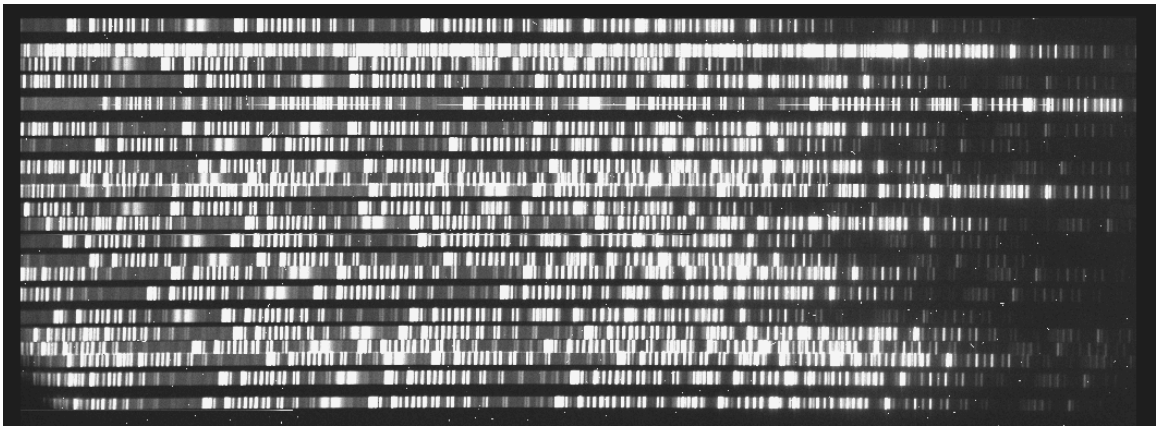

Figure 4.5: A raw FORS2 science frame (Chip 2).

4.3.3 Combining the frames

The combination of individual science frames was not carried out using the FORS2 pipeline. Instead, an algorithm was written to carry out this task. In particular, since the exact start and end y-coordinates of a given reduced spectrum in the pipeline output sometimes varied by about a pixel between frames (the pipeline introduced a padding between individual slits which was not always constant), this tailor-made algorithm was used to read in and calculate the relevant information about each re-

duced spectrum (e.g. the length of the slit for that spectrum, the central y-coordinate of the slit, etc.) to cut each spectrum correctly and enable the combination of frames. The actual combination was carried out using the `IRAF` task `imcombine`, averaging over the number of frames.

4.3.4 Spectro-photometric calibration

One of the slits of our mask was placed on an M4III-star (EIS J033236.27-274302.7 with coordinates R.A. 03:32:36.252, Dec -27:43:02.50 in the Simbad catalog) and observations of this star were used to flux-calibrate our data. Comparing the observed spectrum of this star against a theoretical spectrum of an M4III star, the instrument efficiency was derived (see Fig. 4.6) as well as a flux calibration curve (see Fig. 4.7). To obtain our flux calibration curve, the following equation was used:

$$\text{Flux Calibration Curve} = \frac{F \times \text{Theoretical Spectrum of M4III star}}{\text{Filt. Cor.} \times \text{Measured Counts}} \tag{4.1}$$

where F is the flux of star in ergs $\text{cm}^{-2}\text{s}^{-1}\text{Å}^{-1}$ converted (using the online NICMOS unit conversion form) from the AB magnitude measured in the i-band filter, and Filt. Cor. is a correction factor to account for the shape of the filter (obtained by finding the integral of the product of the theoretical spectrum with the filter transmission curve). A smooth function was then fit through the resulting curve using `IRAF`, taking into account strong atmospheric absorption by O_2 and H_2O around 0.76μm.

4.4 Results

All the 2D spectra were carefully inspected; in particular, the expected location for the target and the wavelength range around 1 micron (where Lyman-α might be expected for z-band dropouts) was rigorously examined. This was carried out by

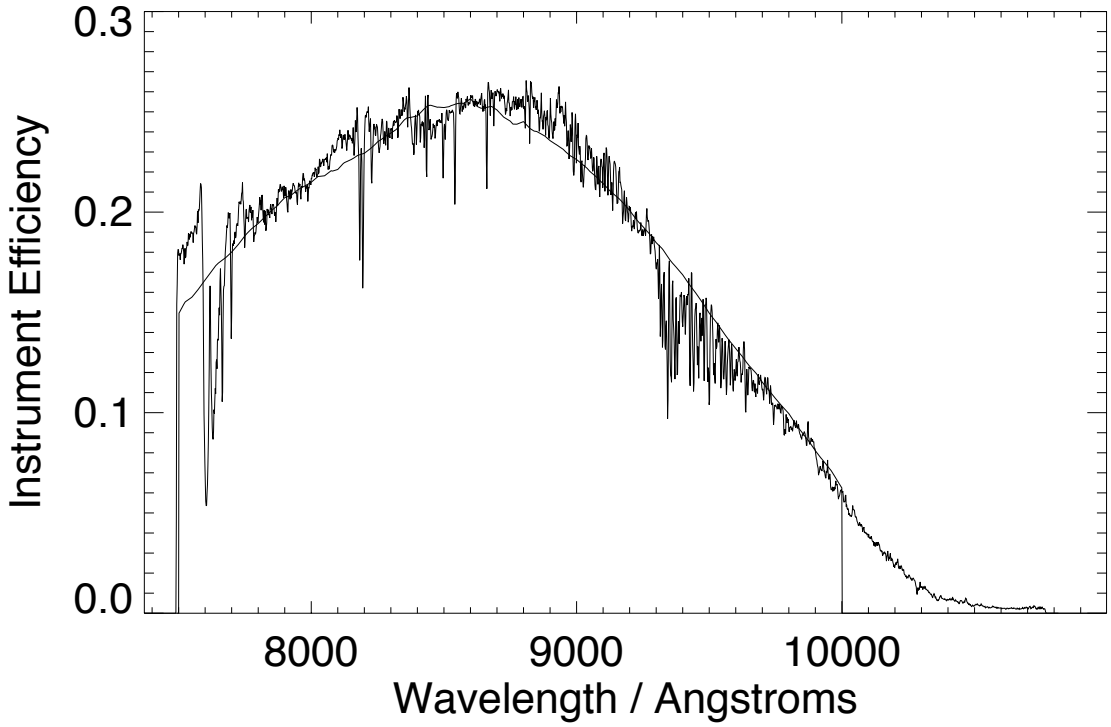

Figure 4.6: Our derived efficiency curve for FORS2 compared with that quoted by ESO (smooth curve); agreement between the two is very good.

means of visual inspection, including examining frames which had been convolved with a Gaussian with similar FWHM to the spatial seeing and spectral resolution to bring up any faint feature. A noise model, based on the Poisson counts of the sky background and dark current, the sensitivity of the detector (as a function of wavelength and position on the array) and the readout noise of the array was developed, in particular using:

$$\text{Predicted Noise (in cgs units)} = \text{Cal. Flux} \times \sqrt{W_{spec} \times W_{spat}} \times \frac{\sqrt{(\{\text{Sky+Data}\} \times t \times N \times g) + N \times (\text{R.N.} \times g)^2}}{(t \times N \times g)}$$

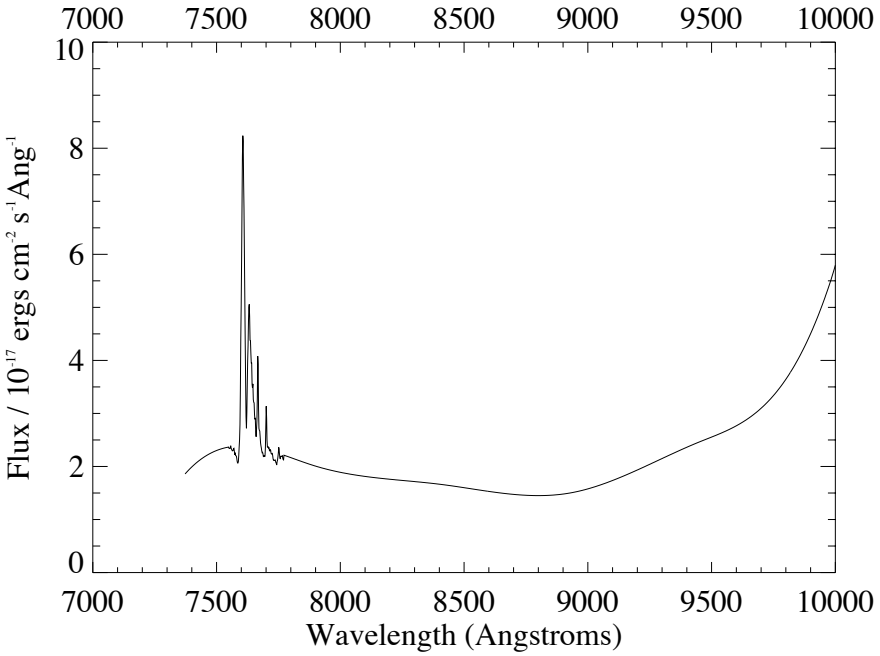

Figure 4.7: The flux calibration curve obtained for FORS2 from observations of the M4-III star EIS J033236.27-274302.7. This shows what 1 count/s/pixel corresponds to. The strong peak around 0.76μm corresponds to atmospheric absorption by O_2 and H_2O.

where Cal. Flux is the wavelength-dependent flux-calibration, W_{spec} and W_{spat} are the spectral and spatial widths of the aperture respectively, {Sky+Data} is the reduced (but not flux-calibrated) data with the sky added to it, t is the exposure time per frame, N is the total number of frames, and g and R.N. are respectively the gain and read-noise of the detector. Dividing the data by this noise model should return a standard deviation with value 1; this operation was carried out and the `IRAF` task `imexam` was used to measure the standard deviation in multiple locations on the 2D spectrum to verify that this was indeed the case. As a further check on the detectability of potential Lyman-α emission, fake sources of varying intensity profiles were added in random locations in the 2D spectra in a manner similar to that described in Chapter 3, and it was concluded that a line with an intrinsic velocity width

of 300km s^{-1} with a signal to noise ratio of 5σ would be detected in our spectroscopy using an aperture of size 1″×18Å FWHM (4×11 pixels).

Since the continuum flux for these objects can be derived from *H*ST imaging, this was used in conjunction with our deep spectroscopy to derive upper limits on the rest-frame Equivalent Widths (see Figures 4.9-4.22 which show the upper limits on the EWs for the strong candidates in our sample). As described previously for GNIRS and XSHOOTER in Chapter 3, the continuum was inferred from broad-band photometry using the filter above the Lyman-α break, in the case of our FORS2 observations using the F_{105W} Y-band for the z-drops at $z \approx 7$. Above the Lyman break, the rest-frame spectral slope was modelled using $f_\lambda \propto \lambda^\beta$, where β was taken to be -2. Since at the high redshift extreme of the expected redshift distribution, the Lyman-α break can fall within the short-wavelength side of the filter used to determine the continuum, the upper limits on the line flux were used to correct for possible Lyman-α line emission contamination of the broad-band magnitude, just as was done before for our GNIRS and XSHOOTER observations.

Since Lyman break galaxies are typically unresolved in ground-based observations, a spatial extraction aperture of 1.5 times the seeing disk was adopted. For the spectral extent, a hypothetical line was assumed to have an intrinsic velocity width of 300km s^{-1}, which after convolution with the spectral resolution of FORS2 (5.48Å) results in a line width of 11.4Å FWHM ($\sim$ 7 pixels). Hence an aperture with size 1″ × 18Å FWHM (4 × 11 pixels) was adopted. For a 300km s^{-1} line our aperture captures 93% of the flux.

In Chapter 3, particular attention was paid to HUDF.zD1, an object which had been previously observed by Fontana et al. (2010), who note a marginal detection of possible Lyman-α emission at a wavelength of 9691.5Å. If this emission line were real it would place this object at $z = 6.97$. This object was observed with Gemini/GNIRS and no emission was detected, however, as was noted in Chapter 3, our spectroscopy

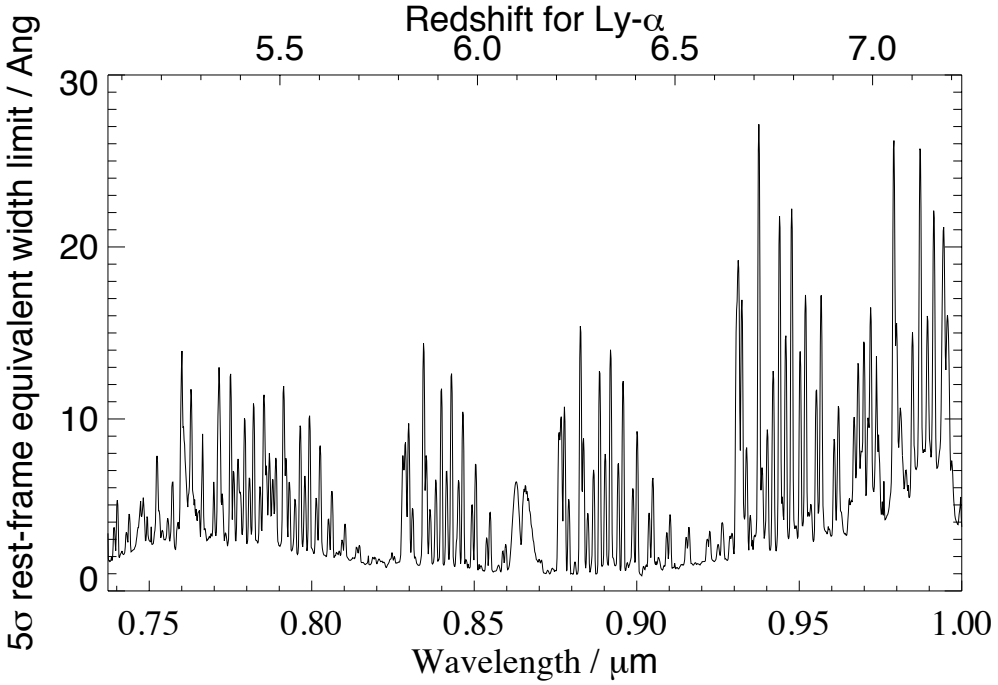

Figure 4.8: 5σ Rest-Frame Equivalent Width limits for ERS.z.70546 from FORS2 observations.

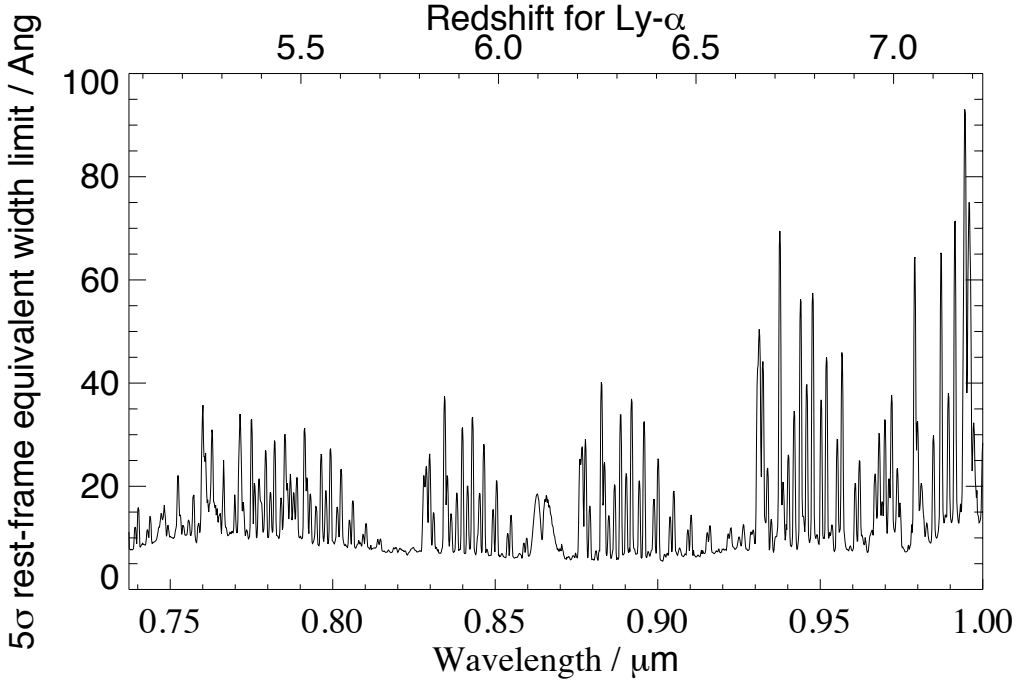

Figure 4.9: 5σ Rest-Frame Equivalent Width limits for ERS.z.87209 from FORS2 observations.

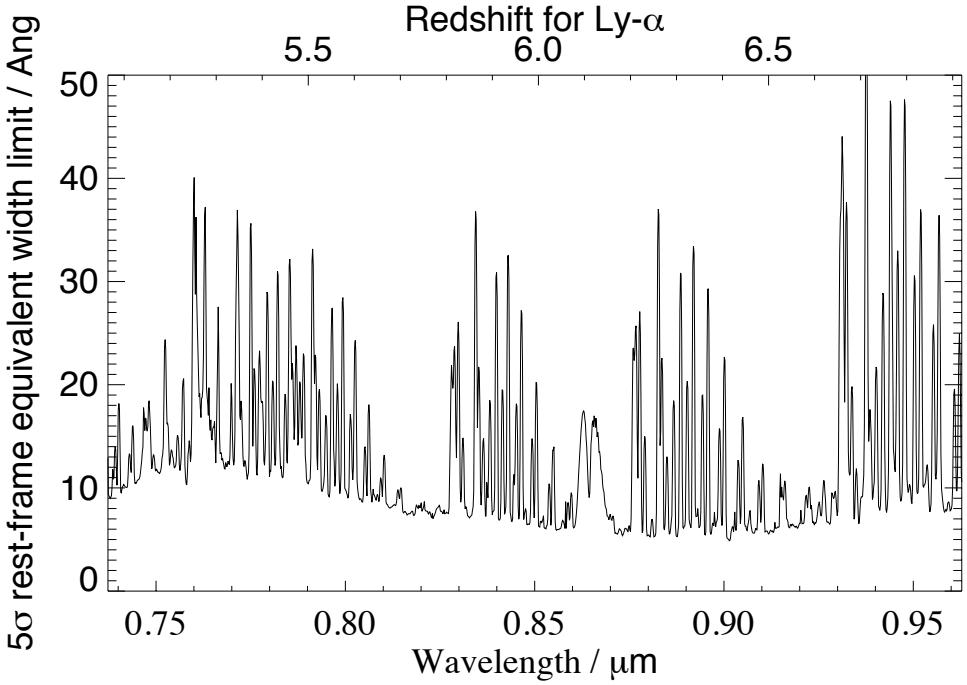

Figure 4.10: 5σ Rest-Frame Equivalent Width limits for ERS.z.87326 from FORS2 observations.

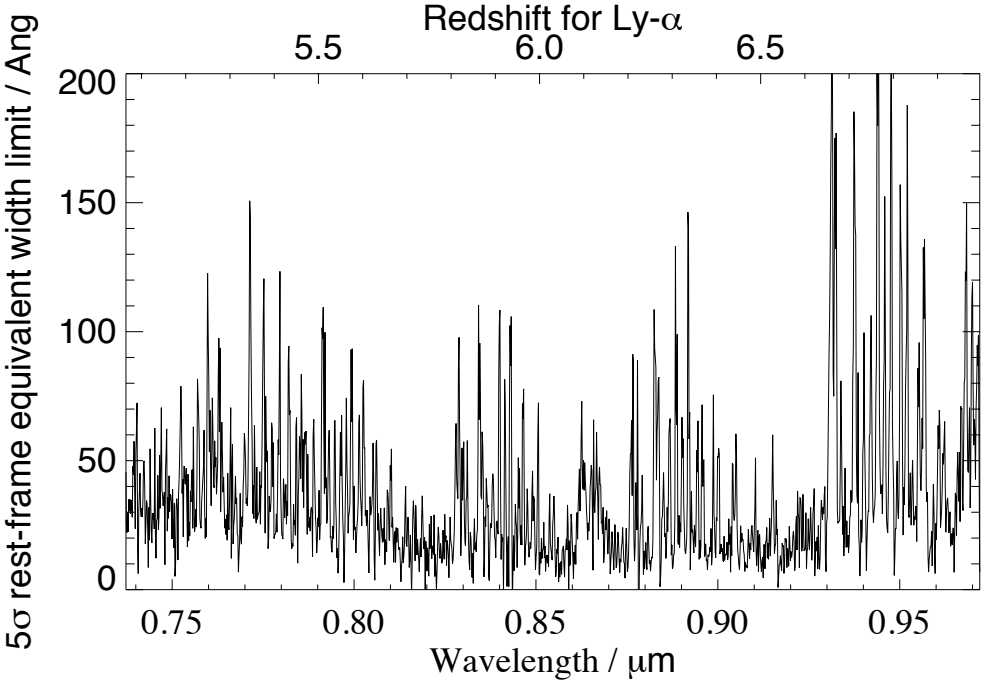

Figure 4.11: 5σ Equivalent Width limits for ERS.z.90192 from FORS2 observations.

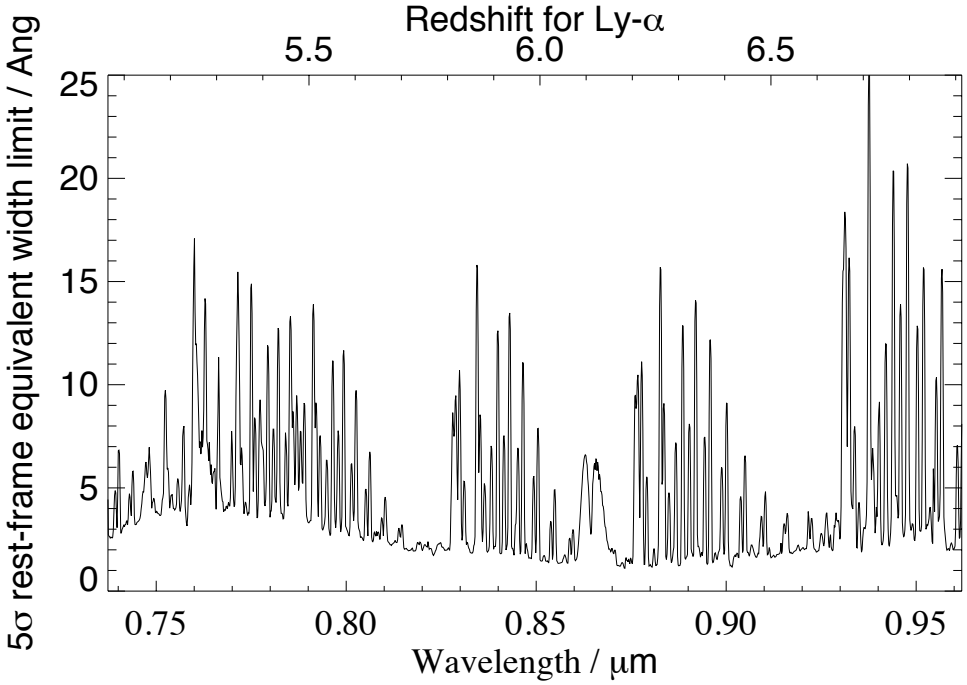

Figure 4.12: 5σ Rest-Frame Equivalent Width limits for ERS.z.46030 from FORS2 observations.

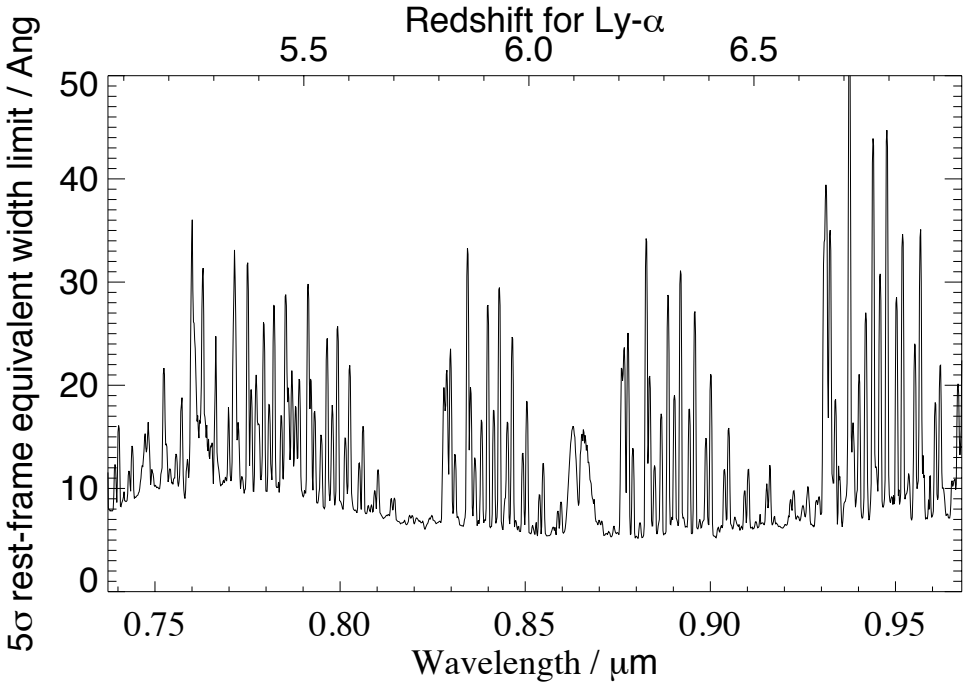

Figure 4.13: 5σ Equivalent Width limits for ERS.z.26813 from FORS2 observations.

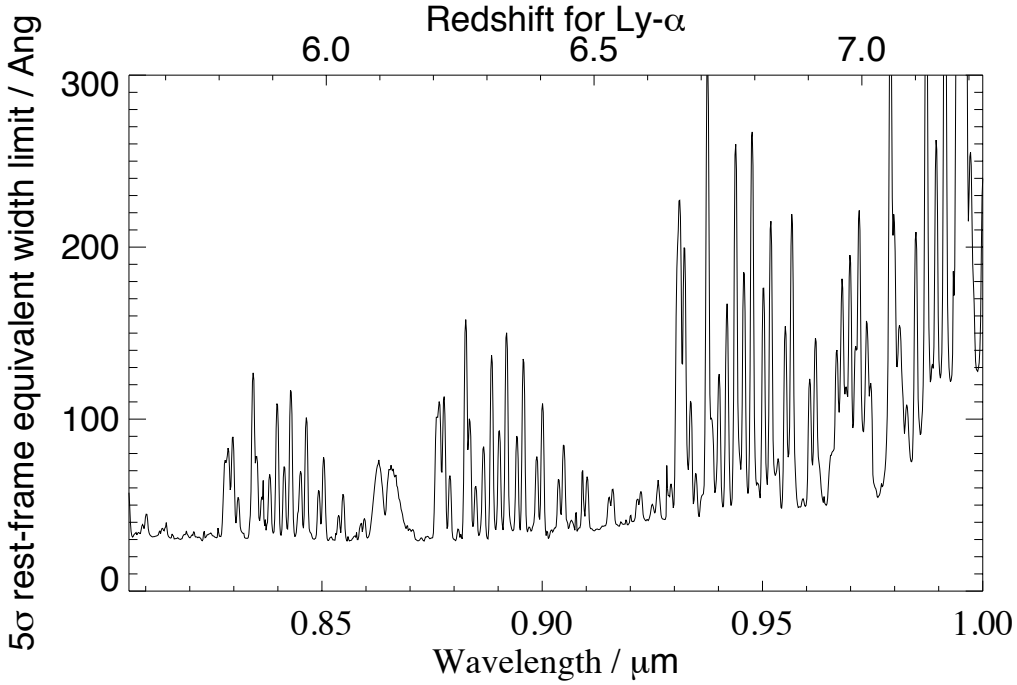

Figure 4.14: 5σ Rest-Frame Equivalent Width limits for HUDF.z.1889 from FORS2 observations.

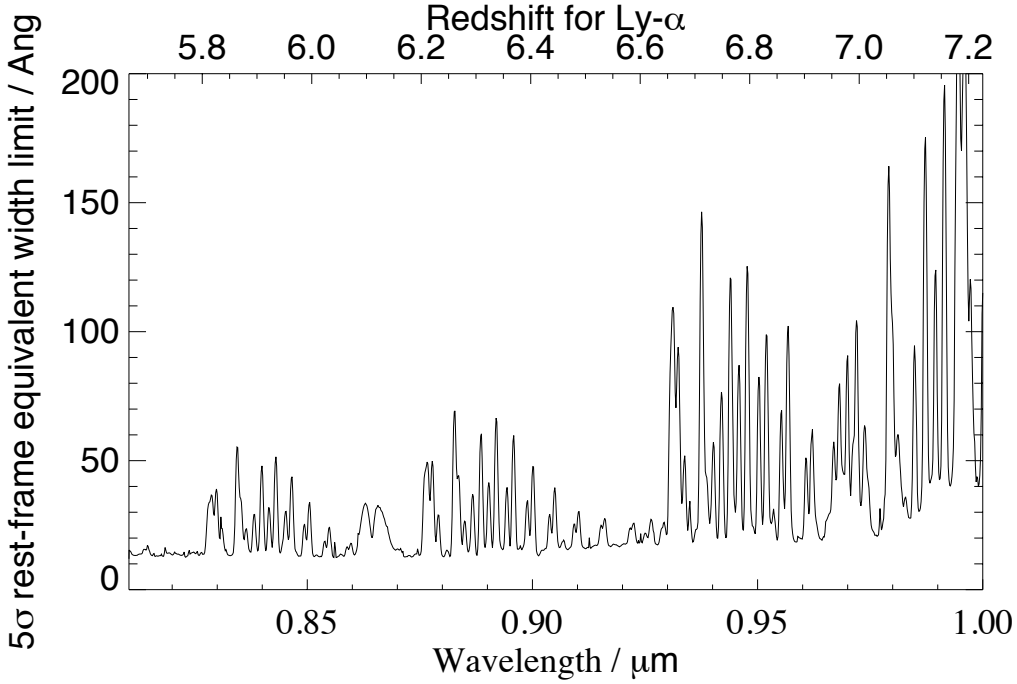

Figure 4.15: 5σ Equivalent Width limits for HUDF.z.2677 from FORS2 observations.

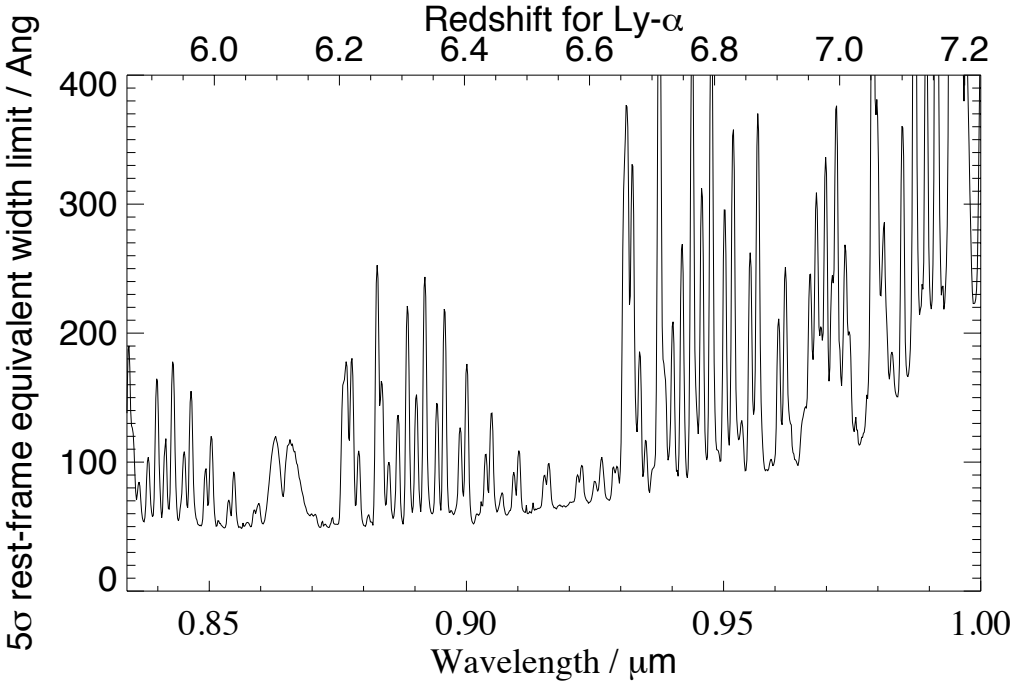

Figure 4.16: 5σ Rest-Frame Equivalent Width limits for UDFy-44706443 from FORS2 observations.

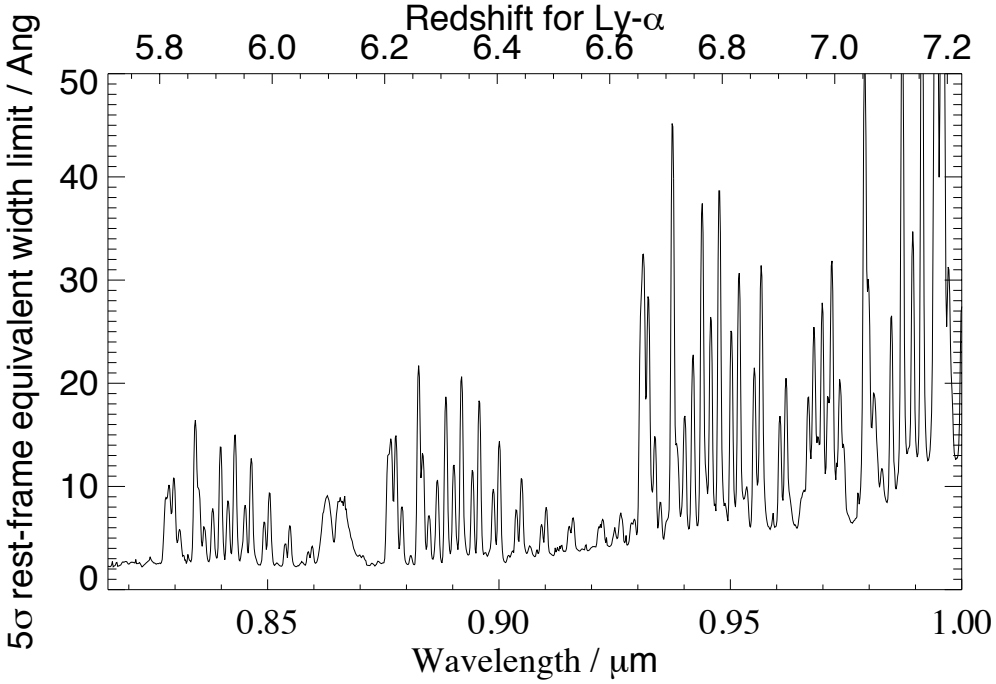

Figure 4.17: 5σ Equivalent Width limits for HUDF.z.4444 from FORS2 observations.

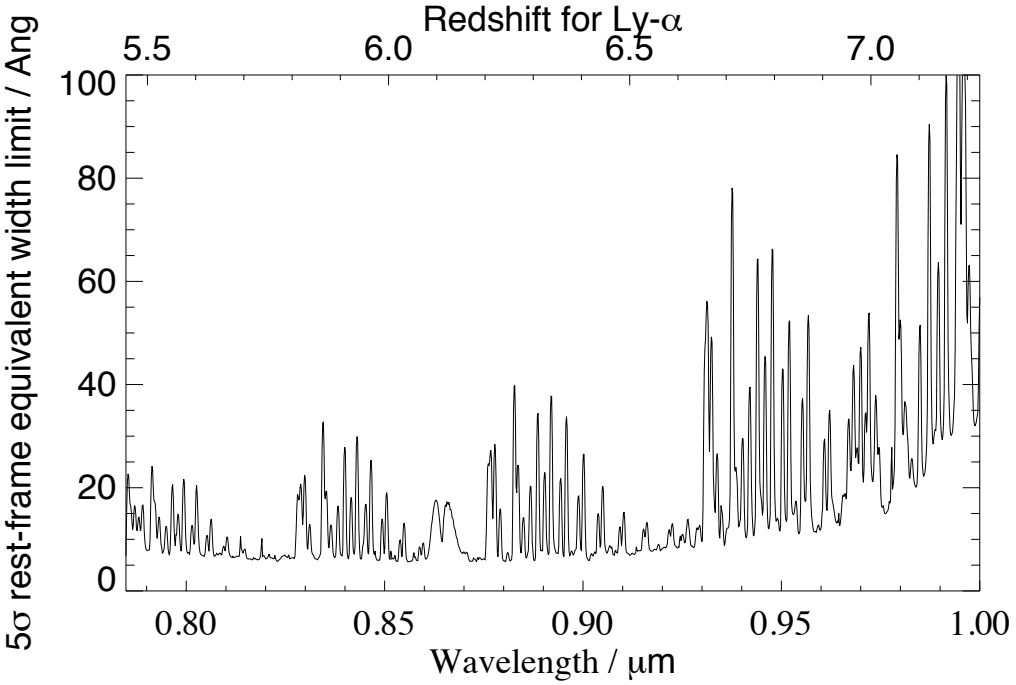

Figure 4.18: 5σ Rest-Frame Equivalent Width limits for HUDF.z.5141 from FORS2 observations.

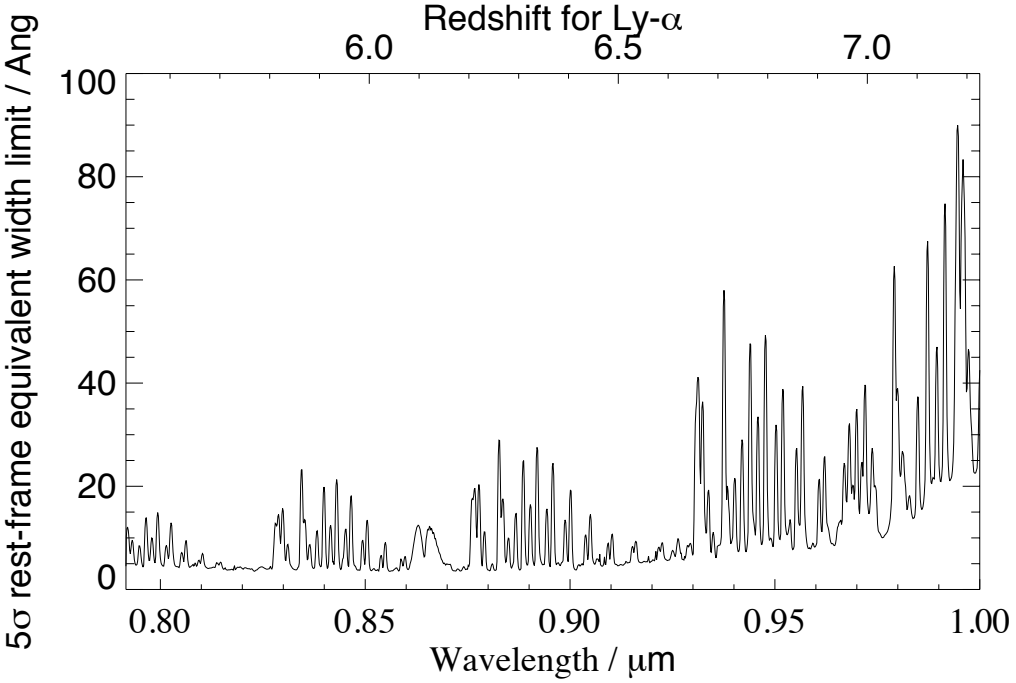

Figure 4.19: 5σ Equivalent Width limits for UDFy-39537174 from FORS2 observations.

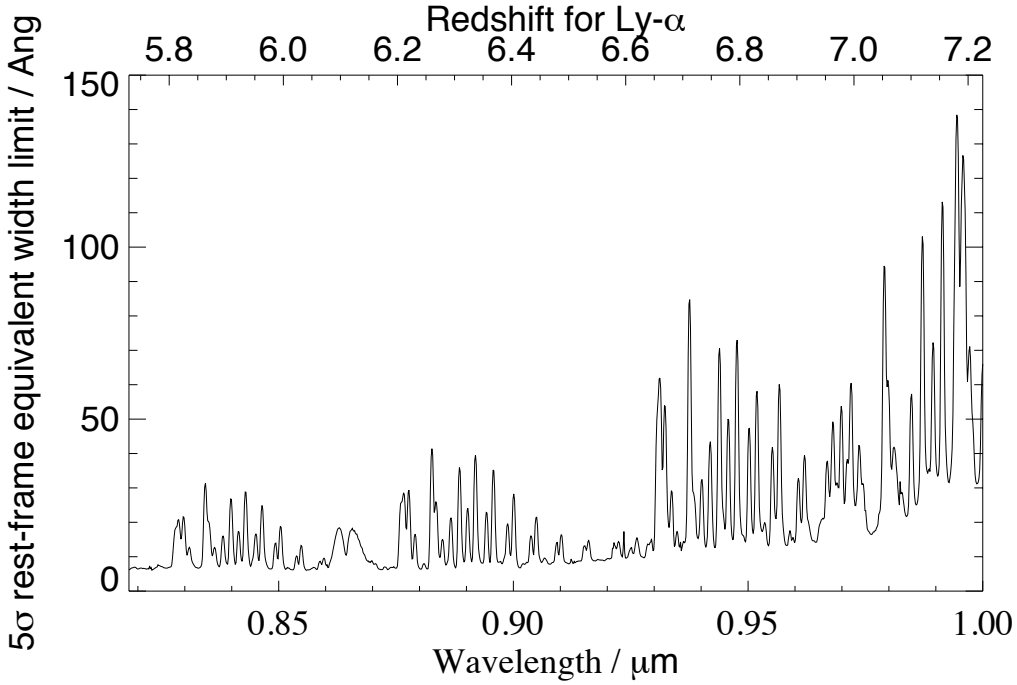

Figure 4.20: 5σ Rest-Frame Equivalent Width limits for HUDF.z.6433 from FORS2 observations.

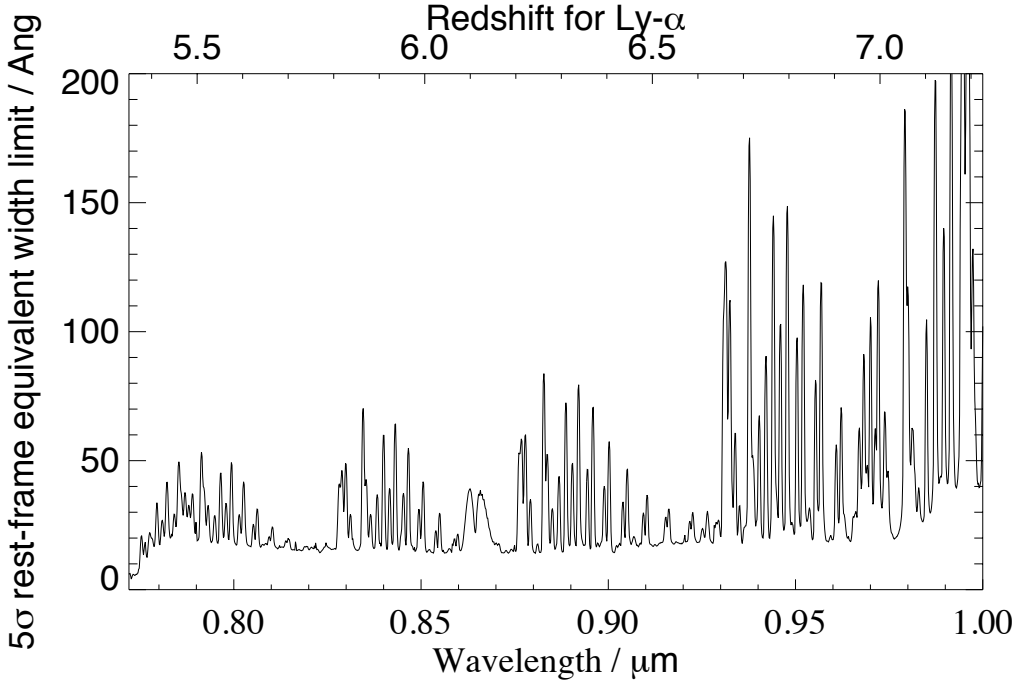

Figure 4.21: 5σ Equivalent Width limits for HUDF.z.7462 from FORS2 observations.

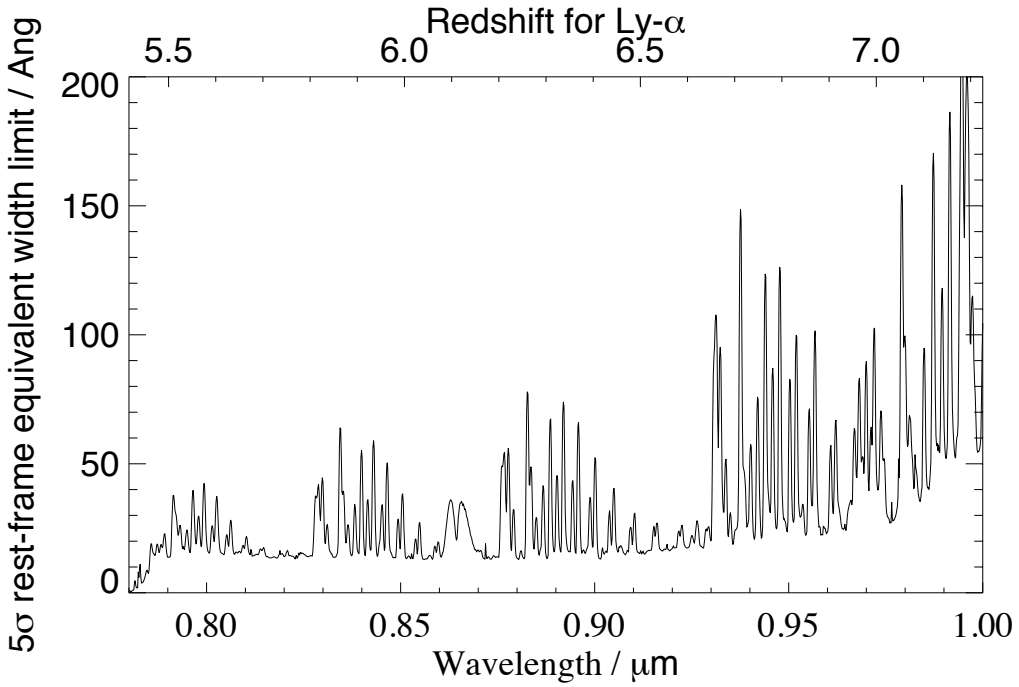

Figure 4.22: 5σ Rest-Frame Equivalent Width limits for UDFy-37218061 from FORS2 observations.

with GNIRS was not deep enough to comment with certainty about the reality of the line. This target was observed again with FORS2 and no evidence of Lyman-α emission is found at the reported wavelength. (Lyman-α emission for this object was also searched for in other wavelength regions, but none was found.) The findings are presented in Fig. 4.23. From the results of our FORS2 observations the reported tentative Lyman-α emission can be confidently ruled out as being real.

4.5 Detection of Lyman-α emission in i-band dropouts

A number of objects targeted by our spectroscopy consisted of i-band dropouts; these were observed as filler targets. Amongst these, Lyman-α emission is detected in 4 objects, enabling a precise calculation of the redshift for these objects. The spectroscopic redshift of two of these objects had already been determined before (by

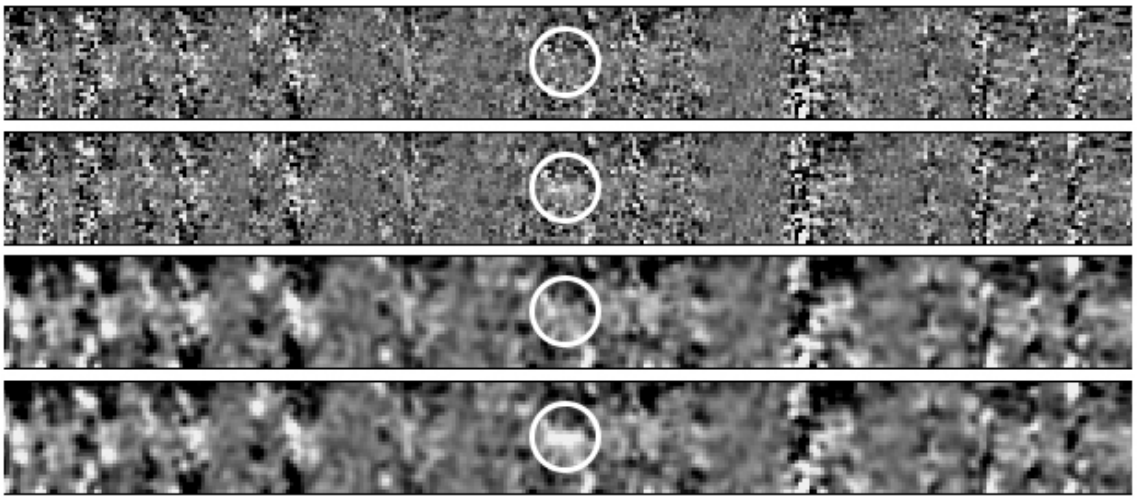

Figure 4.23: The calibrated FORS2 spectrum, with the location of HUDF.zD1 and the expected wavelength of the tentative Lyman-α emission reported by Fontana et al. (2010) marked with a white circle. Wavelength increases from left to right. From top to bottom: (a) the reduced data. Vertical lines of higher noise are due to night sky emission lines; (b) a fake source with the same line flux ($3.4 \times 10^{-18}\,\mathrm{erg\,cm^{-2}\,s^{-1}}$), wavelength and profile as the Fontana et al. (2010) line added into the frame. (c) the reduced data convolved with an elliptical Gaussian with $\sigma = 1$. (d) a fake source with the same line flux ($3.4 \times 10^{-18}\,\mathrm{erg\,cm^{-2}\,s^{-1}}$) and wavelength as the Fontana et al. (2010) line added into the frame. The resulting frame has been Gaussian smoothed ($\sigma = 1$). A line with the same strength as that reported in Fontana et al. (2010) (which was measured to have S/N $\leq$ 7 in their spectroscopy) is expected to be detected at 10σ in our observations, but only 3.22σ is measured.

Stanway et al., 2004 and Vanzella et al., 2009), whereas the redshift for two other objects is being presented in this thesis for the first time. The properties of these objects are presented in Figures 4.24 - 4.27.

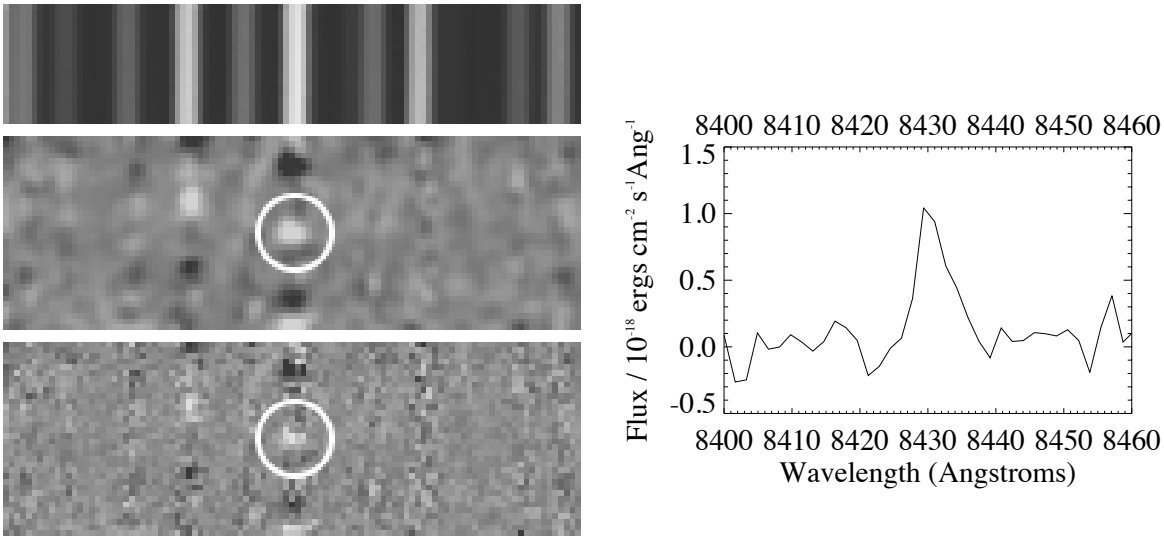

Figure 4.24: CDFS-2418044023. Left: The lower panel shows 2D spectrum around Lyman-α (with the emission feature circled), the middle panel shows the same smoothed with a Gaussian of σ = 1pix, and the upper panel shows the sky spectrum for the same wavelength range. Right: The 1D spectrum around Lyman-α, extracted over a width of 1.25" (5 pixels). The observed Lyman-alpha emission line is centered on 8430.94Å placing the object at a redshift $z = 5.94$. The total flux contained within the line is 5.13×10^{-18} ergs cm^{-2}s^{-1}Å^{-1}. The Equivalent width of the line is 38Å.

Object	z-Range spanned by data (for Ly-α)	Frac_z	Median EW	$\text{Frac}_{\text{EW}<50\text{Å}}$	$\text{Frac}_{\text{EW}<75\text{Å}}$	$\text{Frac}_{\text{EW}<120\text{Å}}$
*ERSz-2352941047	5.06498 - 7.22593	0.829881	28.4834	0.746973	0.888393	0.976450
ERS.z.70546	5.06498 - 7.22593	0.735958	4.52055	1.00089	1.00089	1.00089
*ERSz-2225141173	5.06498 - 6.85988	0.688642	11.5909	0.990151	1.00684	1.00684
ERS.z.87209	5.06498 - 7.36495	0.951587	11.8495	0.955736	0.991614	1.00033
ERS.z.87326	5.06498 - 6.91993	0.556133	8.63367	0.996498	1.00000	1.00000
ERS.z.90192	5.06498 - 6.99560	0.535303	26.6905	0.711076	0.832045	0.928291
*ERSz-2432842478	5.64902 - 8.04441	0.992767	12.7258	0.868721	0.924968	0.966605
*ERSz-2354442550	5.10529 - 7.79517	0.987703	13.7694	0.842440	0.902680	0.963533
ERS.z.46030	5.06498 - 6.91334	0.407656	2.95940	1.00226	1.00226	1.00226
ERS.z.26813	5.06498 - 6.96188	0.506457	8.72831	0.994021	1.00147	1.00147
HUDF.z.1889	5.63174 - 8.03783	0.989248	137.138	0.352169	0.575387	0.736741
HUDF.z.2677	5.66629 - 8.04441	0.985346	94.1065	0.455781	0.557034	0.657736
UDFy-44706443	5.86043 - 8.04441	0.996583	381.286	0.0000009	0.0946618	0.256060
HUDF.z.4444	5.70825 - 8.04441	0.999833	29.1509	0.691916	0.744267	0.800252
*UDFz-41597044	5.64655 - 8.04030	0.994071	119.480	0.372133	0.551312	0.707679
HUDF.z.5141	5.45571 - 8.04441	0.999233	58.4470	0.573291	0.670767	0.751047
UDFy-39537174	5.51165 - 8.04441	0.999833	37.0766	0.629125	0.691969	0.774164
HUDF.z.6433	5.72963 - 8.04441	0.993973	58.2495	0.558168	0.657920	0.735550
*HUDF.z.6497	5.31751 - 7.99752	0.984130	138.993	0.200653	0.369185	0.524713
*M2560z	5.41211 - 8.03701	0.994107	209.090	0.0177285	0.324210	0.593746
HUDF.z.7462	5.35042 - 8.03289	0.981584	72.0892	0.465411	0.553892	0.651532
UDFy-37218061	5.41623 - 8.04441	0.991647	87.1091	0.413438	0.545083	0.664064

Table 4.3: This table for all objects targeted by our spectroscopy shows the redshift range spanned by our data for Lyman-α in Column 2. Column 3 shows the fractional probability that a galaxy drawn from the dropout sample would fall within the spectral coverage of that particular spectrograph setup. Column 4 gives the median EW for each object for the most probable redshift range (see Figure 3.28). The remaining three columns tabulate the fraction of our spectroscopy that has EW limits lower than our chosen threshold (50 Å, 75 Å and 120 Å respectively.) The figures in this table are for a line with an intrinsic velocity width of $300\,\text{km}\,\text{s}^{-1}$. An asterisk (*) before the object name indicates a marginal candidate which was not included in the chosen sample used for our analysis.

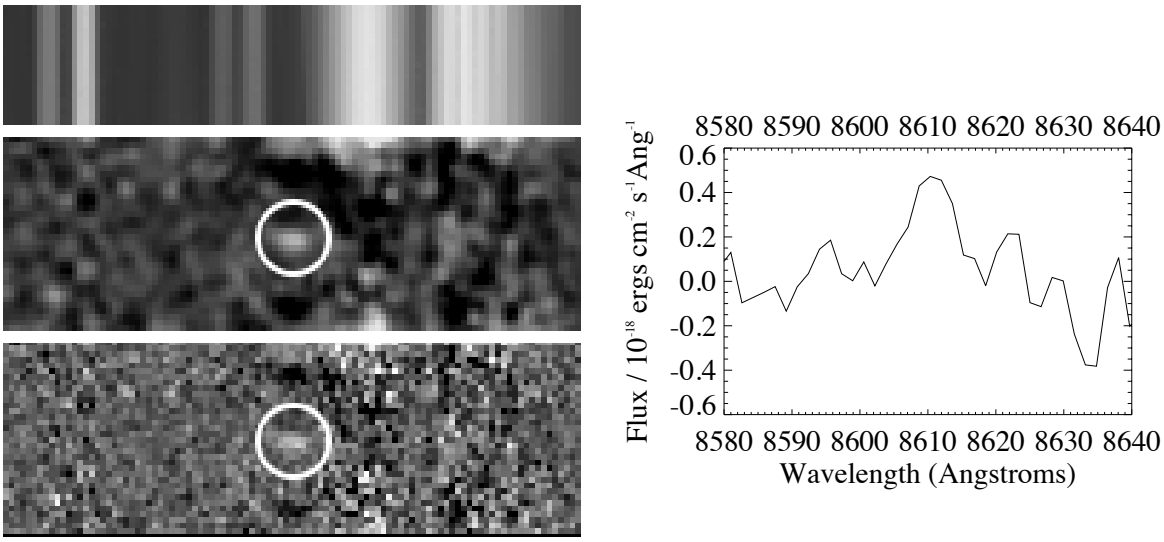

Figure 4.25: CDFS-2373844457. Left: The lower panel shows 2D spectrum around Lyman-α (with the emission feature circled), the middle panel shows the same smoothed with a Gaussian of σ = 1pix, and the upper panel shows the sky spectrum for the same wavelength range. Right: The 1D spectrum around Lyman-α, extracted over a width of 1.25" (5 pixels). The observed Lyman-alpha emission line is centered on 8610.58Å placing the object at a redhisft $z = 6.08$. The total flux contained within the line is 3.50×10^{-18} ergs cm^{-2}s^{-1}Å^{-1}. The Equivalent width of the line is 15Å.

$N_{\rm eff} = \sum$ Frac$_z \times$ Frac$_{\rm EW<thres}$		
EW$_{\rm thres} = 50$ Å	EW$_{\rm thres} = 75$ Å	EW$_{\rm thres} = 120$ Å
7.60571	8.65436	9.64324

Table 4.4: This table shows the total effective number of sampled galaxies with an EW upper limit lower than a set threshold, considering those z-drops targetted by FORS2 which were strong candidates. The figures in this table are for a line with an intrinsic velocity width of 300 km s^{-1}.

4.6 Analysis: The EW distribution and Constraints on the Neutral Fraction χ_{HI}

Since no Lyman-α emission is detected in any of the targeted z-drops, the precise redshift of these objects cannot be pinned down, so one has to rely on the *HST* photometry to assume that all these z-drops lie at $z \sim 7$. In particular, the expected

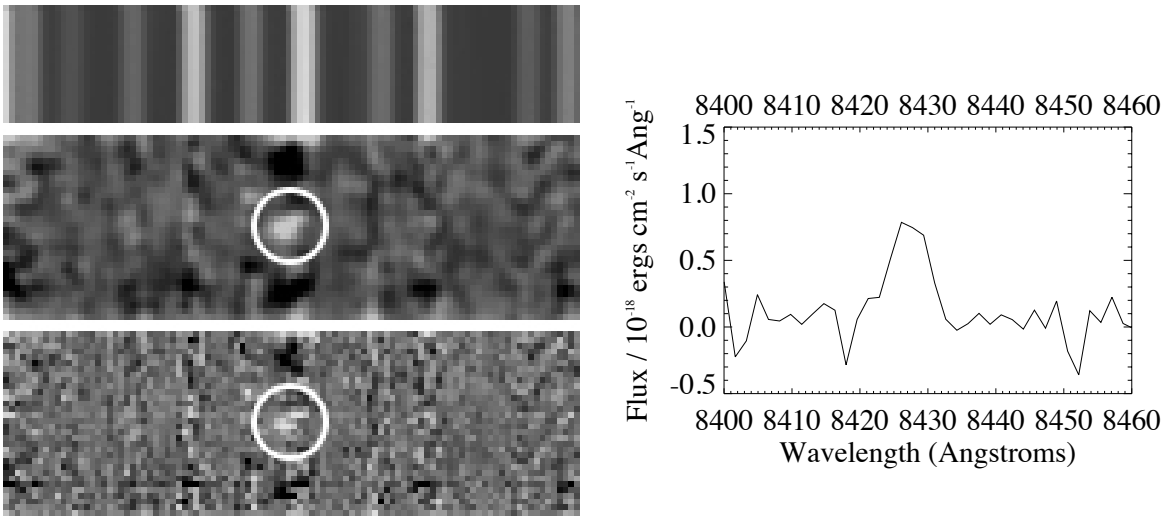

Figure 4.26: CDFS-2431845175. Left: The lower panel shows 2D spectrum around Lyman-α (with the emission feature circled), the middle panel shows the same smoothed with a Gaussian of σ = 1pix, and the upper panel shows the sky spectrum for the same wavelength range. Right: The 1D spectrum around Lyman-α, extracted over a width of 1.25" (5 pixels). The observed Lyman-alpha emission line is centered on 8427.05Å, placing this object at a redshift $z = 5.93$. The total flux contained within the line is 4.76×10^{-18} ergs cm^{-2}s^{-1}Å^{-1}. The Equivalent width of the line is 24Å. This object has also been observed by Stanway et al. (2004) (Glare-3011).

redshift distribution is taken from the simulations of Wilkins et al. (2011) - see Figure 4.28. For each of these spectroscopic targets, M_{1600}, the rest-frame UV absolute magnitude around $\lambda_{rest} = 1600$ Å, was computed so that the appropriate scenario to use from the simulations in Fig. 4.28 could be chosen, selecting the relevant curve and field (HUDF or ERS). The probability of recovering a galaxy at a certain redshift was computed from these simulations.

Following this, the same approach used in Chapter 3 was adopted, considering three different thresholds on the rest-frame EW (50Å, 75Å and 120Å) for each target and then calculating the fraction of our spectroscopy which probed EW limits lower than a given threshold, which fraction is here called $\mathrm{Frac}_{\mathrm{EW<thresh}}$, weighted by the redshift probability distribution for the dropout galaxy.

The position of each slit on the detector varied; this means that the spectral range

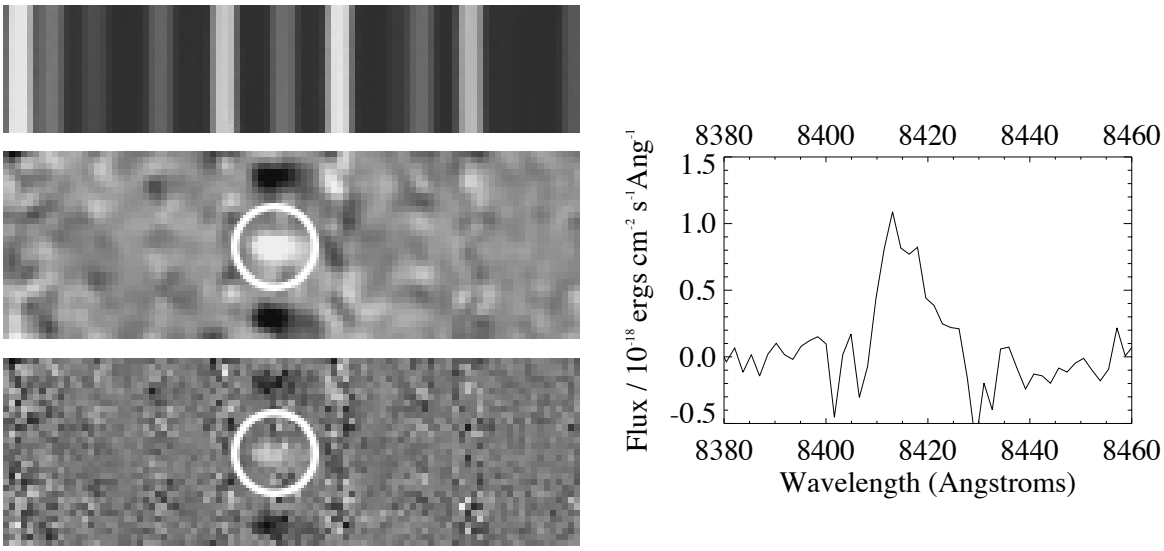

Figure 4.27: HUDF-39065387. Left: The lower panel shows 2D spectrum around Lyman-α (with the emission feature circled), the middle panel shows the same smoothed with a Gaussian of σ = 1pix, and the upper panel shows the sky spectrum for the same wavelength range. Right: The 1D spectrum around Lyman-α, extracted over a width of 1.25" (5 pixels). The observed Lyman-alpha emission line is centered on 8415.68Å placing this object at a redshift $z = 5.92$. The total flux contained within the line is 8.22×10^{-18} ergs cm^{-2}s^{-1}Å^{-1}. The Equivalent width of the line is 49Å. This object has also been observed by Vanzella et al. (2009).

covered is different for each slit. The likelihood function for a galaxy to be lying at a certain redshift enabled us to compute the fractional probability (Frac$_z$) that a galaxy drawn from the sample of observed targets would fall within the spectral range covered. The product of Frac$_z$ and Frac$_{\mathrm{EW<thresh}}$ gives the effective number of observed galaxies, N_{eff}, probed with a sensitivity greater than the chosen EW threshold. Table 4.4 gives N_{eff} for our three chosen thresholds. To derive these numbers not all observed objects were considered. Instead only those targets which are strong candidates were chosen. The objects which were rejected are marked with an asterisk (*) in Table 4.3.

Once again, our results our compared with the work of Stark et al. (2010) (the four data points with error bars in Figure 4.29) whose spectroscopic sample covers a range in UV luminosities of -19.5 > M$_U V$ > -20.5, which is similar to range of

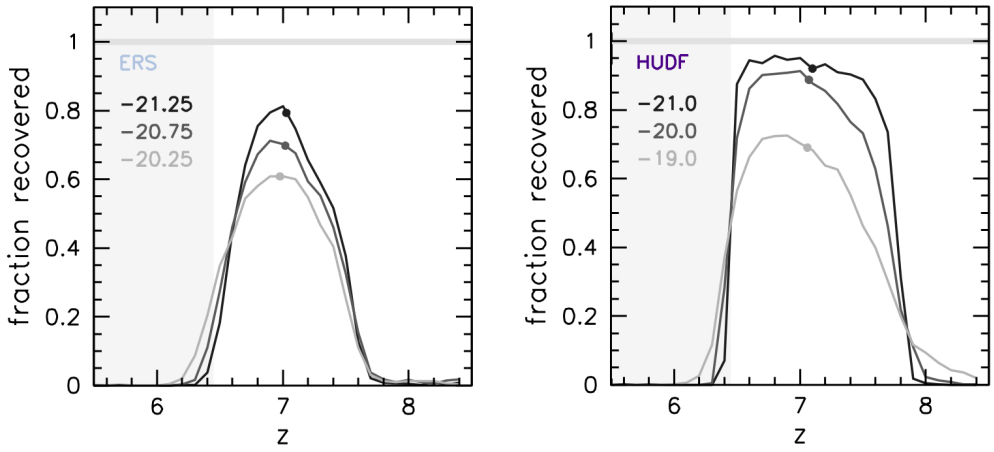

Figure 4.28: The probability of recovering a galaxy in the simulations for z-band dropouts described in Wilkins et al. (2011) for the HUDF and ERS fields as a function of redshift for several different absolute rest-frame M_{1600} magnitudes. The results of these simulations are used to provide the expected redshift distributions for our z-drops. In both figures, the mean redshift is denoted by a dot.

luminosities of our own sample.

From Table 4.4 one can see that for a threshold of 75Å, $N_{eff} = 8.65$. Referring to Figure 4.29, one sees that if the fraction of Lyman-α emitters at $z = 7$ follows the linear trend observed at lower redshifts, then at $z = 7$ one should expect $X_{Ly\alpha} = 0.25 \times 8.65 = 2.16$. So one expects 2.16 galaxies in our chosen sample to exhibit Lyman-α emission in this scenario. However, none are observed. So using Equation 3.3 this prediction can be rejected at a confidence level of $100 \times (1 - [f_0]) = 100 \times (1 - [2.16^0 e^{-2.16}/0!]) = 88\%$.

The extrapolated fraction of Lyman-α emitters from lower redshifts would hold if the neutral fraction of Hydrogen were 0. This means that if our results were in agreement with the extrapolated $X_{Ly\alpha}$ at $z = 7$ from lower redshifts, then they would be consistent with the neutral fraction, χ_{HI}, being 0. Unless the properties of the distribution of galaxies varied with redshift, our significant disagreement with this trend could very well imply that $\chi_{HI} > 0$ at $z = 7$. This possibility is fully discussed (in conjunction with the results of Chapter 3) in the next Chapter.

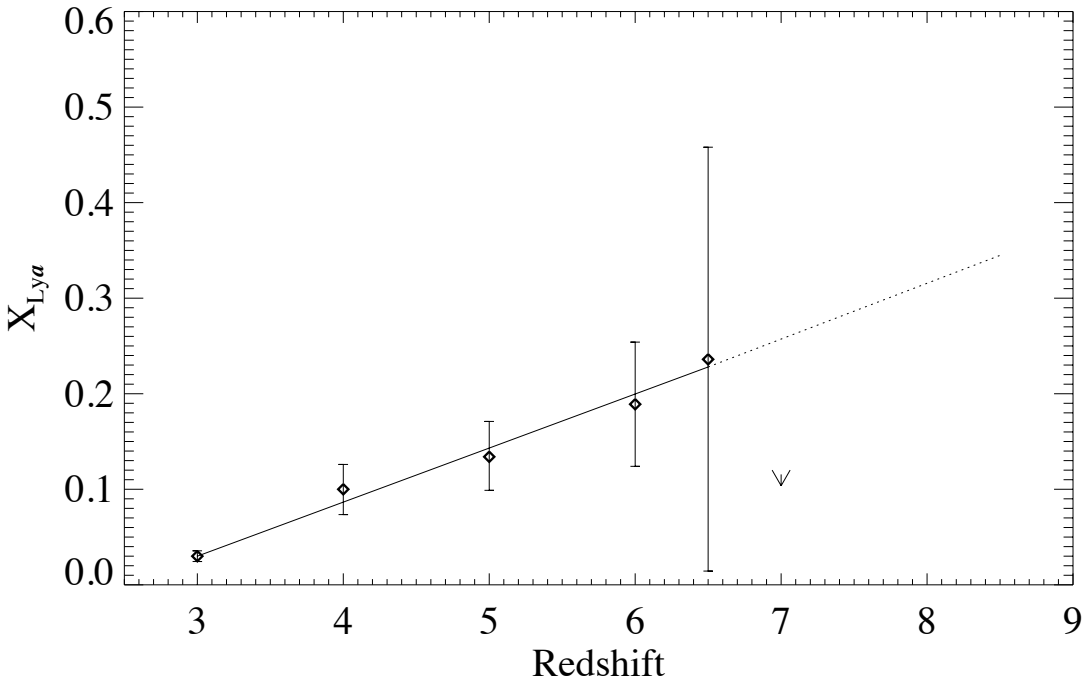

Figure 4.29: Our upper limits on the fraction of high rest-frame equivalent Lyman-α emission at $z \geq 7$ are shown for the z-drops ($z = 7$) targeted with FORS2. The tail of the arrows shows the 75 Å limit and head shows the 120 Å limit, in both cases considering a line with an intrinsic velocity width of 300km/s. The diamond symbols are results obtained at lower redshift by Shapley et al. (2003) at $z = 3$ and Stark et al. (2010) at $z = 4-6.5$. For comparison, the low-redshift trend is extrapolated to higher redshifts (dotted line). Our upper limits are inconsistent with this extrapolation at a confidence level of 88%, quite possibly indicating that the IGM neutral fraction $\chi_{HI} > 0$ at $z > 7$.

Chapter 5

Conclusion

5.1 The Goals of the Project

The work described in this thesis was set to explore the $z > 7$ universe, probing the era of reionization via spectroscopy of primeval galaxy candidates identified using the Lyman-break technique. In particular, the emergence of Lyman-α emission from these high-redshift candidate galaxies was a key question to be investigated by this work. This Lyman-α emission is produced in a process which sees young stars emitting UV radiation which is then absorbed and then re-radiated by surrounding neutral hydrogen gas. In Chapter 1 it was noted how the emergence of this radiation partly depends on the neutral fraction of Hydrogen, χ_{HI}; thus, the emergence of Lyman-α from these primeval galaxies becomes a sensitive diagnostic of the neutral fraction at high redshifts. So to recapitulate, the main aims of this work were to:

- Investigate the question of whether Lyman-α emerges during the epoch of reionization.
- Confirm the redshift of any targeted galaxy candidates exhibiting Lyman-α emission.

- Use the observed fraction of Lyman-α emitters in our sample to infer the neutral fraction of Hydrogen, χ_{HI}, at $z > 7$.

5.2 The Emergence of Lyman-α at $z > 7$

As has been argued in this thesis, one of the key results from this work is the lack of Lyman-α emission in our sample of objects. With the exception of 4 i-band dropouts (2 of which had already been confirmed before) for which very robust detections of the Lyman-α line was obtained, placing these objects at a redshift of around 6, no Lyman-α emission was observed in any of our targeted z-drops or Y-drops. The analysis presented in this thesis suggests that the lack of evidence for Lyman-α emission in this sample of candidate $z > 7$ galaxies is not due to technological limitations of current instrumentation, but rather that it is a true characteristic of the observed targets.

Even the observation of a single high-z galaxy can be used to answer the question of whether the observations are consistent with an HII region produced by such a source alone within a neutral IGM. If the answer is in the affirmative, then the global ionization state of the universe cannot be constrained by the detected Lyman-α emission. On the other hand, if the answer to this question is negative, then one can conclude that the surrounding region had to be ionized previously, due to either the universe being globally reionized, or due to local reionization by nearby sources (Loeb et al., 2005; Dayal and Ferrara, 2011). For this reason, HUDF.YD3, a Y-drop which was claimed to exhibit Lyman-α emission at 11615.6 Å by Lehnert et al. (2010) was investigated carefully; this claimed emission line would place it at $z = 8.6$ making it the only object at such a high redshift with observed Lyman-α emission, however this result could not be confirmed with our observations.

Since no confirmed spectroscopic redshifts for our $z > 7$ sample are available, in

drawing our conclusions it is being assumed that our sample truly consists of $z > 7$ galaxies; in other words, the photometry is solely being relied upon to assume that the observed objects lie at $z > 7$. Given the very good photometric quality of WFC3 data and the fact that for our analysis weak candidates present in our sample were not considered, our observations are not expected to be compromised by a significant fraction of low-redshift contaminants.

Making this assumption, one may suggest that the fraction of Lyman-α emitters at $z > 7$ must be quite low; compared with the fraction of Lyman-α emitters observed at lower redshifts, the fraction at $z > 7$ seems to be significantly less. Indeed no evidence at all for Lyman-α emission is found in our spectroscopic sample of $z > 7$ candidates. In total, our combined sample of targets (across all four spectrographs used for this work) consists of 27 z-drops and 3 Y-drops. Ignoring any weak z-drop candidates in our FORS2 sample (7 objects), the revised total of targeted samples consists of 15 z-drops and 3 Y-drops. Lyman-α emission was not detected in any of these objects. In our analysis the fraction of Lyman-α emitters at $z > 7$ is compared with that at lower-redshifts, basing on the work of Stark et al. (2010), building on work by Stanway et al. (2007) at $z = 6$ and Shapley et al. (2003) at $z = 3$. Accounting for any lack in coverage over certain wavelength regions and taking into consideration the completeness of our sample, effectively 9.63 $z-$drops and 1.15 Y-drops are observed down to an Equivalent Width of 75Å.

Extrapolating the fraction of Lyman-α emitters at lower redshifts to $z = 7$, one expects $X_{Ly\alpha} \sim 0.25$ at $z = 7$, i.e. the fraction of Lyman-α emitters is expected to be 0.25 at $z = 7$. Given our effective number of observed galaxies at $z = 7$ (9.63) one would expect to observe $0.25 \times 9.63 = 2.4$ galaxies in the combined sample[1] that is being considered, but none are detected. This implies that this hypothesis can be

[1]keeping in mind that in the analysis of our Gemini/GNIRS & VLT XSHOOTER sample, an intrinsic line velocity of 200km s^{-1} is being assumed, whereas for the deeper spectroscopy obtained with VLT/FORS2 an even wider 300km s^{-1} line

rejected at a confidence level of $\sim 91\%$.

If the targeted Y-drops at $z = 8.5$ are included in the analysis to derive a constraint at $z = 7.8$ (the average redshift resulting from considering z-drops at $z \sim 7$ and Y-drops at $z \sim 8.5$) then one would expect $X_{Ly\alpha} \approx 0.3$ if the extrapolated evolution from lower redshifts of the Lyman-α fraction holds. The total effective number of observed galaxies (z-drops and Y-drops combined) is 10.78 which means that across the whole sample one would expect to observe $0.3 \times 10.78 = 3.23$ galaxies. Since none are observed, a model which predicts that the fraction of Lyman-α emitters at $z = 7.8$ follows the trend seen at lower redshifts can be rejected at a confidence level of $\sim 96\%$.

One should of course note that the data points reproduced here from Stark et al. (2010) do have associated error bars; consequently, the gradient of this linear extrapolation could be lower, and this would have the effect of decreasing the quoted confidence limits. However, the results of the combined sample (across all datasets) offer a strong enough constraint that they still represent a marked drop from the expected fraction at $z = 7$, even if a smaller gradient were used in fitting the data points.

As discussed in Chapter 1, this lack of Lyman-α emission has been observed by other groups (eg. Fontana et al., 2010, Vanzella et al., 2011, Pentericci et al., 2011, Schenker et al., 2012, Ono et al., 2012, with the last study targeting more luminous sources by virtue of their selection based on Subaru imaging), so in this respect this study seems to be in agreement with other studies which suggest a drop in the fraction of Lyman-α emitters at $z > 7$. It should also be noted that the work of Stark et al. (2010) was extended in Stark et al. (2011) who predict that unless the neutral fraction rises between $z = 6$ and $z = 7$, Lyman-α should be readily detectable in spectroscopic campaigns at $z = 7$. The same result finds support in observations made at $z = 5.7$ and $z = 6.5$ by Ouchi et al. (2010) and Kashikawa et al. (2011) respectively, both

of which studies report a decrease in EWs. They also report little evolution in the rest UV luminosity function for Lyman break galaxies whilst observing a decrease in the Lyman-α luminosity function. Such observations could imply an increase in χ_{HI}, which is discussed in the next section.

5.3 Constraining χ_{HI}, the Neutral Fraction of Hydrogen

Numerous theoretical studies in the literature have investigated how an increase in the neutral fraction of Hydrogen in the Intergalactic Medium could impact the transmission of Lyman-α photons from galaxies (e.g. Santos, 2004, Furlanetto et al., 2006, McQuinn et al., 2007, Mesinger and Furlanetto, 2008). All of our spectroscopic results (across all spectrographs) are compared with the plot produced by Stark et al. (2010) (see Fig. 5.1 below) who derive a mapping between Lyman-α fractions and χ_{HI} basing on the 200 Mpc radiative transfer simulations of McQuinn et al. (2007). These simulations investigate the impact of patchy reionization on the Lyman-α line profile, the luminosity function and the clustering of Lyman-α emitters for several realistic models of reionization.

In deriving the mapping between Lyman-α fractions and χ_{HI}, Stark et al. (2010) make a number of assumptions, which should be briefly outlined here since our results are being directly compared to their conclusions. Initially they assume that: (a) the Lyman-α fraction would not evolve between $z \simeq 6$ and $z \simeq 7$, and that (b) the predicted decline in the amplitude of the Lyman-α luminosity function (with respect to a fully ionized IGM) would result in an identical decrease in the fraction of Lyman-α emitters. However, this is not a realistic scenario because the Lyman-α fraction does evolve with redshift even if there is no change in the ionization state of the IGM. For instance, Bouwens et al. (2010) suggest that obscuration by dust continues to

evolve over $z \gtrsim 6-8$, which would imply that in the absence of any evolution in the ionization state of the IGM, the Lyman-α fraction would be expected to be even larger at $z \simeq 6.5-7$. For this reason, Stark et al. (2010) then extend the smooth evolution observed in the Lyman-α fraction between $z \sim 4$ and $z \sim 6$ to $z > 6$.

One should note that the fraction of Lyman alpha emitters (over the $3.0 < z < 6.2$ redshift range) does have a luminosity dependence, which is presented in Figure 13 of Stark et al. (2010). However our comparison is ensured to be a fair one by considering only those galaxies in the sample which have a comparable absolute magnitude as the sample used in the analysis of Stark et al. (2010). It should also be stressed that the same rest-frame Equivalent Width threshold as that of Stark et al. (2010) is being imposed (namely, 75Å). Evidence for evolution is being sought for. Therefore, a model of the fraction of high Equivalent Width emitters observed at $z = 3-6$ is being considered, and then the following question is being asked: Extrapolating the trend observed at lower redshifts, would one expect to detect any Lyman-alpha emission at the higher redshifts probed by our spectroscopy? The conclusion is that one should indeed detect Lyman-α, but our observations yield no detection, hence one can rule out such a model. Looking at samples of such objects at lower redshift, it is true that some sources might have low Equivalent Widths, but these would be far below the sensitivity limits of this spectroscopy, so that subset of the population cannot be constrained. For this reason, the comparison which is being made here is between the high Equivalent Width emitters.

On the plot in Figure 5.1 is shown the location of various χ_{HI} constraints (triangle symbols), reproduced from Stark et al. (2010), in order to derive a comparison between our own results and these values to constrain the neutral fraction of Hydrogen in the Intergalactic Medium at $z = 7$. As can be seen from the plot, our results at $z \sim 7$ (arrow at $z = 7$) indicate a significant evolution in the χ_{HI} from $z \sim 6$, suggesting that $\chi_{HI} \sim 0.5$. The combined limit from our zdrop observations (arrow at $z = 7$)

and ydrop observations (arrow at $z = 8.5$) is shown at the average redshift of $z = 7.8$.

These results are in agreement with those obtained from other observational campaigns which cited simulations other than those of McQuinn et al. (2007) (which are used in our case) to derive a value for χ_{HI}. Ota et al. (2008, 2010) observe a lack of Lyman-α emitters in the deep NB973 survey of the Subaru Deep Field; using these results in conjunction with the reionization models of Santos (2004) they estimate $\chi_{HI}^{z=7}$=0.32-0.62. Assuming that the universe is completely ionized by $z = 6$ and adopting the semi-analytical models of Dijkstra et al. (2011), Pentericci et al. (2011) find that their observations of 20 galaxies require a change in the neutral fraction of the order of $\Delta\chi_{HI} \sim 0.6$ in just $\Delta z \sim 1$ (from $z \sim 6$ to $z \sim 7$). Schenker et al. (2012) combine the results from their Keck LRIS observations (19 sources) together with the results of Fontana et al. (2010) (7 sources); using these combined results in conjunction with the reionization model of McQuinn et al. (2007) (the same one adopted for our comparison) they derive $\chi_{HI} = 0.44 - 0.51$. Ono et al. (2012) compare their results with those of Dijkstra et al. (2011) and derive an even higher value for the neutral fraction, suggesting $\chi_{HI} \sim 0.6 - 0.9$. So our results can be seen to be in broad agreement with other recent literature. On the subject of observations in support of an increase in χ_{HI}, it is apt to also remind ourselves of the quasar ULASJ112001.48+064124.3 (Mortlock et al., 2011), which lies at the low-redshift end of what is probed by the study presented in this thesis, and was discussed in Chapter 1, Section 1.8.2. From a measurement of the near-zone radius of ULASJ1120+0641 Mortlock et al. (2011) find that the neutral fraction was a factor of about 15 higher at $z = 7.1$ than what it was at $= 6.2$.

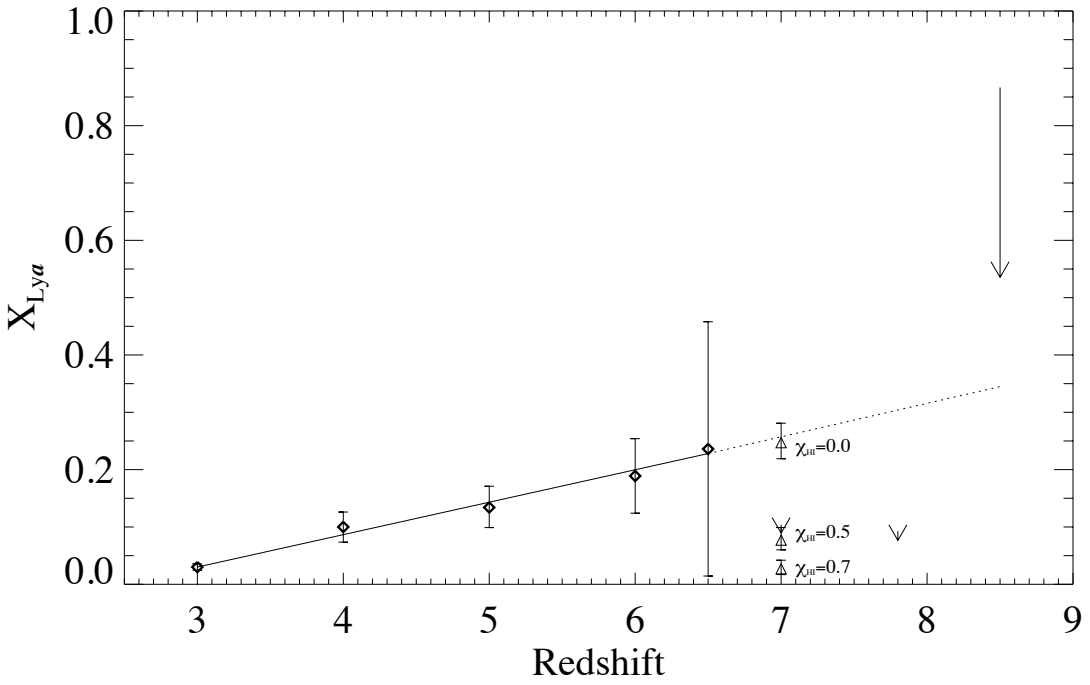

Figure 5.1: Our upper limits on the fraction of high rest-frame equivalent Lyman-α emission at $z \geq 7$ are shown for the z-drops ($z = 7$) targeted with VLT/FORS2, Gemini/GNIRS and VLT/XSHOOTER and the Y-drops ($z = 8.5$) targeted with VLT/XSHOOTER. The tail of the arrows represents our 75 Å limit and the head of the arrows represents our 120 Å limit. The diamond symbols are results obtained at lower redshift by Shapley et al. (2003) at $z = 3$ and Stark et al. (2010) at $z = 4 - 6.5$. For comparison, the low-redshift trend is extrapolated to higher redshifts (dotted line). Our upper limits are inconsistent with this extrapolation at a confidence level of 91% at $z = 7$ and 96% at $z = 7.8$, quite possibly indicating that the IGM neutral fraction $\chi_{HI} > 0$ at $z \geq 7$. Our results would suggest that $\chi_{HI} \sim 0.5$, which would be in agreement with other studies.

5.4 The Future

Whilst significant effort has gone into spectroscopic observations at $z \sim 7$ by various groups, and a lot of progress has been made from an imaging point of view at $z \sim 8$, it is clear that more spectroscopic data is required to assess the distribution of Lyman-α emission and absorption at these redshifts, especially at $z \sim 8$. These multiple observational efforts suggest a marked decline in the fraction of Lyman-α emitters at $z > 7$, but to confirm this, larger samples are required which would provide even more robust statistics. A recent study at $z = 6.5$ by Cowie et al. (2011) highlights the importance of further investigation. Cowie et al. (2011) focused on 7 Lyman-α selected galaxies at $z = 6.5$ (which were selected from the Lyman-α spectroscopic atlas of Hu et al., 2010); comparing these with continuum-selected samples at the same redshift, they report that the fraction of Lyman-α emitters is similar to that at lower redshifts, suggesting that they find no sign of the effects associated with reionization. So whilst, as has seen above, numerous studies do seem to be in agreement with our own findings that there is a drop in the Lyman-α fraction, it is very important to increase the sample size in order to determine whether results such as Cowie et al.'s (2011) might be suffering from uncertainties arising from cosmic variance in the continuum luminosity functions. Such continued study would also prove useful in investigating other interesting questions, such as the homogeneity of the reionization process.

Dunkley et al. (2009) use polarization measurements from WMAP data to derive constraints for reionization, claiming that instantaneous reionization during late epochs below $z = 8.2$ (6.7) can be rejected at the 2σ (3σ) level, arguing instead for an extended reionization process taking place between $z \sim 6 - 11$. The current problem is that physical models cannot easily reproduce such an extended era of reionization because of the rapid recombination of Hydrogen (e.g. Cen, 2003). Studies such as the one presented in this thesis can be used to address this question. Indeed, if the

lack of observed Lyman-α emission at $z = 7$ is interpreted as signifying an increase in the neutral fraction from lower redshifts, suggesting a significant departure from $\chi_{HI} = 0$, then they support the claim that reionization was definitely not complete by $z = 7$. Further spectroscopic studies on even larger samples of high-redshift galaxies hold the promise of tackling this puzzling question with greater clarity and possibly solving this cosmological problem.

Finally, it should be noted that when it comes to using the Lyman-α fraction to constrain the neutral fraction, a recent study by Bolton and Haehnelt (2012) suggests an alternative viewpoint from a theoretical perspective as to whether the currently observed drop in the fraction of Lyman-α emitters should indeed be interpreted as signifying a change in the neutral fraction from that at lower redshifts. Bolton and Haehnelt (2012) ran a hydrodynamical simulation reproducing the absorption spectra of $z \sim 6 - 7$ quasars, and showed how, as one begins to approach the tail-end of reionization, in average regions of the universe the opacity of the intervening IGM red-ward of rest-frame Lyman-α can rapidly rise due to an increase in the incidence of optically thick absorption systems. They go further to suggest that, if one assumes that the observed decline in the fraction of Lyman-α emitters is solely due to evolution in the neutral fraction, then a volume averaged neutral fraction of $\sim 10\%$ could be enough to provide agreement with the observed Lyman-α emitter fraction at $z \sim 7$. Rather than requiring a very steep change in χ_{HI}, they propose that the observed drop in the Lyman-α emitter fraction could be explained by a rapid decrease in the mean free path of ionizing photons, which is expected during the final stages of reionization.

We are living in very interesting times for studies of the high-redshift universe, both from an observational and theoretical perspective. No doubt, theory and observation will continue to inform each other in the coming years. From a practical point of view, studies such as the one presented in this thesis show that such observations are notoriously difficult with current instrumentation, because it is challenging to

obtain large samples at $z > 6.5$, especially if aiming for a high level of completeness.

New instruments such as KMOS at the VLT will be well suited for IR follow-up surveys of such high-redshift objects, and ULTRA-VISTA will probe the bright end of the luminosity function, making it a perfectly poised instrument for selecting candidate galaxies suitable for follow-up spectroscopy. Follow up spectroscopy with MOSFIRE at Keck has the potential to provide the first evidence of Lyman-α emission at $z \sim 8$ while the VLT IFU spectrograph MUSE will allow us to look for Lyman-α emission over a wide redshift range (up to $z \sim 6.7$).

In the long term, the James Webb Space Telescope (JWST) will be a workhorse instrument for both identifying ultra high-redshift galaxies and also confirming them spectroscopically with the state-of-the-art multi-object-spectrograph NIRSpec, which will allow us to obtain spectroscopy on more than 100 sources simultaneously. If Lyman-α is indeed not emerging at these high redshifts, then spectroscopic confirmation of high-z candidates could be achieved using the OII line or other lines, including rest-UV absorption in the Interstellar Medium and stellar atmospheres.

This whole variety of upcoming instruments, in combination with ongoing theoretical efforts, will help us extend our knowledge of galaxy formation to ever higher redshifts, and once future observatories such as JWST and the European Extremely Large Telescope come online, we will be able to probe galaxy formation at $z > 15$.

Recalling that the first Hubble Deep Field image was made only as recently as 1996, we can appreciate better the long way we have come. One cannot help but wonder what new discoveries are awaiting us.

Bibliography

T. Abel, J. H. Wise, and G. L. Bryan. The H II Region of a Primordial Star. *ApJ*, 659:L87–L90, April 2007. doi: 10.1086/516820.

M. Ajiki, B. Mobasher, Y. Taniguchi, Y. Shioya, T. Nagao, T. Murayama, and S. S. Sasaki. Narrowband Survey of the GOODS Fields: Search for Lyα Emitters at z = 5.7. *ApJ*, 638:596–602, February 2006.

M. A. Alvarez, V. Bromm, and P. R. Shapiro. The H II Region of the First Star. *ApJ*, 639:621–632, March 2006.

P. Anninos and M. L. Norman. The Role of Hydrogen Molecules in the Radiative Cooling and Fragmentation of Cosmological Sheets. *ApJ*, 460:556, April 1996. doi: 10.1086/176992.

R. Barkana and A. Loeb. The Photoevaporation of Dwarf Galaxies during Reionization. *ApJ*, 523:54–65, September 1999. doi: 10.1086/307724.

R. Barkana and A. Loeb. In the beginning: the first sources of light and the reionization of the universe. *Phys. Rep.*, 349:125–238, July 2001. doi: 10.1016/S0370-1573(01)00019-9.

R. H. Becker, X. Fan, R. L. White, M. A. Strauss, V. K. Narayanan, R. H. Lupton, J. E. Gunn, J. Annis, N. A. Bahcall, J. Brinkmann, A. J. Connolly, I. Csabai, P. C. Czarapata, M. Doi, T. M. Heckman, G. S. Hennessy, Ž. Ivezić, G. R. Knapp,

D. Q. Lamb, T. A. McKay, J. A. Munn, T. Nash, R. Nichol, J. R. Pier, G. T. Richards, D. P. Schneider, C. Stoughton, A. S. Szalay, A. R. Thakar, and D. G. York. Evidence for Reionization at z$\sim$ 6: Detection of a Gunn-Peterson Trough in a z=6.28 Quasar. *AJ*, 122:2850–2857, December 2001. doi: 10.1086/324231.

A. J. Benson, N. Sugiyama, A. Nusser, and C. G. Lacey. The epoch of reionization. *MNRAS*, 369:1055–1080, July 2006.

E. Bertin and S. Arnouts. SExtractor: Software for source extraction. *A&AS*, 117: 393–404, June 1996.

S. P. Bhavsar, S. Bharadwaj, and J. V. Sheth. SHUFFLE: A New Statistical Bootstrap Method: Applied to Cosmological Filaments. In S. H. Holt and C. S. Reynolds, editors, *The Emergence of Cosmic Structure*, volume 666 of *American Institute of Physics Conference Series*, pages 303–306, May 2003. doi: 10.1063/1.1581807.

R. Blank and C. Cabelli. Teledyne imaging sensors h2rg visible and infrared focal plane array. `http://www.teledyne-si.com/imaging/H2RG%20Brochure%20-%20rev6%20v2-2%20-%20OSR.pdf`, April 2012. Accessed: 20/08/2012.

J. S. Bolton and M. G. Haehnelt. The nature and evolution of the highly ionized near-zones in the absorption spectra of z$\simeq$6 quasars. *MNRAS*, 374:493–514, January 2007. doi: 10.1111/j.1365-2966.2006.11176.x.

J. S. Bolton and M. G. Haehnelt. On the rapid demise of Lyman-alpha emitters at $z > 7$ due to the increasing incidence of optically thick absorption systems. *ArXiv e-prints*, August 2012.

J. R. Bond, L. Kofman, and D. Pogosyan. How filaments of galaxies are woven into the cosmic web. *Nat*, 380:603–606, April 1996. doi: 10.1038/380603a0.

R. J. Bouwens, G. D. Illingworth, J. P. Blakeslee, and M. Franx. Galaxies at z∼6: The UV Luminosity Function and Luminosity Density from 506 HUDF, HUDF Parallel ACS Field, and GOODS i-Dropouts. *ApJ*, 653:53–85, December 2006.

R. J. Bouwens, G. D. Illingworth, M. Franx, and H. Ford. $z \sim 7-10$ Galaxies in the HUDF and GOODS Fields: UV Luminosity Functions. *ApJ*, 686:230–250, October 2008. doi: 10.1086/590103.

R. J. Bouwens, G. D. Illingworth, P. A. Oesch, M. Stiavelli, P. van Dokkum, M. Trenti, D. Magee, I. Labbé, M. Franx, C. M. Carollo, and V. Gonzalez. Discovery of z∼8 Galaxies in the Hubble Ultra Deep Field from Ultra-Deep WFC3/IR Observations. *ApJ*, 709:L133–L137, February 2010. doi: 10.1088/2041-8205/709/2/L133.

R. J. Bouwens, G. D. Illingworth, P. A. Oesch, I. Labbé, M. Trenti, P. van Dokkum, M. Franx, M. Stiavelli, C. M. Carollo, D. Magee, and V. Gonzalez. Ultraviolet Luminosity Functions from 132 $z \sim 7$ and $z \sim 8$ Lyman-break Galaxies in the Ultra-deep HUDF09 and Wide-area Early Release Science WFC3/IR Observations. *ApJ*, 737:90, August 2011. doi: 10.1088/0004-637X/737/2/90.

M. N. Bremer, J. B. Jensen, M. D. Lehnert, N. M. F. Schreiber, and L. Douglas. Gemini H-Band Imaging of the Field of a z = 10 Candidate. *ApJ*, 615:L1–L4, November 2004. doi: 10.1086/426019.

V. Bromm, R. P. Kudritzki, and A. Loeb. Generic Spectrum and Ionization Efficiency of a Heavy Initial Mass Function for the First Stars. *ApJ*, 552:464–472, May 2001. doi: 10.1086/320549.

A. J. Bunker, L. A. Moustakas, and M. Davis. Resolving the Stellar Populations in a z=4 Lensed Galaxy. *ApJ*, 531:95–117, March 2000. doi: 10.1086/308432.

A. J. Bunker, E. R. Stanway, R. S. Ellis, R. G. McMahon, and P. J. McCarthy. A

star-forming galaxy at z=5.78 in the Chandra Deep Field South. *MNRAS*, 342: L47–L51, July 2003. doi: 10.1046/j.1365-8711.2003.06664.x.

A. J. Bunker, E. R. Stanway, R. S. Ellis, and R. G. McMahon. The star formation rate of the Universe at $z \sim 6$ from the Hubble Ultra-Deep Field. *MNRAS*, 355: 374–384, December 2004. doi: 10.1111/j.1365-2966.2004.08326.x.

A. J. Bunker, S. Wilkins, R. S. Ellis, D. P. Stark, S. Lorenzoni, K. Chiu, M. Lacy, M. J. Jarvis, and S. Hickey. The contribution of high-redshift galaxies to cosmic reionization: new results from deep WFC3 imaging of the Hubble Ultra Deep Field. *MNRAS*, 409:855–866, December 2010. doi: 10.1111/j.1365-2966.2010.17350.x.

R. Cen. The Universe Was Reionized Twice. *ApJ*, 591:12–37, July 2003. doi: 10.1086/375217.

H.-W. Chen, K. M. Lanzetta, and S. Pascarelle. Spectroscopic identification of a galaxy at a probable redshift of z = 6.68. *Nat*, 398:586–588, April 1999. doi: 10.1038/19251.

T. R. Choudhury and A. Ferrara. Updating reionization scenarios after recent data. *MNRAS*, 371:L55–L59, September 2006. doi: 10.1111/j.1745-3933.2006.00207.x.

F. R. Chromey. *To Measure the Sky.* Cambridge University Press, 2010.

F. R. Chromey and D. A. Hasselbacher. The Flat Sky: Calibration and Background Uniformity in Wide Field Astronomical Images. *PASP*, 108:944, October 1996. doi: 10.1086/133817.

B. Ciardi, A. Ferrara, F. Governato, and A. Jenkins. Inhomogeneous reionization of the intergalactic medium regulated by radiative and stellar feedbacks. *MNRAS*, 314:611–629, May 2000. doi: 10.1046/j.1365-8711.2000.03365.x.

P. C. Clark, S. C. O. Glover, R. S. Klessen, and V. Bromm. Gravitational Fragmentation in Turbulent Primordial Gas and the Initial Mass Function of Population III Stars. *ApJ*, 727:110, February 2011.

J. G. Cohen, D. W. Hogg, R. Blandford, L. L. Cowie, E. Hu, A. Songaila, P. Shopbell, and K. Richberg. Caltech faint galaxy redshift survey. x. a redshift survey in the region of the hubble deep field north. *The Astrophysical Journal*, 538, Issue 1: 29–52, 2000.

J. M. Colberg, K. S. Krughoff, and A. J. Connolly. Intercluster filaments in a ΛCDM Universe. *MNRAS*, 359:272–282, May 2005. doi: 10.1111/j.1365-2966.2005.08897.x.

M. Colless et al. The 2dF Galaxy Redshift Survey: spectra and redshifts. *MNRAS*, 328:1039–1063, December 2001.

L. L. Cowie, E. M. Hu, and A. Songaila. The UV-continuum Properties of Lyα-selected Galaxies at z = 6.5. *ApJ*, 735:L38, July 2011.

M. Davis et al. Science Objectives and Early Results of the DEEP2 Redshift Survey. In P. Guhathakurta, editor, *Discoveries and Research Prospects from 6- to 10-Meter-Class Telescopes II*, volume 4834 of *Society of Photo-Optical Instrumentation Engineers (SPIE) Conference Series*, pages 161–172, February 2003.

P. Dayal and A. Ferrara. Ancient giants: on the farthest galaxy at z= 8.6. *MNRAS*, 417:L41–L45, October 2011. doi: 10.1111/j.1745-3933.2011.01116.x.

P. Dayal and A. Ferrara. *MNRAS*, 421:2568–2579, April 2012.

P. Dayal, A. Maselli, and A. Ferrara. The visibility of lyman alpha emitters during reionization. *Monthly Notices of the Royal Astronomical Society*, 410:830, 2011.

C. De Breuck. High Redshift Radio Galaxies, the Most Massive Galaxies at Every Epoch. In *IAU Joint Discussion*, volume 12 of *IAU Joint Discussion*, August 2006.

R. H. Dicke, P. J. E. Peebles, P. G. Roll, and D. T. Wilkinson. Cosmic Black-Body Radiation. *ApJ*, 142:414–419, July 1965. doi: 10.1086/148306.

M. Dickinson. Galaxies at high redshift. In I. Pérez-Fournon, M. Balcells, F. Moreno-Insertis, and F. Sánchez, editors, *Galaxies at High Redshift*, pages 29–68, 2003.

M. Dijkstra. Continuum Emission by Cooling Clouds. *ApJ*, 690:82–88, January 2009.

M. Dijkstra. Observational signatures of lyman alpha emission from early galaxy formation. arXiv:1102.3157v1, February 2011.

M. Dijkstra, Z. Haiman, and A. Loeb. A Limit from the X-Ray Background on the Contribution of Quasars to Reionization. *ApJ*, 613:646–654, October 2004.

M. Dijkstra, A. Mesinger, and J. S. B. Wyithe. The detectability of Lyα emission from galaxies during the epoch of reionization. *MNRAS*, 414:2139–2147, July 2011. doi: 10.1111/j.1365-2966.2011.18530.x.

P. Dijkstra and J.S.B. Wyithe. Seeing through the trough: outflows and the detectability of ly-alpha emission from the first galaxies. *Monthly Notices of the Royal Astronomical Society*, 408:352, 2010.

S. Djorgovski and M. Dickinson. CCD data taking modes and flatfielding problems. *Highlights of Astronomy*, 8:645, 1989.

S. D'Odorico, H. Dekker, R. Mazzoleni, J. Vernet, I. Guinouard, P. Groot, F. Hammer, P. K. Rasmussen, L. Kaper, R. Navarro, R. Pallavicini, C. Peroux, and F. M. Zerbi. X-shooter UV- to K-band intermediate-resolution high-efficiency spectrograph for the VLT: status report at the final design review. In *Society of Photo-Optical Instrumentation Engineers (SPIE) Conference Series*, volume 6269 of *Society of Photo-Optical Instrumentation Engineers (SPIE) Conference Series*, July 2006.

J. Dunkley, E. Komatsu, M. R. Nolta, D. N. Spergel, D. Larson, G. Hinshaw, L. Page, C. L. Bennett, B. Gold, N. Jarosik, J. L. Weiland, M. Halpern, R. S. Hill, A. Kogut, M. Limon, S. S. Meyer, G. S. Tucker, E. Wollack, and E. L. Wright. Five-Year Wilkinson Microwave Anisotropy Probe Observations: Likelihoods and Parameters from the WMAP Data. *ApJS*, 180:306–329, February 2009.

E. Dwek, F. Galliano, and A. P. Jones. The origin and evolution of dust in high-redshift galaxies. *Il Nuovo Cimento B*, 122, Issue 9:959–966, 2007.

R. S. Ellis. *Observations of the High Redshift Universe*, pages 259–364. 2008.

X. Fan, M. A. Strauss, D. P. Schneider, R. H. Becker, R. L. White, V. K. Narayanan, G. T. Richards, L. Pentericci, E. Grebel, and SDSS Collaboration. New z ¿ 6 Quasars Discovered in the Sloan Digital Sky Survey. In *American Astronomical Society Meeting Abstracts*, volume 34 of *Bulletin of the American Astronomical Society*, page 114.14, December 2002.

X. Fan, M. A. Strauss, R. H. Becker, R. L. White, J. E. Gunn, G. R. Knapp, G. T. Richards, D. P. Schneider, J. Brinkmann, and M. Fukugita. Constraining the Evolution of the Ionizing Background and the Epoch of Reionization with $z \sim 6$ Quasars. II. A Sample of 19 Quasars. *AJ*, 132:117–136, July 2006. doi: 10.1086/504836.

M. A. Fardal, N. Katz, J. P. Gardner, L. Hernquist, D. H. Weinberg, and R. Davé. Cooling Radiation and the Lyα Luminosity of Forming Galaxies. *ApJ*, 562:605–617, December 2001. doi: 10.1086/323519.

S. L. Finkelstein, C. Papovich, M. Giavalisco, N. A. Reddy, H. C. Ferguson, A. M. Koekemoer, and M. Dickinson. On the Stellar Populations and Evolution of Star-forming Galaxies at $6.3 < z < 8.6$. *ApJ*, 719:1250–1273, August 2010.

S. L. Finkelstein, G. J. Hill, K. Gebhardt, G. Blanc, N. Drory, and HETDEX Collaboration. HETDEX: Probing the Chemical Evolution of the Universe with Lyman

Alpha Emitting Galaxies. In *American Astronomical Society Meeting Abstracts*, volume 219 of *American Astronomical Society Meeting Abstracts*, page 424.16, January 2012.

D. J. Fixsen, E. S. Cheng, D. A. Cottingham, R. E. Eplee, Jr., R. B. Isaacman, J. C. Mather, S. S. Meyer, P. D. Noerdlinger, R. A. Shafer, R. Weiss, E. L. Wright, C. L. Bennett, N. W. Boggess, T. Kelsall, S. H. Moseley, R. F. Silverberg, G. F. Smoot, and D. T. Wilkinson. Cosmic microwave background dipole spectrum measured by the COBE FIRAS instrument. *ApJ*, 420:445–449, January 1994.

A. Fontana, E. Vanzella, L. Pentericci, M. Castellano, M. Giavalisco, A. Grazian, K. Boutsia, S. Cristiani, M. Dickinson, E. Giallongo, R. Maiolino, A. Moorwood, and P. Santini. The Lack of Intense Lyα in Ultradeep Spectra of z = 7 Candidates in GOODS-S: Imprint of Reionization? *ApJ*, 725:L205–L209, December 2010. doi: 10.1088/2041-8205/725/2/L205.

S. R. Furlanetto, M. Zaldarriaga, and L. Hernquist. The effects of reionization on Lyα galaxy surveys. *MNRAS*, 365:1012–1020, January 2006. doi: 10.1111/j.1365-2966.2005.09785.x.

M. J. Geller and J. P. Huchra. Mapping the universe. *Science (ISSN 0036-8075), vol. 246, Nov. 17, 1989, p. 897-903. Research supported by the Smithsonian Institution and Digital Equipment Corp.*, 246:897–903, November 1989.

J. R. Gott, III, M. Jurić, D. Schlegel, F. Hoyle, M. Vogeley, M. Tegmark, N. Bahcall, and J. Brinkmann. A Map of the Universe. *ApJ*, 624:463–484, May 2005.

J. E. Gunn and B. A. Peterson. On the Density of Neutral Hydrogen in Intergalactic Space. *ApJ*, 142:1633–1641, November 1965. doi: 10.1086/148444.

Z. Haiman and L. Knox. Reionization of the Intergalactic Medium and its Effect on the CMB. In A. de Oliveira-Costa and M. Tegmark, editors, *Microwave Fore-*

grounds, volume 181 of *Astronomical Society of the Pacific Conference Series*, page 227, 1999.

Z. Haiman and A. Loeb. Determining the Redshift of Reionization from the Spectra of High-Redshift Sources. *ApJ*, 519:479–485, July 1999.

Z. Haiman, A. A. Thoul, and A. Loeb. Cosmological Formation of Low-Mass Objects. *ApJ*, 464:523, June 1996. doi: 10.1086/177343.

Z. Haiman, M. J. Rees, and A. Loeb. Destruction of Molecular Hydrogen during Cosmological Reionization. *ApJ*, 476:458 (erratum 484, 985), February 1997. doi: 10.1086/303647.

Z. Haiman, T. Abel, and M. J. Rees. The Radiative Feedback of the First Cosmological Objects. *ApJ*, 534:11–24, May 2000a. doi: 10.1086/308723.

Z. Haiman, M. Spaans, and E. Quataert. Lyα Cooling Radiation from High-Redshift Halos. *ApJ*, 537:L5–L8, July 2000b. doi: 10.1086/312754.

D. S. Hayes and D. W. Latham. A rediscussion of the atmospheric extinction and the absolute spectral-energy distribution of VEGA. *ApJ*, 197:593–601, May 1975.

P. Hibon, N. Kashikawa, C. Willott, M. Iye, and T. Shibuya. Search for z ˜ 7 Lyα Emitters with the Suprime-Cam at the Subaru Telescope. *ApJ*, 744:89, January 2012. doi: 10.1088/0004-637X/744/2/89.

S. Hickey, A. Bunker, M. J. Jarvis, K. Chiu, and D. Bonfield. Constraints on star-forming galaxies at $z > 6.5$ from HAWK-I Y-band imaging of GOODS-South. *MNRAS*, 404:212–223, May 2010. doi: 10.1111/j.1365-2966.2009.15767.x.

C. M. Hirata and N. Padmanabhan. Cosmological production of H_2 before the formation of the first galaxies. *MNRAS*, 372:1175–1186, November 2006.

S. B. Howell. *Handbook of CCD Astronomy*. March 2006.

E. M. Hu, L. L. Cowie, P. Capak, R. G. McMahon, T. Hayashino, and Y. Komiyama. The Luminosity Function of Lyα Emitters at Redshift $z \sim 5.7$. *AJ*, 127:563–575, February 2004.

E. M. Hu, L. L. Cowie, A. J. Barger, P. Capak, Y. Kakazu, and L. Trouille. An Atlas of z = 5.7 and z = 6.5 Lyα Emitters. *ApJ*, 725:394–423, December 2010.

W. T. Hu. *Wandering in the Background: a Cosmic Microwave Background Explorer*. PhD thesis, UNIVERSITY OF CALIFORNIA, BERKELEY., 1995.

E. Hubble. A Relation between Distance and Radial Velocity among Extra-Galactic Nebulae. *Proceedings of the National Academy of Science*, 15:168–173, March 1929.

T. Ichikawa, R. Suzuki, C. Tokoku, Y. K. Uchimoto, M. Konishi, T. Yoshikawa, T. Yamada, I. Tanaka, K. Omata, and T. Nishimura. MOIRCS: multi-object infrared camera and spectrograph for SUBARU. In *Society of Photo-Optical Instrumentation Engineers (SPIE) Conference Series*, volume 6269 of *Society of Photo-Optical Instrumentation Engineers (SPIE) Conference Series*, July 2006.

J. A. Irwin. *Astrophysics: Decoding the Cosmos*. Wiley-VCH Verlag, 2007.

M. Iye, K. Ota, N. Kashikawa, H. Furusawa, T. Hashimoto, T. Hattori, Y. Matsuda, T. Morokuma, M. Ouchi, and K. Shimasaku. A galaxy at a redshift z = 6.96. *Nat*, 443:186–188, September 2006. doi: 10.1038/nature05104.

N. Kashikawa, K. Shimasaku, M. A. Malkan, M. Doi, Y. Matsuda, M. Ouchi, Y. Taniguchi, C. Ly, T. Nagao, M. Iye, K. Motohara, T. Murayama, K. Murozono, K. Nariai, K. Ohta, S. Okamura, T. Sasaki, Y. Shioya, and M. Umemura. The End of the Reionization Epoch Probed by Lyα Emitters at z = 6.5 in the Subaru Deep Field. *ApJ*, 648:7–22, September 2006. doi: 10.1086/504966.

N. Kashikawa, K. Shimasaku, Y. Matsuda, E. Egami, L. Jiang, T. Nagao, M. Ouchi, M. A. Malkan, T. Hattori, K. Ota, Y. Taniguchi, S. Okamura, C. Ly, M. Iye, H. Furusawa, Y. Shioya, T. Shibuya, Y. Ishizaki, and J. Toshikawa. Completing the Census of Lyα Emitters at the Reionization Epoch. *ApJ*, 734:119, June 2011.

T. Kitayama, N. Yoshida, H. Susa, and M. Umemura. The Structure and Evolution of Early Cosmological H II Regions. *ApJ*, 613:631–645, October 2004.

K. Kodaira et al. The Discovery of Two Lyman α Emitters beyond Redshift 6 in the Subaru Deep Field. *PASJ*, 55:L17–L21, April 2003.

J. D. Kurk, H. J. A. Röttgering, L. Pentericci, G. K. Miley, W. van Breugel, C. L. Carilli, H. Ford, T. Heckman, P. McCarthy, and A. Moorwood. A Search for clusters at high redshift. I. Candidate Lyalpha emitters near 1138-262 at z=2.2. *A&A*, 358:L1–L4, June 2000.

J. D. Kurk, L. Pentericci, H. J. A. Röttgering, and G. K. Miley. A search for clusters at high redshift. III. Candidate Hα emitters and EROs in the PKS 1138-262 proto-cluster at z = 2.16. *A&A*, 428:793–815, December 2004. doi: 10.1051/0004-6361:20040075.

D. Larson, J. Dunkley, G. Hinshaw, E. Komatsu, M. R. Nolta, C. L. Bennett, B. Gold, M. Halpern, R. S. Hill, N. Jarosik, A. Kogut, M. Limon, S. S. Meyer, N. Odegard, L. Page, K. M. Smith, D. N. Spergel, G. S. Tucker, J. L. Weiland, E. Wollack, and E. L. Wright. Seven-year WMAP Observations: Power Spectra and WMAP-derived Parameters. *ApJS*, 192:16, February 2011.

F. LeBlanc. *An Introduction to Stellar Astrophysics*. Wiley, 2010.

M. D. Lehnert and M. Bremer. Luminous Lyman Break Galaxies at $z > 5$ and the Source of Reionization. *ApJ*, 593:630–639, August 2003. doi: 10.1086/376729.

M. D. Lehnert, N. P. H. Nesvadba, J.-G. Cuby, A. M. Swinbank, S. Morris, B. Clément, C. J. Evans, M. N. Bremer, and S. Basa. Spectroscopic confirmation of a galaxy at redshift z = 8.6. *Nat*, 467:940–942, October 2010.

G. Lemaître. Un Univers homogène de masse constante et de rayon croissant rendant compte de la vitesse radiale des nébuleuses extra-galactiques. *Annales de la Societe Scietifique de Bruxelles*, 47:49–59, 1927.

S. J. Lilly and L. L. Cowie. Deep infrared surveys (Invited). In C. G. Wynn-Williams and E. E. Becklin, editors, *Infrared astronomy with arrays*, page 473, 1987.

A. Loeb. *How Did the First Stars and Galaxies Form?* Princeton Univ. Press, 2010.

A. Loeb and G. Rybicki. Scattered ly-alpha radiation around sources before cosmological reionization. *The Astrophysical Journal*, 524:527, 1999.

A. Loeb, R. Barkana, and L. Hernquist. Was the Universe Reionized at Redshift 10? *ApJ*, 620:553–558, February 2005. doi: 10.1086/427229.

M. S. Longair. *The Cosmic Century.* Cambridge University Press, June 2006.

S. Lorenzoni, A. J. Bunker, S. M. Wilkins, E. R. Stanway, M. J. Jarvis, and J. Caruana. Star-forming galaxies at z approx 8-9 from Hubble Space Telescope/WFC3: implications for reionization. *MNRAS*, 414:1455–1466, June 2011.

C. Mackay, A. Basden, and M. Bridgeland. Astronomical imaging with L3CCDs: detector performance and high-speed controller design. In J. D. Garnett and J. W. Beletic, editors, *Optical and Infrared Detectors for Astronomy*, volume 5499 of *Society of Photo-Optical Instrumentation Engineers (SPIE) Conference Series*, pages 203–209, September 2004.

C. D. Mackay. Charge-coupled devices in astronomy. *ARA&A*, 24:255–283, 1986.

S. Malhotra and J. E. Rhoads. Luminosity Functions of Lyα Emitters at Redshifts z=6.5 and z=5.7: Evidence against Reionization at z$\leq$6.5. *ApJ*, 617:L5–L8, December 2004. doi: 10.1086/427182.

M. R. C. McDowell. On the formation of H2 in H I regions. *The Observatory*, 81: 240–243, December 1961.

E. M. McLinden, S. L. Finkelstein, J. E. Rhoads, S. Malhotra, P. Hibon, M. L. A. Richardson, G. Cresci, A. Quirrenbach, A. Pasquali, F. Bian, X. Fan, and C. E. Woodward. First Spectroscopic Measurements of [O III] Emission from Lyα Selected Field Galaxies at $z \sim 3.1$. *ApJ*, 730:136, April 2011.

R. J. McLure, J. S. Dunlop, M. Cirasuolo, A. M. Koekemoer, E. Sabbi, D. P. Stark, T. A. Targett, and R. S. Ellis. Galaxies at z = 6-9 from the WFC3/IR imaging of the Hubble Ultra Deep Field. *MNRAS*, 403:960–983, April 2010.

M. McQuinn, L. Hernquist, M. Zaldarriaga, and S. Dutta. Studying reionization with Lyα emitters. *MNRAS*, 381:75–96, October 2007.

A. Mesinger and S. R. Furlanetto. Lyα emitters during the early stages of reionization. *MNRAS*, 386:1990–2002, June 2008. doi: 10.1111/j.1365-2966.2008.13039.x.

H. Mo, F. C. van den Bosch, and S. White. *Galaxy Formation and Evolution*. Cambridge University Press, May 2010.

A. Modigliani. X-Shooter Pipeline User Manual Issue 7.0 (VLT-MAN-ESO-14650-4840). 2012.

A. Modigliani, P. Goldoni, F. Royer, R. Haigron, L. Guglielmi, P. François, M. Horrobin, P. Bristow, J. Vernet, S. Moehler, F. Kerber, P. Ballester, E. Mason, and L. Christensen. The X-shooter pipeline. In *Society of Photo-Optical Instrumenta-*

tion Engineers (SPIE) Conference Series, volume 7737 of *Society of Photo-Optical Instrumentation Engineers (SPIE) Conference Series*, July 2010.

D. J. Mortlock, S. J. Warren, B. P. Venemans, M. Patel, P. C. Hewett, R. G. McMahon, C. Simpson, T. Theuns, E. A. Gonzáles-Solares, A. Adamson, S. Dye, N. C. Hambly, P. Hirst, M. J. Irwin, E. Kuiper, A. Lawrence, and H. J. A. Röttgering. A luminous quasar at a redshift of z = 7.085. *Nat*, 474:616–619, June 2011.

T. Murayama, Y. Taniguchi, N. Z. Scoville, M. Ajiki, D. B. Sanders, B. Mobasher, H. Aussel, P. Capak, A. Koekemoer, Y. Shioya, T. Nagao, C. Carilli, R. S. Ellis, B. Garilli, M. Giavalisco, M. G. Kitzbichler, O. Le Fèvre, D. Maccagni, E. Schinnerer, V. Smolčić, S. Tribiano, A. Cimatti, Y. Komiyama, S. Miyazaki, S. S. Sasaki, J. Koda, and H. Karoji. Lyα Emitters at Redshift 5.7 in the COSMOS Field. *ApJS*, 172:523–544, September 2007.

P. A. Oesch, R. J. Bouwens, C. M. Carollo, G. D. Illingworth, M. Trenti, M. Stiavelli, D. Magee, I. Labbé, and M. Franx. Structure and Morphologies of z$\sim$7-8 Galaxies from Ultra-deep WFC3/IR Imaging of the Hubble Ultra-deep Field. *ApJ*, 709: L21–L25, January 2010a. doi: 10.1088/2041-8205/709/1/L21.

P. A. Oesch, R. J. Bouwens, G. D. Illingworth, C. M. Carollo, M. Franx, I. Labbé, D. Magee, M. Stiavelli, M. Trenti, and P. G. van Dokkum. $z \sim 7$ Galaxies in the HUDF: First Epoch WFC3/IR Results. *ApJ*, 709:L16–L20, January 2010b.

Y. Ono, M. Ouchi, B. Mobasher, M. Dickinson, K. Penner, K. Shimasaku, B. J. Weiner, J. S. Kartaltepe, K. Nakajima, H. Nayyeri, D. Stern, N. Kashikawa, and H. Spinrad. Spectroscopic Confirmation of Three z-Dropout Galaxies at z = 6.844-7.213: Demographics of Lya Emission in z$\sim$7 Galaxies. In *American Astronomical Society Meeting Abstracts #220*, volume 220 of *American Astronomical Society Meeting Abstracts*, page #429.03, May 2012.

K. Ota, M. Iye, N. Kashikawa, K. Shimasaku, M. Kobayashi, T. Totani, M. Nagashima, T. Morokuma, H. Furusawa, T. Hattori, Y. Matsuda, T. Hashimoto, and M. Ouchi. Reionization and Galaxy Evolution Probed by z = 7 Lyα Emitters. *ApJ*, 677:12–26, April 2008.

K. Ota, M. Iye, N. Kashikawa, K. Shimasaku, M. Ouchi, T. Totani, M. A. R. Kobayashi, M. Nagashima, A. Harayama, N. Kodaka, T. Morokuma, H. Furusawa, A. Tajitsu, and T. Hattori. Lyα Emitters at z = 7 in the Subaru/XMM-Newton Deep Survey Field: Photometric Candidates and Luminosity Functions. *ApJ*, 722: 803–811, October 2010. doi: 10.1088/0004-637X/722/1/803.

M. Ouchi, K. Shimasaku, M. Akiyama, K. Sekiguchi, H. Furusawa, S. Okamura, N. Kashikawa, M. Iye, T. Kodama, T. Saito, T. Sasaki, C. Simpson, T. Takata, T. Yamada, H. Yamanoi, M. Yoshida, and M. Yoshida. The Discovery of Primeval Large-Scale Structures with Forming Clusters at Redshift 6. *ApJ*, 620:L1–L4, February 2005. doi: 10.1086/428499.

M. Ouchi, K. Shimasaku, M. Akiyama, C. Simpson, T. Saito, Y. Ueda, H. Furusawa, K. Sekiguchi, T. Yamada, T. Kodama, N. Kashikawa, S. Okamura, M. Iye, T. Takata, M. Yoshida, and M. Yoshida. The Subaru/XMM-Newton Deep Survey (SXDS). IV. Evolution of Lyα Emitters from z=3.1 to 5.7 in the 1 deg^2 Field: Luminosity Functions and AGN. *ApJS*, 176:301–330, June 2008. doi: 10.1086/527673.

M. Ouchi, K. Shimasaku, H. Furusawa, T. Saito, M. Yoshida, M. Akiyama, Y. Ono, T. Yamada, K. Ota, N. Kashikawa, M. Iye, T. Kodama, S. Okamura, C. Simpson, and M. Yoshida. Statistics of 207 Lyα Emitters at a Redshift Near 7: Constraints on Reionization and Galaxy Formation Models. *ApJ*, 723:869–894, November 2010.

A. H. Pawlik, J. Schaye, and E. van Scherpenzeel. Keeping the Universe ionized:

photoheating and the clumping factor of the high-redshift intergalactic medium. *MNRAS*, 394:1812–1824, April 2009.

R. Pelló, D. Schaerer, J. Richard, J.-F. Le Borgne, and J.-P. Kneib. ISAAC/VLT observations of a lensed galaxy at z = 10.0. *A&A*, 416:L35–L40, March 2004.

L. Pentericci et al. Spectroscopic Confirmation of z∼7 Lyman Break Galaxies: Probing the Earliest Galaxies and the Epoch of Reionization. *ApJ*, 743:132, December 2011. doi: 10.1088/0004-637X/743/2/132.

A. A. Penzias and R. W. Wilson. A Measurement of Excess Antenna Temperature at 4080 Mc/s. *ApJ*, 142:419–421, July 1965. doi: 10.1086/148307.

J. Richard, R. Pelló, J.-P. Kneib, D. Schaerer, M. R. Santos, and R. Ellis. In M. Plionis, editor, *Astrophysics and Space Science Library*, volume 301 of *Astrophysics and Space Science Library*, page 27, 2004.

R. Salvaterra et al. GRB090423 at a redshift of z∼8.1. *Nat*, 461:1258–1260, October 2009. doi: 10.1038/nature08445.

M. R. Santos. Probing reionization with Lyman α emission lines. *MNRAS*, 349: 1137–1152, April 2004. doi: 10.1111/j.1365-2966.2004.07594.x.

W. C. Saslaw and D. Zipoy. Molecular Hydrogen in Pre-galactic Gas Clouds. *Nat*, 216:976–978, December 1967. doi: 10.1038/216976a0.

D. Schaerer. On the properties of massive Population III stars and metal-free stellar populations. *A&A*, 382:28–42, January 2002.

M. A. Schenker, D. P. Stark, R. S. Ellis, B. E. Robertson, J. S. Dunlop, R. J. McLure, J.-P. Kneib, and J. Richard. Keck Spectroscopy of Faint $3 < z < 8$ Lyman Break Galaxies: Evidence for a Declining Fraction of Emission Line Sources in the Redshift Range $6 < z < 8$. *ApJ*, 744:179, January 2012.

P. A. G. Scheuer. A Sensitive Test for the Presence of Atomic Hydrogen in Intergalactic Space. *Nat*, 207:963, August 1965. doi: 10.1038/207963a0.

M. Schmidt. Large Redshifts of Five Quasi-Stellar Sources. *ApJ*, 141:1295, April 1965. doi: 10.1086/148217.

S. Serjeant. *Observational Cosmology*. September 2010.

A. E. Shapley, C. C. Steidel, M. Pettini, and K. L. Adelberger. Rest-Frame Ultraviolet Spectra of $z \sim 3$ Lyman Break Galaxies. *ApJ*, 588:65–89, May 2003.

J. Shen, T. Abel, H. J. Mo, and R. K. Sheth. An Excursion Set Model of the Cosmic Web:The Abundance of Sheets, Filaments, and Halos. *ApJ*, 645:783–791, July 2006.

K. Shimasaku et al. Subaru Deep Survey. IV. Discovery of a Large-Scale Structure at Redshift ~ 5. *ApJ*, 586:L111–L114, April 2003.

K. Shimasaku et al. Lyα Emitters at z = 5.7 in the Subaru Deep Field. *PASJ*, 58: 313–334, April 2006.

V. M. Slipher. Spectrographic Observations of Nebulae. *Popular Astronomy*, 23: 21–24, January 1915.

V. M. Slipher. Nebulae. *Proceedings of the American Philosophical Society*, 56:403–409, 1917.

A. Songaila. The Evolution of the Intergalactic Medium Transmission to Redshift 6. *AJ*, 127:2598–2603, May 2004. doi: 10.1086/383561.

D. N. Spergel et al. First-Year Wilkinson Microwave Anisotropy Probe (WMAP) Observations: Determination of Cosmological Parameters. *ApJS*, 148:175–194, September 2003. doi: 10.1086/377226.

D. N. Spergel et al. Three-Year WMAP Observations: Implications for Cosmology. *ApJS*, 170:377–408, June 2007.

V. Springel et al. Simulations of the formation, evolution and clustering of galaxies and quasars. *Nature*, 435:629, 2005.

E. R. Stanway, A. J. Bunker, and R. G. McMahon. Lyman break galaxies and the star formation rate of the Universe at $z \sim 6$. *MNRAS*, 342:439–445, June 2003.

E. R. Stanway, A. J. Bunker, R. G. McMahon, R. S. Ellis, T. Treu, and P. J. McCarthy. Hubble Space Telescope Imaging and Keck Spectroscopy of z ˜ 6 i-Band Dropout Galaxies in the Advanced Camera for Surveys GOODS Fields. *ApJ*, 607: 704–720, June 2004.

E. R. Stanway, A. J. Bunker, K. Glazebrook, R. G. Abraham, J. Rhoads, S. Malhotra, D. Crampton, M. Colless, and K. Chiu. The GLARE Survey - II. Faint $z \sim 6$ Lyα line emitters in the HUDF. *MNRAS*, 376:727–738, April 2007.

E. R. Stanway, M. N. Bremer, V. Squitieri, L. S. Douglas, and M. D. Lehnert. A limit on the number density of bright z∼7 galaxies. *MNRAS*, 386:370–376, May 2008. doi: 10.1111/j.1365-2966.2008.13030.x.

E. R. Stanway et al. Three Lyα Emitters at z∼6: Early GMOS/Gemini Data from the GLARE Project. *ApJ*, 604:L13–L16, March 2004.

D. P. Stark, R. S. Ellis, K. Chiu, M. Ouchi, and A. Bunker. Keck spectroscopy of faint $3 < z < 7$ Lyman break galaxies - I. *MNRAS*, 408:1628–1648, November 2010.

D. P. Stark, R. S. Ellis, and M. Ouchi. Keck Spectroscopy of Faint 3<z<7 Lyman Break Galaxies: A High Fraction of Line Emitters at Redshift Six. *ApJ*, 728:L2, February 2011. doi: 10.1088/2041-8205/728/1/L2.

C. C. Steidel and D. Hamilton. Deep imaging of high redshift QSO fields below the Lyman limit. I - The field of Q0000-263 and galaxies at Z = 3.4. *AJ*, 104:941–949, September 1992. doi: 10.1086/116287.

C. C. Steidel, K. L. Adelberger, M. Dickinson, M. Giavalisco, M. Pettini, and M. Kellogg. A Large Structure of Galaxies at $z \approx 3$ and Its Cosmological Implications. *ApJ*, 492:428, January 1998. doi: 10.1086/305073.

C. C. Steidel, M. Bogosavljević, A. E. Shapley, J. A. Kollmeier, N. A. Reddy, D. K. Erb, and M. Pettini. Diffuse Lyα Emitting Halos. *ApJ*, 736:160, August 2011.

D. Stern and H. Spinrad. Search Techniques for Distant Galaxies. *PASP*, 111:1475–1502, December 1999. doi: 10.1086/316471.

D. Stern, P. Eisenhardt, H. Spinrad, S. Dawson, W. van Breugel, A. Dey, W. de Vries, and S. A. Stanford. *Nat*, 408:560–562, November 2000.

K. R. Stewart, J. S. Bullock, E. J. Barton, and R. H. Wechsler. *ApJ*, 702:1005–1015, September 2009.

R. Suzuki et al. MOIRCS for the Subaru Telescope I. Imaging. *PASJ*, 60:1347, December 2008.

Y. Taniguchi et al. The SUBARU Deep Field Project: Lyman-α Emitters at a Redshift of 6.6. *PASJ*, 57:165–182, February 2005.

N. R. Tanvir. The highest redshift GRBs and their host galaxies. In *American Institute of Physics Conference Series*, volume 1279, pages 32–39, October 2010.

N. R. Tanvir et al. A γ-ray burst at a redshift of z$\sim$8.2. *Nat*, 461:1254–1257, October 2009.

M. Tegmark, J. Silk, M. J. Rees, A. Blanchard, T. Abel, and F. Palla. How Small Were the First Cosmological Objects? *ApJ*, 474:1, January 1997. doi: 10.1086/303434.

P. Todini and A. Ferrara. Dust formation in primordial Type II supernovae. *MNRAS*, 325:726, 2001.

J. Tumlinson, J. M. Shull, and A. Venkatesan. *ApJ*, 584:608–620, February 2003.

J. A. Tyson. In *CCDs in astronomy*, volume 8 of *Astronomical Society of the Pacific Conference Series*, pages 1–10, 1990.

N. D. Tyson and R. R. Gal. *AJ*, 105:1206–1212, March 1993.

E. Vanzella, L. Pentericci, A. Fontana, A. Grazian, M. Castellano, K. Boutsia, S. Cristiani, M. Dickinson, S. Gallozzi, E. Giallongo, M. Giavalisco, R. Maiolino, A. Moorwood, D. Paris, and P. Santini. Spectroscopic Confirmation of Two Lyman Break Galaxies at Redshift Beyond 7. *ApJ*, 730:L35, April 2011.

E. Vanzella et al. Spectroscopic Observations of Lyman Break Galaxies at Redshifts $\sim$4, 5, and 6 in the Goods-South Field. *ApJ*, 695:1163–1182, April 2009.

B. P. Venemans et al. Protoclusters associated with $z > 2$ radio galaxies. I. Characteristics of high redshift protoclusters. *A&A*, 461:823–845, January 2007.

K. Vollmann and T. Eversberg. *Astronomische Nachrichten*, 327:862, November 2006.

M. Volonteri and N. Y. Gnedin. Relative Role of Stars and Quasars in Cosmic Reionization. *ApJ*, 703:2113–2117, October 2009.

S. J. Weatherley, S. J. Warren, and T. S. R. Babbedge. Reanalysis of the spectrum of the z = 10 galaxy. *A&A*, 428:L29–L32, December 2004.

D. Whalen, T. Abel, and M. L. Norman. Radiation Hydrodynamic Evolution of Primordial H II Regions. *ApJ*, 610:14–22, July 2004. doi: 10.1086/421548.

S. M. Wilkins, A. J. Bunker, R. S. Ellis, D. Stark, E. R. Stanway, K. Chiu, S. Lorenzoni, and M. J. Jarvis. Probing $\sim L_*$ Lyman-break galaxies at z$\sim$7 in GOODS-South

with WFC3 on Hubble Space Telescope. *MNRAS*, 403:938–944, April 2010. doi: 10.1111/j.1365-2966.2009.16175.x.

S. M. Wilkins, A. J. Bunker, S. Lorenzoni, and J. Caruana. New star-forming galaxies at $z \approx 7$ from Wide Field Camera Three imaging. *MNRAS*, 411:23–36, February 2011. doi: 10.1111/j.1365-2966.2010.17626.x.

C. Willott. Cosmology: A monster in the early Universe. *Nat*, 474:583–584, 2011. doi: 10.1038/474583a.

J. H. Wise and T. Abel. How Very Massive Metal-Free Stars Start Cosmological Reionization. *ApJ*, 684:1–17, September 2008. doi: 10.1086/590050.

J. S. B. Wyithe, A. M. Hopkins, M. D. Kistler, H. Yüksel, and J. F. Beacom. Determining the escape fraction of ionizing photons during reionization with the GRB-derived star formation rate. *MNRAS*, 401:2561–2571, February 2010.

H.-J. Yan, R. A. Windhorst, N. P. Hathi, S. H. Cohen, R. E. Ryan, R. W. O'Connell, and P. J. McCarthy. Galaxy formation in the reionization epoch as hinted by Wide Field Camera 3 observations of the Hubble Ultra Deep Field. *Research in Astronomy and Astrophysics*, 10:867–904, September 2010. doi: 10.1088/1674-4527/10/9/003.

N. Yoshida, S. P. Oh, T. Kitayama, and L. Hernquist. Early Cosmological H II/He III Regions and Their Impact on Second-Generation Star Formation. *ApJ*, 663: 687–707, July 2007.